

# Ab initio radiation chemistry

Dissertation zur Erlangung des Doktorgrades  
des Fachbereiches Chemie  
der Universität Hamburg

vorgelegt von

**Sophia Bazzi**

Hamburg

2019

Gutachter der Dissertation: Prof. Dr. Robin Santra  
Prof. Dr. Carmen Herrmann

Gutachter der Disputation: Prof. Dr. Robin Santra  
Prof. Dr. Melanie Schnell  
Priv. Doz. Dr. Markus Perbandt

Datum der Disputation: June 14<sup>th</sup>, 2019.

Vorsitzender des Fach-Promotionsausschusses: Prof. Dr. Robin Santra

Leiter des Fachbereiches Chemie: Prof. Dr. Michael Fröba

Dekan der Fakultät für Mathematik,  
Informatik und Naturwissenschaften: Prof. Dr. Heinrich Graener

*To my dear parents  
Shahnaz and Gholamreza*

## *Acknowledgements*

I had one reason to join Robin Santra's group and I now have many reasons to thank him. I always felt welcome to discuss science with Robin even at times when he was extremely busy. I remember several occasions when we aimed for a ten minutes urgent discussion but it actually took several hours because of the joy and enthusiasm he has for science. Robin is an example of a true leader who can listen without prejudice and guide without hesitation. My last research activity as a Ph.D. student in Robin's group is an example that shows he is an open-minded scientist who let me work independently on my own idea while guiding me at the most important moments of my work.

The one reason that I, as a chemist, joined a theoretical physics group was Robin's unique way of thinking reflected in the group's publications where the most complicated problems were solved in an understandable and creative way by making use of original ideas in physics and chemistry; the decision that I don't regret. Thank you Robin for being a fantastic human, a true leader, and an open-minded scientist.

My mentor, Dr. Isabell Melzer-Pellmann, for her excellent and honest advice.

Oriol Vendrell with whom I worked for the first nine months of my Ph.D. before he moved to a new place. I learned a lot from Oriol in a short period of time. Zoltan Jurek, on whom I could always count, Ralph Welsch, Murali Krishna and Khadijeh Khalili for the fruitful discussions we had, Sascha Epp for helping me with translation of the abstract and Malik Muhammad Abdullah and John Bekx for making the workplace a lively and happy environment with their humor.

I gratefully acknowledge the funding sources that made my Ph.D. work possible. I was funded by the Deutsches Elektronen-Synchrotron (DESY). I had the honor to be a member of the PIER Helmholtz Graduate School (PHGS) and I thank the PHGS team especially Stefanie Tepass, and Mirko Siemssen.

I thank my friends, Abdolali Miradi, Maryam Sayfollahi, Masoud Mehrjoo, Soodabeh Darzi, Arya Fallahi, Moein Fakhari, and Sadegh Bakhtiarzadeh, for being like a family to me in my happy and sad times.

I thank my dear parents Shahnaz Sarabandi and Gholamreza Bazzi, and my amazing sisters, Maryam, Sara, and Safura, five pieces of my soul for their unconditional love and support.

Most of all, I thank my loving, encouraging, and patient partner Mehdi Ravandeh who spent many weekends at CFEL with me.

# Zusammenfassung

Die Entwicklung neuer Techniken und Werkzeuge wie z.B. Freie-Elektronen-Laser (FELs) oder Pump-Probe-Experimente eröffneten neue Herangehensweisen in der Femtochemie, insbesondere die Beobachtung der Echtzeitdynamik von lichtangeregten Molekülen auf der Femtosekunden-Zeitskala. Die Fortschritte bei Femtochemie Experimenten bringen neue Herausforderungen und Möglichkeiten auf dem Gebiet der theoretischen Femtochemie, zur Beschreibung der ultraschneller Molekulardynamik auf den Potenzialhyperflächen elektronisch angeregter Moleküle.

Diese Arbeit stellt eine Reihe von theoretischen Studien über die ultraschnelle Dynamik molekularer Systeme nach Anregung oder Ionisation durch Laserpulse im VUV-bis XUV-Regime an, welche für Pump-Probe-Experimente von großer Bedeutung sind. Die Theorie dieser Arbeit basiert auf ab-initio klassischen Trajektoriekalkulationen innerhalb des "fewest switches surface hopping (FSSH)"- Schemas. In vorliegender Arbeit wird die VUV bis XUV- Photochemie anhand drei verschiedener molekularer Spezies und drei separater Studien untersucht. Die Studien innerhalb der vorliegenden Arbeit umfassen folgende Bereiche: (I) eine gemeinsame experimentelle und theoretische Studie über die VUV-induzierte Dynamik von H<sub>2</sub>O und seinen deuterierten Isotopologen unter Verwendung eines VUV-Pump-VUV-Probe Schemas; (II) XUV-Photochemie des Benzol Kations, welche die zeitaufgelöste, zustandsspezifische Fragmentierungsdynamik und die zeitaufgelöste Relaxation der elektronisch angeregten Zustände umfasst; (III) die ultraschnelle Ladungsübertragung und Strukturdynamik nach externer Valenzionisation von CH<sub>2</sub>O···ClF, einem halogengebundenen Dimer.

Wir zeigen wie die Ergebnisse von ab-initio Trajektorienberechnungen von der Auswahl der verwendeten elektronischen Strukturmethoden abhängen. Wir betonen daher die Notwendigkeit effizienter und dennoch genauer elektronischer Strukturansätze, die sich nicht auf kleine molekulare Systeme und einige angeregte Zustände beschränken.



# Abstract

The development of tools and techniques such as free-electron lasers (FELs) and pump-probe experiments has advanced the field of femtochemistry and made it possible to follow the real-time dynamics of photo-excited molecular species on the femtosecond time scale. Advances in femtochemistry experiments present new challenges and opportunities in the field of theoretical/computational femtochemistry for describing the ultrafast molecular dynamics on the potential energy surfaces of electronically excited molecules.

This thesis presents a series of theoretical studies on ultrafast dynamics of molecular systems after excitation/ionization by laser pulses in the VUV to XUV regime, which is highly relevant for pump-probe experiments. The theory employed in this thesis is based on ab initio classical trajectory calculations within the fewest switches surface hopping (FSSH) scheme. In the present thesis the VUV to XUV- photochemistry of three different molecular species is investigated in three separate studies. The studies within the present work encompass: (I) a joint experimental and theoretical study on the VUV-induced dynamics of H<sub>2</sub>O and its deuterated isotopologues utilizing a VUV-pump VUV-probe scheme; (II) XUV photochemistry of the benzene radical cation that includes the time-resolved state-specific fragmentation dynamics, and the time resolved relaxation of the electronic excited states through internal conversion; and (III) ultrafast charge transfer and structural dynamics following outer valence ionization of CH<sub>2</sub>O···ClF, a halogen-bonded dimer.

In all of these studies one can see how the results of an ab initio classical trajectory calculations depend on the selection of electronic structure methods employed. We highlight the need for efficient and yet accurate electronic structure approaches that are not limited to small molecular systems and a few excited states.

# List of Publications

1. *"Challenges in XUV photochemistry simulations: A Case study on ultrafast fragmentation dynamics of the benzene radical cation"*,  
S. Bazzi, R. Welsch, O. Vendrell, and R. Santra *J. Phys. Chem. A*, **122**, (2018).  
<https://pubs.acs.org/doi/abs/10.1021/acs.jpca.7b11543>
2. *"Weak-field few-femtosecond VUV photodissociation dynamics of water isotopologues"*,  
A. Baumann, S. Bazzi, D. Rompotis, O. Schepp, A. Azima, M. Wieland, D. Popova-Gorelova, O. Vendrell, R. Santra, and M. Drescher *Phys. Rev. A*, **96**, (2017). <https://journals.aps.org/prabstract/10.1103/PhysRevA.96.013428>
3. *"Ultrafast charge transfer and structural dynamics following outer valence ionization of a halogen-bonded dimer"*,  
S. Bazzi and R. Santra, *J. Phys. Chem. A*, **123**, (2019). <https://pubs.acs.org/doi/abs/10.1021/acs.jpca.9b00646>

# List of Abbreviations

<b>ADC</b>	Algebraic-diagrammatic construction
<b>APS</b>	American Physical Society
<b>CAS</b>	Complete active space
<b>CASPT2</b>	CAS second order perturbation theory
<b>CASSCF</b>	Complete active space self-consistent field
<b>CC2</b>	Coupled-cluster method of second order
<b>CDTK</b>	Chemical dynamics toolkit
<b>CI</b>	Configuration interaction
<b>CIS</b>	CI singles
<b>CISD</b>	CI singles and doubles
<b>CSFs</b>	Configuration state functions
<b>eV</b>	Electron Volt
<b>FSSH</b>	Fewest switches surface hopping
<b>FC</b>	Franck–Condon
<b>FEL</b>	Free-electron laser
<b>FLASH</b>	Free-electron Laser Hamburg
<b>FSSH</b>	Fewest switches surface hopping
<b>FWHM</b>	Full width at half maximum
<b>HF</b>	Hartree-Fock
<b>HOMO</b>	Highest occupied molecular orbital
<b>LCLS</b>	(Stanford) LINAC Coherent Light Source

<b>MCTDH</b>	Multiconfigurational time-dependent Hartree
<b>MCSCF</b>	Multi-configurational SCF
<b>MO</b>	Molecular orbital
<b>MRCI</b>	Multireference CI
<b>NA-MQC</b>	Nonadiabatic Mixed Quantum-Classical
<b>PAHs</b>	Polycyclic aromatic hydrocarbons
<b>RASSCF</b>	Restricted active space SCF
<b>SA-CASSCF</b>	State averaged CASSCF
<b>SCF</b>	Self-consistent field
<b>SACLA</b>	Spring-8 angstrom compact free electron laser
<b>SLAC</b>	Stanford Linear Accelerator Center
<b>TDDFT</b>	Time-dependent density functional theory
<b>TDSE</b>	Time-dependent Schrödinger equation
<b>UV</b>	Ultraviolet
<b>VUV</b>	Vacuum Ultraviolet
<b>XC</b>	Exchange-correlation
<b>XFEL</b>	X-ray Free electron laser
<b>XUV</b>	Extreme Ultraviolet

# List of Figures

2.1	A system which contains the states $a$ and $b$ , where the number of trajectories in the state $b$ equals 6 at time $t$ and is reduced to 5 at time $t'$ . The middle panel illustrates the various possible switches that bring the system from the population distribution at time $t$ to the one at time $t'$ . The first possibility shows how this distribution can be achieved with the minimum number of transitions. . . . .	20
3.1	Sketch of the optical setup used to perform the single-shot pump-probe experiment. © 2017, American Physical Society (APS) . . . . .	32
3.2	Ion microscope image and delay-dependent ion signal originating from the non-resonant two-photon ionization of Kr. The microscope image (a) shows the averaged spatially resolved $\text{Kr}^+$ ion yield for 3000 laser pulses. The averaged delay-dependent $\text{Kr}^+$ ion yield (b) corresponds to the VUV pulse intensity autocorrelation, which yields an instrument response function with a FWHM of $(23.1 \pm 1.4)$ fs. From the single-shot intensity autocorrelation for each laser pulse (c), the root-mean-square uncertainty of its FWHM (d) can be deduced. © 2017, American Physical Society (APS) . . . . .	34

3.3	<p>(a) Cuts through the potential energy surfaces for the ground and first excited electronic states of <math>\text{H}_2\text{O}</math> and <math>\text{H}_2\text{O}^+</math> calculated at the MR-CISD(8,7) and MR-CISD(7,7) level, respectively (solid lines) and for the <math>\tilde{A}^1B_1</math> state of <math>\text{H}_2\text{O}</math> calculated with CASSCF(6,4) (dashed line). The dissociation coordinate is obtained by changing the length of one of the O-H bonds (<math>R_{\text{OH}}</math>) and maintaining the other O-H bond length and the angle HOH at the equilibrium values of 0.958 Å and 104.47°, respectively. <math>R_{\text{OH}} = 0</math> corresponds to the equilibrium bond length. (b) The dominant configurations for the <math>\tilde{A}^1B_1</math> state of a neutral water molecule, and <math>\tilde{X}^2B_1</math> and <math>\tilde{A}^2A_1</math> states of the cation and their corresponding CI coefficients at the equilibrium geometry (W) are obtained from the MR-CISD calculation. © 2017, American Physical Society (APS)</p>	38
3.4	<p>Calculated time evolution of the vertical excitation energy from the <math>\tilde{A}^1B_1</math> to the <math>\tilde{X}^2B_1</math> state (blue) and from the <math>\tilde{A}^1B_1</math> to the <math>\tilde{A}^2A_1</math> state (orange) during the dissociation for (a) <math>\text{H}_2\text{O}</math>, (b) HDO, and (c) <math>\text{D}_2\text{O}</math> and the corresponding time windows, in which ionization from <math>\tilde{A}^1B_1</math> to <math>\tilde{X}^2B_1</math> and <math>\tilde{A}^2A_1</math> with a single photon of 7.7 eV energy (gray line) is possible. The error bars represent the root-mean-square width of the energy distribution for a given time. © 2017, American Physical Society (APS)</p>	41

3.5	Ion microscope images and delay-dependent ion signals for H <sub>2</sub> O, HDO and D <sub>2</sub> O. The microscope image (a) shows the averaged spatially resolved ion yield of the different isotopologues for 3000 laser pulses. The delay-dependent ion signal (b) of each isotopologue is shown in comparison to the instrument response function (blue) recorded in the corresponding measurement series and fitted with a Gaussian function (red). Depending on the degree of deuterization an increased FWHM is observed with respect to the instrument response function, indicating a kinetic isotope effect on the excited state dynamics of the molecule.	44
© 2017, American Physical Society (APS) . . . . .		44
4.1	Fragmentation dynamics along with the internal conversion dynamics for an initial excitation to the states a) $\tilde{B}^2E_{2g}$ , b) $\tilde{D}^2E_{1u}$ , c) $\tilde{G}^3A_{1g}$ d) $\tilde{H}^2E_{2g}$ , e) $\tilde{I}^2E_{1u}$ , and f) $\tilde{J}^2A_{1g}$ . The left bar displays the current electronic state of the trajectory and the right bar indicates the fragments. Taken from the supplementary information of Ref. [187].	56
© 2018, American Chemical Society (ACS) . . . . .		56
4.2	Cuts through the potential energy surface for the $\tilde{X}^2E_{1g}$ state of C <sub>6</sub> H <sub>6</sub> <sup>+</sup> calculated with HF/6-31g* (green), and CASPT2(12,8)/6-31g* (blue). The dissociation coordinate is obtained by changing the length of one of the CH bonds (R <sub>CH</sub> ) and maintaining the other bond lengths and the angles at the equilibrium values. R <sub>0</sub> corresponds to the equilibrium bond length. Figure is taken from Ref. [187].	57
© 2018, American Chemical Society (ACS) . . . . .		57
4.3	Internal conversion dynamics for an initial excitation to the states (a) $\tilde{B}^2E_{2g}$ , (b) $\tilde{C}^2A_{2u}$ , (c) $\tilde{D}^2E_{1u}$ , and (d) $\tilde{H}^2E_{2g}$ . Figure is taken from Ref. [187].	58
© 2018, American Chemical Society (ACS) . . . . .		58

4.4	Internal conversion dynamics for an initial excitation on the states (a) $\tilde{E}^2B_{2u}$ , (b) $\tilde{F}^2B_{1u}$ , (c) $\tilde{G}^3A_{1g}$ , (d) $\tilde{I}^2E_{1u}$ , and (e) $\tilde{J}^2A_{1g}$ . Figure is taken from the supplementary information of Ref. [187]. © 2018, American Chemical Society (ACS) . . . . .	59
5.1	Ground-state geometry of the $\text{CH}_2\text{O}\cdots\text{ClF}$ dimer calculated at the HF/ANO-L-VTZP level. The main structural parameters from the calculated ground-state geometry (cal.) are given and compared to the experimental values (ex.) obtained from Ref. Cooke1998. © 2019, American Chemical Society (ACS) . . . . .	63
5.2	Cuts through the potential energy surfaces for the ground ( $D_0$ ), first excited ( $D_1$ ), and second excited ( $D_2$ ) electronic states of the $\text{CH}_2\text{O}\cdots\text{ClF}$ dimer cation calculated at a) Koopmans' level and b) CASCI(5,8). The ANO-L-VTZP basis set is used in both calculations. The intermolecular coordinate is obtained by changing the distance along the (Cl $\cdots$ O) halogen bond ( $R_{\text{Cl}\cdots\text{O}}$ ) and maintaining the rest of the bonds and the angles at the equilibrium geometry of the neutral dimer. $R_{\text{Cl}\cdots\text{O}} = 0$ corresponds to the equilibrium intermolecular distance in the neutral dimer. © 2019, American Chemical Society (ACS) . . . . .	67
5.3	Isosurfaces of the three highest molecular orbitals of the $\text{CH}_2\text{O}\cdots\text{ClF}$ dimer and the corresponding orbital energies calculated at the HF/ANO-L-VTZP level at the equilibrium geometry of the neutral dimer, as well as the partial hole population on the ClF molecule. © 2019, American Chemical Society (ACS) . . . . .	68
5.4	Dynamics of: (a) intermolecular charge transfer, and (b) electronic population, averaged over 100 trajectories for an initial excitation to the $D_1$ of the dimer cation. © 2019, American Chemical Society (ACS) . . . . .	69

5.5	Temporal evolution of: (a) atomic charges, (b) intramolecular distances, and (c) intermolecular distances, averaged over 100 trajectories for an initial excitation to the $D_1$ of the dimer cation. © 2019, American Chemical Society (ACS) . . . . .	72
5.6	Time evolution of the nuclear motion and the molecular orbital accommodating the hole in a representative trajectory for an initial excitation to the $D_1$ of the dimer cation. The distance between the Cl and O atoms is given in Å. © 2019, American Chemical Society (ACS) . . . . .	74
5.7	Dynamics of: (a) intermolecular charge transfer, and (b) electronic population, averaged over 100 trajectories for an initial excitation to the $D_2$ of the dimer cation. © 2019, American Chemical Society (ACS) . . . . .	75
5.8	Temporal evolution of: (a) atomic charges, (b) intramolecular distances, and (c) intermolecular distances, averaged over 100 trajectories for an initial excitation to the $D_2$ of the dimer cation. © 2019, American Chemical Society (ACS) . . . . .	76
5.9	Time evolution of the nuclear motion and molecular orbital accommodating the hole in a representative trajectory for an initial excitation to the $D_2$ of the dimer cation. The distance between the Cl and O atoms is given in Å. © 2019, American Chemical Society (ACS) . . . . .	77
5.10	Dynamics of the intermolecular charge transfer, averaged over 100 trajectories, following ionization out of the HOMO. © 2019, American Chemical Society (ACS) . . . . .	78
5.11	Temporal evolution of: (a) atomic charges and charge of the $\text{CH}_2$ group, (b) intramolecular distances, and (c) intermolecular distances, averaged over 100 trajectories, following ionization out of the HOMO. © 2019, American Chemical Society (ACS) . . . . .	79

# List of Tables

3.1	Vertical ionization energies of H <sub>2</sub> O at the experimental equilibrium position (top) and at the asymptotic region (bottom) calculated with (a) MR-CISD and (b) CASSCF with the OH bond length kept fixed at the equilibrium OH bond length of H <sub>2</sub> O. Experimental ionization energies for H <sub>2</sub> O, OH in their respective equilibrium geometries and the Hydrogen radical are taken from Refs. [168] and [169]. All values in electronvolts . . . . .	35
4.1	The symmetry assignment of the excited electronic states of C <sub>6</sub> H <sub>6</sub> <sup>+</sup> and the corresponding orbital energies calculated at HF/6-31g* level at the equilibrium geometry of the neutral benzene. The dissociation probability for an initial excitation to each electronic state is also given. The Half life of each of the initially excited states is given and compared to Ref. [186]. . . . .	50
4.2	Average of the minimum and maximum difference between the potential energies along the 50 trajectories started on the given potential energy surfaces. All quantities are given in eV. Table is taken from the supplementary information of Ref. [187]. . . . .	55

# Contents

<b>Acknowledgements</b>	<b>iv</b>
<b>Zusammenfassung</b>	<b>vi</b>
<b>Abstract</b>	<b>viii</b>
<b>List of publications</b>	<b>ix</b>
<b>List of Figures</b>	<b>xi</b>
<b>List of Tables</b>	<b>xvi</b>
<b>1 Introduction</b>	<b>1</b>
1.1 Structure of this thesis . . . . .	11
<b>2 Introduction to Theoretical Framework</b>	<b>14</b>
2.1 Born-Oppenheimer approximation . . . . .	14
2.2 Tully's fewest switches algorithm . . . . .	16
2.2.1 Kinetic energy adjustment . . . . .	22
2.2.2 Ensemble of trajectories . . . . .	23
2.2.3 Generation of initial phase space . . . . .	24
2.2.4 Numerical integration of Newton's equations . . . . .	24
2.2.5 Choice of the electronic structure method . . . . .	25
2.2.6 Koopmans' theorem . . . . .	29

<b>3</b>	<b>Weak-field few-fs VUV photodissociation dynamics of water isotopologues</b>	<b>31</b>
3.1	Experimental methods . . . . .	32
3.2	Computational methods . . . . .	35
3.3	Results and discussion . . . . .	37
3.3.1	Experimental data . . . . .	37
3.3.2	Computational data . . . . .	40
<b>4</b>	<b>XUV photochemistry of the Benzene Radical Cation</b>	<b>45</b>
4.1	Computational methods . . . . .	46
4.2	Potential energy surfaces . . . . .	48
4.3	State-specific fragmentation dynamics . . . . .	49
4.4	Internal conversion dynamics . . . . .	51
<b>5</b>	<b>Ultrafast charge transfer and structural dynamics following outer valence ionization of a halogen-bonded dimer</b>	<b>60</b>
5.1	Computational methods . . . . .	61
5.1.1	The first electronically excited state . . . . .	67
5.1.2	The second electronically excited state . . . . .	71
5.1.3	The ground state . . . . .	77
<b>6</b>	<b>Conclusions and Outlook</b>	<b>80</b>
	<b>Bibliography</b>	<b>84</b>
	<b>References</b>	<b>97</b>



# Chapter 1

## Introduction

With visible light we see the visible world; with Newtonian mechanics we understand and control this world. In order to see the invisible, however, we need a different kind of light; in order to understand and control the invisible, we need a different kind of mechanics, i.e., quantum mechanics. For a chemist, the invisible world is about the molecules and the atoms, their reactions, and their dynamics. In 1999, Nobel Prize-winning chemist Prof. Ahmed Zewail ushered the chemists into the world of femtochemistry with the real-time study of chemical bond breaking and bond formation that occur on the time scale of molecular vibrations and rotations, the fastest period of which is  $\approx 10$  femtoseconds ( $10^{-14}s$ ) [1]. A simple and yet powerful tool to study femtosecond experiments are pump-probe experiments. In such experiments, a pump pulse initiates the chemical process and a probe pulse interrogates its temporal evolution.

Two typical methods in femtochemistry experiments through which information about an evolving molecular structure at each instant of time can be obtained are molecular absorption and diffraction experiments. Diffraction experiments themselves are divided into two categories: light and electron diffraction. In order to resolve molecular distances in light-diffraction experiments we have to work in the X-ray regime.

There are currently a handful of X-ray free electron lasers (FELs) available to perform

time-resolved X-ray diffraction experiments, including European X-ray free electron laser (XFEL) in Hamburg, LINAC Coherent Light Source (LCLS) at Stanford, and spring-8 angstrom compact free electron laser (SACLA) in Japan. The first experiments of this kind were developed at X-ray synchrotrons. Laser-plasma based X-ray sources are other facilities capable of performing X-ray diffraction experiments.

FELs can produce very short laser pulses with high photon energy and high brilliance [2, 3]. There are several other FEL facilities in the world that provide femtosecond XUV/X-ray pulses. The free-electron laser in hamburg (FLASH), is the first ever built FEL to carry out experiments in the vacuum ultraviolet (VUV) and soft x-ray regime [4]. FLASH generates laser pulses with pulse durations from 10 fs to 70 fs and with wavelengths that range from 6.8 nm to 47 nm [3].

The femtosecond experiments require special theoretical support, because the ultra-short femtosecond pulses can bring the molecules into their highly (electronically) excited states, in which the Born-Oppenheimer approximation is not necessarily valid. Chemical dynamics is about motions of electrons and nuclei of atoms. In chemistry, however, we do not (cannot) keep track of every possible motion of every electron and nucleus. Instead we determine the state of a system. Each state possesses a certain amount of energy. In every molecular configuration, a molecular system has a certain amount of energy. These several energy points finally provide us with the potential energy surfaces of a molecule in motion [5].

The concept of potential energy surface was first introduced by Eyring and Polanyi in a historic 1931 paper [6]. An accurate description of molecular dynamic processes requires an accurate description of the potential energy surface(s) governing the dynamics. If the nuclear motion is affected by one potential energy surface, the Born-Oppenheimer approximation is valid. However, if more than one potential energy surfaces are involved, a non-Born-Oppenheimer description of the molecular dynamics

would be inevitable.

The large mass of a nucleus compared to that of an electron permits an approximate separation of the electronic and nuclear motion which is called the Born-Oppenheimer approximation where electrons adjust instantaneously to the slower motion of the nuclei. The mathematical foundation for this is given in a 1927 historical paper by Born and Oppenheimer [7]. According to the Born-Oppenheimer approximation, the true molecular wave function is adequately approximated as [8]:

$$\Psi(q_i, q_\alpha) = \Psi_{el}(q_i, q_\alpha)\Psi_N(q_\alpha), \quad \text{if } (m_e/m_\alpha)^{1/4} \ll 1, \quad (1.1)$$

where  $q_i$  and  $q_\alpha$  symbolize the electronic and nuclear coordinates and  $m_e$  and  $m_\alpha$  refer to electronic and nuclear mass. The Born-Oppenheimer approximation that is basic to quantum chemistry, introduces little error for the ground electronic states of diatomic molecules. [8]

There are, however, many chemical events in which the nuclear motion is not governed by a single adiabatic potential energy surface. Development of the theory of nonadiabatic chemistry started in 1932 by the works of Landau, [9] Zener [10], Stueckelberg [11], and London [12].

For electronically excited molecules, the electron and nuclear dynamics can be strongly coupled [13]. This is the case for many important non-adiabatic dynamical phenomena [14], such as internal conversion (for example, photoisomerization) [15–18], intersystem crossing [19–22], charge and energy transport in many technological applications (for example, photovoltaics, catalysis and energy storage) [23–27], and natural systems (for example, photosynthetic complexes) [28, 29]. The failure of the Born-Oppenheimer approximation can, for example, result from the irradiation of a system with light that brings the molecule into its electronically excited states.

Modeling the nonadiabatic dynamical processes is computationally expensive and

therefore different strategies have been developed for the efficient simulation of such processes. The ideal way to treat the electronically excited molecules would be to solve the time-dependent Schrödinger equation (TDSE) taking into account all nuclear and electronic degrees of freedom and external fields. Multiconfigurational time-dependent Hartree (MCTDH) [30], is one of the popular methods that have been used to describe the multidimensional dynamics.

The full quantum mechanical solution of the time-dependent Schrödinger equation to describe the photochemistry of molecular systems is computationally unaffordable if all nuclear degrees of freedom and a broad spectrum of excited states are to be considered, especially for medium to large systems. It might, however, be possible to treat the system quantum mechanically at the cost of freezing all, or part of the nuclear degrees of freedom (dimension reduction). In this approach one usually needs to apply different kinds of approximations which will affect the accuracy of such calculations.

An alternative approach to the full quantum mechanical description of nonadiabatic phenomena would be nonadiabatic mixed quantum-classical dynamics [31] where the nuclear degrees of freedom are treated classically, and the electronic degrees of freedom quantum mechanically.

Several nonadiabatic mixed quantum-classical dynamics based approaches have, so far, been developed for treating the nonadiabatic dynamical processes [31], including trajectory surface hopping, mean-field Ehrenfest, mixed quantum-classical Liouville equation [32–34], the mapping approach [35, 36], and the coupled-trajectories mixed quantum-classical method [37]. Among the approaches mentioned above, this work builds on the basis of the trajectory surface hopping method. This method is explained in chapter 2. The bottleneck of such calculations is the electronic structure calculations discussed in the following.

For an accurate picture of nuclear dynamics and fragmentation patterns one needs to

calculate the electronic structure accurately. Accurate electronic structure calculations of a large number of excited states along with several nuclear degrees of freedom including bond breaking is a very challenging task. The highest accuracy for calculating coupled potential energy surfaces over the entire range of nuclear geometries can be obtained with multireference methods, such as the multireference configuration interaction (MRCI) [38] approach. Energy gradients as well as derivative couplings can be obtained using analytic gradient techniques [39–41], which allows for the simulation of fragmentation processes. Due to the high computational cost of MRCI calculations, they are limited to simulation of a few atoms and cannot handle large systems. Furthermore, only a few excited states can be treated with MRCI and therefore it is not a feasible approach for describing the broad range of electronic states accessed in the XUV radiation regime.

Multiconfigurational methods have been widely used to describe ultrafast dynamics, particularly complete active space self-consistent field (CASSCF) [42] and its second-order perturbation theory extension (CASPT2) [43–48], which recovers part of the dynamical correlation energy that is missing from a CASSCF calculation [49]. However, it should be noted that the shape of the potential energy surfaces and as a result, the photoinduced dynamics can be strongly influenced by the choice of the active space and the basis set [50]. Active space selection is a very delicate task and one needs to have a benchmark for its validation [51]. CASSCF applications are also limited by the number of atoms and the size of active spaces [51] and it becomes impractical for large active spaces, large systems, and large number of electronic states, which are typical for XUV-induced dynamics.

Other wave function-based methods that have been successful in many aspects of excited state chemistry are the approximate coupled-cluster method of second order

(CC2) [52] as an approximation to the CCSD method [52, 53], and the algebraic-diagrammatic-construction (ADC) [54–61]. These methods are not as expensive as MRCI or CAS methods but they have many limitations. Both methods are based on a single reference determinant and thus cannot describe situations with static correlation. Furthermore, these methods have problems describing the topology around surface crossings. Tuna et al. [62] have previously assessed the performance of these two methods for the description of  $S_0$  and  $S_1$  reaction paths as well as the branching space of the conical intersection involved in the photoisomerization process of penta-2,4-dieniminium cation. They showed that CC2 suffers from the existence of many artifacts around the surface crossing and that ADC(2) and ADC(3) methods are unable to describe the correct topology of the surface crossing. Plasser et al. [62, 63] showed that CC2 is an unsuitable method for surface hopping molecular dynamics simulations due to numerical instabilities arising from the non-Hermitian formulation of CC2.

Another approach that has been widely applied to calculate excited state properties [64–68] and ultrafast dynamics [69] is time-dependent density functional theory (TDDFT), [70] which is applicable to relatively large systems. The results of TDDFT calculations strongly depend on the exchange-correlation (XC) functional employed and on the fraction of Hartree-Fock exchange included. Therefore, the excitation energies are highly dependent on the choice of functional, which makes the TDDFT calculations ambiguous if there is no benchmark to validate the excitation energies [71, 72]. It is known that the typical XC functionals used in DFT ground state calculations, such as gradient-corrected BP86 [73, 74] or hybrid-type B3LYP [75, 76], show wrong asymptotic behavior [77] for excited states. It has been shown that TDDFT employing standard functionals leads to dramatic failures for the two lowest lying singlet  $\pi \rightarrow \pi^*$  states of linear acenes from two (naphthalene) up to eight ring (octaacene) acenes

[78, 79]. Furthermore, it has been shown that the popular linear-response TDDFT approach suffers from convergence problems near conical intersections and is incapable of properly describing the topography of potential energy surfaces at crossing points in the studied systems. This makes TDDFT less applicable for modeling non-adiabatic relaxation processes [80].

Working in the XUV regime, one usually encounters cationic states of a molecule and therefore an accurate and efficient theory capable of describing the photochemistry of cations would come very useful for interpreting, predicting, and directing the experiments.

A computationally efficient ab initio approach for simulation of excited state dynamics of cations following XUV photoionization is a Koopmans' theorem based approach [81, 82], which is applicable to the XUV induced dynamics of rather large systems such as polycyclic aromatic hydrocarbons (PAHs) that will be discussed in chapter 4. A Koopmans' theorem based approach does not take into account orbital relaxation and electron correlation effects which can lead to deviations in binding energies. Additionally, only states corresponding to the removal of an electron from a (valence) orbital can be treated within this approach and thus shake-up or satellite states are neglected, which become more important at higher binding energies. This approach has previously been successfully applied to describe correlated proton-electron hole dynamics of ionized  $[\text{H}(\text{H}_2\text{O})_{21}]^+$  [81] and ultrafast dynamics of acetylene cations after XUV photoionization [82], where no fragmentation involving breakage of covalent bonds was involved. In addition, we have employed the same approach in order to study the XUV photochemistry of the Benzene Radical Cation (see chapter 4).

Another example where we have used a Koopmans' theorem based approach is the description of the photochemistry of  $\text{CH}_2\text{O} \cdots \text{ClF}$ , a halogen-bonded dimer. We have

studied vertical ionization-induced charge transfer and structural dynamics of the positively charged dimer. Halogen bonding is involved in a wide range of applications including medicinal chemistry [83, 84], anion recognition and sensing [85–90], anion transport across the biological and synthetic lipid bilayer membranes [91, 92], and across the plasma membrane in living cells [92], anion-templated self-assembly, and organocatalysis [93], the design of supramolecular photofunctional materials [94, 95] and catalysis [96]. Studying the non-Born–Oppenheimer charge transfer and structural dynamics in halogen bonded clusters will open up new opportunities to further expand the applications of halogen bonding and to better understand its nature.

Ground-state halogen bonding is considered to be a primarily electrostatic interaction [94, 97–100] between an electron donor and a region of positive electrostatic potential on the elongation of the covalent bond on a polarized halogen atom attached to electron-withdrawing groups. Altering the electrostatic interaction will, therefore, change the strength of the halogen bond. Following ionization, the charge distribution of a halogen-bonded dimer will change, thus leading to a change in the halogen bonding strength. It should be noted that the initial charge distribution following ionization depends on the molecular orbital from which an electron is removed. The charge distribution then undergoes very fast dynamics until the system reaches a new equilibrium. Tracking the temporal evolution of charge distribution and structural parameters following ionization out of different molecular orbitals has a significant outcome; it gives information on how to transiently manipulate the halogen-bond interaction through ionization. It also helps to understand the contribution of each molecular orbital to the ground-state halogen bonding.

We investigated the vertical ionization-induced charge transfer in the halogen-bonded dimer  $\text{CH}_2\text{O}\cdots\text{ClF}$  beyond the Born–Oppenheimer approximation. It should be noted

that the charge transfer differs from charge migration; charge migration is, by convention, a time-dependent oscillation of the charge density in a molecule driven by the coherent superposition of electronic states, whereas charge transfer involves nuclear motion. [101] Vertical ionization has so far been used as an efficient tool in order to initiate the charge migration in isolated molecules [102–108], hydrogen-bonded [109, 110] and various other types of noncovalent-bonded clusters [111–113]. Chandra et al. have, for the first time, recently investigated the pure electronic charge migration through non-hydrogen noncovalent bonds, including halogen bonds, using the Born–Oppenheimer approximation. [111–113]. Charge migration mediated by halogen bonds has applications in the development of bright and practical purely organic phosphors. [101, 114].

In chapter 5, we focus on the simple halogen-bound dimer  $\text{CH}_2\text{O} \cdots \text{ClF}$ , which involves the interaction of a carbonyl group with a Cl atom. The abundance of carbonyl-halogen contacts in the protein data bank makes it an attractive subject for fundamental studies. The special selectivity of halogen bonds for carbonyl oxygens in the polypeptide backbone in the crystal structures of protein kinase complexes with halogen-substituted inhibitors points to the special importance of carbonyl-halogen interactions. [115] The high selectivity and the strong directional dependence of halogen bonds are the unique chemical properties that make them useful for the development of protein inhibitors and drugs [115–120].

As already mentioned, the choice of the electronic structure method in the quantum classical calculations depends on factors such as system size, the number of excited states involved, and the complexity and nature of a chemical reaction. For example, since water is a relatively small molecule and we were not interested in a large number of excited states, in a study presented in chapter 3, we have used methods (CASSCF) that are more advanced than the Koopmans’ theorem in order to study the

VUV-induced dynamics of H<sub>2</sub>O and its deuterated isotopologues in the first excited state ( $\tilde{A}^1B_1$ ). We provided theoretical support to our collaborators that conducted an experiment on this system. In the following I present a short introduction to the photodissociation reaction of water, for the theoretical details see chapter 3.

The VUV-induced photodissociation reaction of water via the first excited state has been the subject of an abundance of theoretical and experimental studies, as a prototype for a repulsive, barrierless, adiabatic dissociation reaction. The potential energy surface [121, 122] of the first excited state has been calculated with high precision by Staemmler and Palma [121]. This is a widely utilized calculation and has been further improved by different groups [123–125]. Based on these calculations previous theoretical studies focused on the interpretation of the  $\tilde{A}^1B_1$  absorption spectrum [126–129], as well as on the rotational fine-structure of the dissociation products [130]. These calculations are supported by a multitude of experiments, such as high precision absorption spectroscopy [131], Rydberg-tagging experiments [132, 133], photoemission spectroscopy [134] or studies of isotope effects on the dissociation dynamics [126, 135–139].

With the availability of laser systems capable of generating femtosecond VUV pulses, experimental studies have been extended to the time domain. Farmanara *et al.* [140, 141] were able to identify an upper bound of 20 fs for the photodissociation time constant in the  $\tilde{A}^1B_1$  state, limited by their temporal resolution in a 155 nm single-color pump-probe experiment. Furthermore, Trushin *et al.* [142] performed a VUV-pump multiphoton IR-probe experiment and were able to identify different time windows for this pump-probe scheme, defining the time the molecular wave-packet needs to exit the Franck-Condon region (1.8 fs) and leave the 1+5 photon ionization window (3.5 fs). In addition to these experimental studies Imre and Zhang [128], as well as Henriksen *et al.* [127] deduced the time a wave-packet created by vertical excitation of the  $\tilde{A}^1B_1$

state needs to leave the Franck-Condon region is 5 fs.

To gain further insight into the wave-packet dynamics, our collaborators utilized 16-fs, 161-nm pulses [143] to study the photodissociation dynamics of H<sub>2</sub>O and its deuterated isotopologues in the first excited state. By combining the ultrashort 161-nm pulses with a novel single-shot VUV pump/probe approach [144], the experiment was able to disclose sub-10-fs photodissociation dynamics, while greatly reducing acquisition time by collecting a complete pump-probe data set at the repetition rate of the laser system. In addition to the pump-probe measurement, the experimental group determined the instrument response function by means of an intensity autocorrelation of the VUV pulse, enabling deconvolution of the investigated ultrafast dynamics.

This VUV pump/probe approach complements previous studies relying on multi-photon ionization in the probe step, where a sufficiently high infrared field strength is needed. These strong fields may influence the molecular potentials [145] and affect the intrinsic molecular dynamics, as discussed in a previous study on the photodissociation of O<sub>2</sub> [146]. In the weak-field approach of the experiment in Ref.[143] these effects, as well as the influence of intermediate states, which might be accessed resonantly in the probe step, are excluded, allowing a simplified theoretical description of the experimental observables for the molecular dynamics. Furthermore, the weak-field case represents a valuable reference for assessing the relevance of strong-field effects at higher intensities, but lower photon energies.

## 1.1 Structure of this thesis

In chapter 2, I explain the theory of nonadiabatic mixed quantum-classical dynamics based on Tully's fewest switches algorithm [147]. The theory is implemented in an in-house program package and used to simulate the photochemistry of the molecular species presented in this thesis.

In chapter 3, I show an application in the context of a pump-probe experiment studying the VUV induced photodissociation dynamics of water and its deuterated isotopologues supported by our theoretical data. We used a mixed quantum-classical approach in which the nuclear motions were treated classically by Newton's equations of motion and the electrons were described quantum mechanically. The water molecule is small enough to allow us to use relatively expensive methods. We used complete active space self-consistent field, CASSCF(6,4), for on-the-fly ab initio calculations of the electronic structure. In order to increase the accuracy of calculations we then reevaluated the CASSCF energies with the single point calculations at the multi-reference single and doubles configuration interaction level with eight correlated electrons and seven active orbitals, MR-CISD (8,7). Our theoretical calculations were in a very good agreement with the data obtained from the pump-probe experiments.

Chapter 4 is devoted to XUV induced non-adiabatic dynamics and photodissociation of the benzene radical cation, where we used a similar mixed quantum-classical approach as in chapter 3. It is challenging to obtain a complete picture of the dynamics and dissociation patterns of the benzene radical cation after XUV irradiation (10–124 eV), as one has to deal with several nuclear degrees of freedom, as well as a broad range of excited states and fragmentation channels. Therefore a Koopmans' theorem based approach was employed for electronic structure calculations to describe the non-adiabatic dynamics of singly ionized benzene on fifteen coupled potential energy surfaces. The aim of this study was to assess the possibility of utilizing Koopmans' theorem to study the XUV induced photodissociation of medium-sized to large systems using ab initio classical trajectory calculations within the fewest switches surface hopping (FSSH) scheme [147]. We addressed two fundamental aspects of the XUV photochemistry: the time resolved relaxation of the electronically excited states through internal conversion and the time-resolved state-specific fragmentation dynamics. Our theoretical approach

showed a good performance for the non-adiabatic relaxation process. Our approach, however, underestimated the dissociation probability compared to experiments. This highlights the challenges in simulating XUV induced photochemistry of medium-sized systems discussed in the last section.

In chapter 5, I used the same theoretical approach as in chapter 4 to investigate the temporal evolution of the structure and the charge of the  $\text{CH}_2\text{O}\cdots\text{ClF}$  dimer after removing an electron from one of its three outer-valence molecular orbitals. The dimer involves the interaction of a carbonyl group with a Cl atom; an abundant interaction in the protein data bank. I decided to study this dimer in order to inspire further research into the control of halogen-bond interactions through ionization or electronic excitation, which has potential applications in drug design and drug delivery. In addition, the results of this fundamental study have potential applications in other areas such as solar energy conversion, and anion recognition.

Finally, I close this work with a short summary and outlook.

## Chapter 2

# Introduction to Theoretical Framework

### 2.1 Born-Oppenheimer approximation

Chemical dynamics involves motions of electrons and nuclei of atoms. Nuclei are much heavier than electrons therefore they move much slower than the electrons. Therefore during the time of a cycle of electronic motion (in a classical picture), the change in the nuclear configuration is negligible [8]. Thus we can, with a very good approximation (Born-Oppenheimer approximation), solve the Schrödinger equation by freezing all the nuclear degrees of freedom.

First we solve the Schrödinger equation for a purely electronic Hamiltonian ( $\hat{H}_{Pure-el}$ , Eq. 2.1) in a fixed nuclear configuration and set the nuclear kinetic energy ( $T_n$ , Eq. 2.2) to zero.

$$\hat{H}_{Pure-el} = -\frac{\hbar^2}{2m_e} \sum_i \nabla_i^2 - \sum_\alpha \sum_i \frac{Z_\alpha e^2}{4\pi\epsilon_0 L_{i\alpha}} + \sum_j \sum_{i>j} \frac{e^2}{4\pi\epsilon_0 L_{ij}}, \quad (2.1)$$

$$T_n(R) = -\frac{\hbar^2}{2} \sum_\alpha \frac{1}{m_\alpha} \nabla_\alpha^2, \quad (2.2)$$

## 2.1. Born-Oppenheimer approximation

---

where  $\alpha$  refers to the nucleus with atomic number  $Z_\alpha$ ,  $i$  and  $j$  refer to electrons,  $\varepsilon_0$  is the vacuum permittivity,  $L_{i\alpha} = |\mathbf{r}_i - \mathbf{R}_\alpha|$  is the distance between electron  $i$  and nucleus  $\alpha$ ,  $L_{ij} = |\mathbf{r}_i - \mathbf{r}_j|$  is the distance between electrons  $i$  and  $j$ , and  $\mathbf{r}$  and  $\mathbf{R}$  refer to the electronic and nuclear positions, respectively.

The  $\hat{H}_{Pure-el}$  consists of: kinetic energy of the electrons ( $T_e$ ),

$$T_e(r) = -\frac{\hbar^2}{2m_e} \sum_i \nabla_i^2, \quad (2.3)$$

potential energy of the repulsion between the electrons ( $V_e$ ),

$$V_e(r) = \sum_j \sum_{i>j} \frac{e^2}{4\pi\varepsilon_0 L_{ij}}, \quad (2.4)$$

and the potential energy of the attractions between the electrons and the nuclei ( $V_{en}$ ),

$$V_{en}(r, R) = -\sum_\alpha \sum_i \frac{Z_\alpha e^2}{4\pi\varepsilon_0 L_{i\alpha}}. \quad (2.5)$$

The repulsion term between the nuclei  $\alpha$  and  $\beta$  is given by

$$V_{nn}(R) = \sum_\alpha \sum_{\beta>\alpha} \frac{Z_\alpha Z_\beta e^2}{4\pi\varepsilon_0 L_{\alpha\beta}}, \quad (2.6)$$

where  $L_{\alpha\beta} = |\mathbf{R}_\alpha - \mathbf{R}_\beta|$  is the distance between nuclei  $\alpha$  and  $\beta$  with atomic numbers  $Z_\alpha$  and  $Z_\beta$ .

In order to obtain the electronic Hamiltonian including nuclear-repulsion ( $H_{el}$ , Eq. 2.7), we add the nuclear-repulsion term ( $V_{nn}(R)$ , Eq. 2.6) to the purely electronic Hamiltonian (Eq. 2.1). Thus,

$$\hat{H}_{el} = -\frac{\hbar^2}{2m_e} \sum_i \nabla_i^2 - \sum_\alpha \sum_i \frac{Z_\alpha e^2}{4\pi\varepsilon_0 L_{i\alpha}} + \sum_j \sum_{i>j} \frac{e^2}{4\pi\varepsilon_0 L_{ij}} + \sum_\alpha \sum_{\beta>\alpha} \frac{Z_\alpha Z_\beta e^2}{4\pi\varepsilon_0 L_{\alpha\beta}}. \quad (2.7)$$

It should be noted that the  $V_{nn}(R)$  as well as the  $L_{\alpha\beta}$  are not variables in a fixed nuclear geometry. Therefore the electronic coordinates are the only variables in Eq. 2.7. The electronic Schrödinger equation reads:

$$\hat{H}_{el}(\mathbf{r}; \mathbf{R})\Psi_{el}(\mathbf{r}; \mathbf{R}) = E_{el}(\mathbf{R})\Psi_{el}(\mathbf{r}; \mathbf{R}), \quad (2.8)$$

where the electronic wave function,  $\Psi_{el}(\mathbf{r}; \mathbf{R})$ , and the electronic energies,  $E_{el}$ , depend parametrically on the nuclear coordinates,  $\mathbf{R}$ , and directly on the electronic coordinates,  $\mathbf{r}$ .  $E_{el}(\mathbf{R})$  in Eq. 2.8 would be a point on the potential energy surface. Solving the electronic Schrödinger equation within the Born-Oppenheimer approximation (2.8) for a series of different (fixed) nuclear configurations gives the adiabatic (Born-Oppenheimer) potential energy surfaces.

However, for highly excited molecules electron and nuclear dynamics can be strongly coupled leading to non-Born–Oppenheimer (nonadiabatic) dynamics [13]. In the following, I present a theory for describing the nonadiabatic dynamics of the molecular systems.

## 2.2 Tully’s fewest switches algorithm

Tully’s fewest switches algorithm [147] is one of the most popular mixed quantum-classical methods for treating nonadiabatic dynamics in molecular systems. In the following, the derivation of the Tully’s approach, implemented in our in-house code, chemical dynamics toolkit (CDTK), is shown. For the derivations presented here I have used several books, reviews, and papers as references [3, 31, 148–155].

Here I use the  $\hat{H}_{el}$  electronic Hamiltonian (Eq. 2.8) to treat the quantum (electronic) part. It should be noted that the electronic Hamiltonian here includes the nuclear-repulsion term. The classical Hamiltonian describing the kinetic energy of the

## 2.2. Tully's fewest switches algorithm

---

nuclei is written as:

$$H_{class.n}(\mathbf{R}, \mathbf{P}) = \sum_{\alpha} \frac{1}{2m_{\alpha}} \mathbf{P}_{\alpha}^2, \quad (2.9)$$

where  $\mathbf{P}_{\alpha} = m_{\alpha} \frac{d}{dt}(\mathbf{R}_{\alpha}(t))$  is the momentum of nucleus  $\alpha$  with mass  $m_{\alpha}$ . The equation of motion for the electrons is given by the time dependent Schrödinger equation:

$$i\hbar \frac{\partial \Psi_{el}(\mathbf{r}, t; \mathbf{R}(t))}{\partial t} = \hat{H}_{el}(\mathbf{r}; \mathbf{R}(t)) \Psi_{el}(\mathbf{r}, t; \mathbf{R}(t)), \quad (2.10)$$

In the Tully's fewest switches surface hopping approach the nuclear motion is governed by a single electronic state ( $\Psi_{el}^{current}$ ) at each instant of time where the  $\Psi_{el}^{current}$  wave function is considered to be a Born-Oppenheimer wave function. As will be discussed in 2.2.2, an ensemble of trajectories must be calculated to determine the nuclear wave packet. The  $\Psi_{el}^{current}$  that can change in time, can also differ from one trajectory to other.

Within Tully's approach, stochastic methods determine quantum hopping from the current state to any other electronic state. In order to obtain the probability of quantum hops we first expand the time-dependent electronic wave function as a linear combination of electronic states:

$$\Psi_{el}(\mathbf{r}, t; \mathbf{R}(t)) = \sum_a c_a(t) \Psi_{el}^a(\mathbf{r}; \mathbf{R}(t)), \quad (2.11)$$

where  $\Psi_{el}^a$  is the Born-Oppenheimer wave function for state  $a$ , and  $c_a(t)$  is a time-dependent expansion coefficient. The term  $c_a^*(t)c_a(t)$  is the probability of finding the system in the adiabatic state  $a$  at time  $t$ . Substituting Eq. 2.11 in the quantum equation of motion (Eq. 2.10) and projecting on each adiabatic electronic state  $\Psi^b(\mathbf{r}; \mathbf{R})$

gives:

$$\langle \Psi^b(\mathbf{r}; \mathbf{R}) | i \frac{\partial}{\partial t} \sum_a c_a(t) \Psi^a(\mathbf{r}; \mathbf{R}) \rangle = \langle \Psi^b(\mathbf{r}; \mathbf{R}) | \hat{H}_{el}(\mathbf{r}; \mathbf{R}(t)) | \sum_a c_a(t) \Psi^a(\mathbf{r}; \mathbf{R}) \rangle, \quad (2.12)$$

The LHS of Eq. 2.12 can be written as

$$\begin{aligned} \langle \Psi^b(\mathbf{r}; \mathbf{R}) | i \frac{\partial}{\partial t} \sum_a c_a(t) \Psi^a(\mathbf{r}; \mathbf{R}) \rangle &= i \sum_a \frac{dc_a(t)}{dt} \langle \Psi^b(\mathbf{r}; \mathbf{R}) | \Psi^a(\mathbf{r}; \mathbf{R}) \rangle \\ &+ i \sum_a c_a(t) \langle \Psi^b(\mathbf{r}; \mathbf{R}) | \frac{\partial}{\partial t} \Psi^a(\mathbf{r}; \mathbf{R}) \rangle. \end{aligned} \quad (2.13)$$

Assuming the eigenfunctions of  $\hat{H}_{el}(\mathbf{r}; \mathbf{R}(t))$  to be orthonormal gives:

$$\langle \Psi^b(\mathbf{r}; \mathbf{R}) | i \frac{\partial}{\partial t} \sum_a c_a(t) \Psi^a(\mathbf{r}; \mathbf{R}) \rangle = i \frac{dc_b(t)}{dt} + i \sum_a c_a(t) \langle \Psi^b(\mathbf{r}; \mathbf{R}) | \frac{\partial}{\partial t} \Psi^a(\mathbf{r}; \mathbf{R}) \rangle. \quad (2.14)$$

And by using the chain rule:

$$\langle \Psi^b(\mathbf{r}; \mathbf{R}) | \frac{\partial}{\partial t} \Psi^a(\mathbf{r}; \mathbf{R}) \rangle = \langle \Psi^b(\mathbf{r}; \mathbf{R}) | \frac{\partial}{\partial \mathbf{R}} \Psi^a(\mathbf{r}; \mathbf{R}) \rangle \cdot \frac{d\mathbf{R}}{dt}. \quad (2.15)$$

Finally the LHS of Eq. 2.12 becomes:

$$\begin{aligned} \langle \Psi^b(\mathbf{r}; \mathbf{R}) | i \frac{\partial}{\partial t} \sum_a c_a(t) \Psi^a(\mathbf{r}; \mathbf{R}) \rangle &= i \frac{dc_b(t)}{dt} + i \sum_a c_a(t) \langle \Psi^b(\mathbf{r}; \mathbf{R}) | \frac{\partial}{\partial \mathbf{R}} \Psi^a(\mathbf{r}; \mathbf{R}) \rangle \cdot \frac{d\mathbf{R}}{dt} \\ &= i \frac{dc_b(t)}{dt} + i \sum_a c_a(t) \mathbf{d}_{ab} \cdot \frac{d\mathbf{R}}{dt}, \end{aligned} \quad (2.16)$$

where  $\mathbf{d}_{ab}$  is the nonadiabatic coupling vector,  $\mathbf{d}_{ab} \cdot \frac{d\mathbf{R}}{dt}$  is an element of the electronic Hamiltonian matrix responsible for nonadiabatic couplings, and  $\frac{d\mathbf{R}}{dt}$  is the classical nuclear velocity vector.

The RHS of Eq. 2.12 can be written as

$$\begin{aligned}
 & \langle \Psi^b(\mathbf{r}; \mathbf{R}) | \hat{H}_{el}(\mathbf{r}; \mathbf{R}(t)) | \sum_a c_a(t) \Psi^a(\mathbf{r}; \mathbf{R}) \rangle & (2.17) \\
 & = \sum_a c_a(t) \langle \Psi^b(\mathbf{r}; \mathbf{R}) | \hat{H}_{el}(\mathbf{r}; \mathbf{R}(t)) | \Psi^a(\mathbf{r}; \mathbf{R}) \rangle \\
 & & = \sum_a c_a(t) \delta_{ab} E_a(R(t)) \\
 & & = c_b(t) E_b(R(t))
 \end{aligned}$$

where  $E_a(R(t))$  and  $E_b(R(t))$  are the potential energy surfaces of the electronic states  $a$  and  $b$ , respectively. Inserting Eqs. 2.16, 2.17 into 2.12 results in a quantum equation of motion for the coefficients  $c_a(t)$ :

$$\frac{dc_b(t)}{dt} = - \sum_a \left[ \frac{i}{\hbar} \delta_{ab} E_a(R(t)) + \mathbf{d}_{ab} \cdot \frac{d\mathbf{R}}{dt} \right] c_a(t). \quad (2.18)$$

In the following, Eq. 2.18 is used to calculate the probability of hopping from state  $b$  to any other state within  $t$  and  $t' = t + \Delta t$  time interval. Suppose  $N_{total}$  is the total number of trajectories out of which  $N_b$  trajectories populate the state  $b$  at time  $t$ :

$$N_b = c_b^* c_b \cdot N_{total}. \quad (2.19)$$

In the next step, I calculate the probability of reducing the number of trajectories from  $N_b$  at time  $t$ , to  $N_b'$  at time  $t'$ , where  $N_b - N_b' = \Delta N$ . In order to have the minimum number of hops (fewest switches),  $\Delta N$  transitions are required from state  $b$  to any other state and zero transitions from any other state to state  $b$ , as illustrated schematically in Figure 2.1. Finally, the probability of a hop from state  $b$  within the

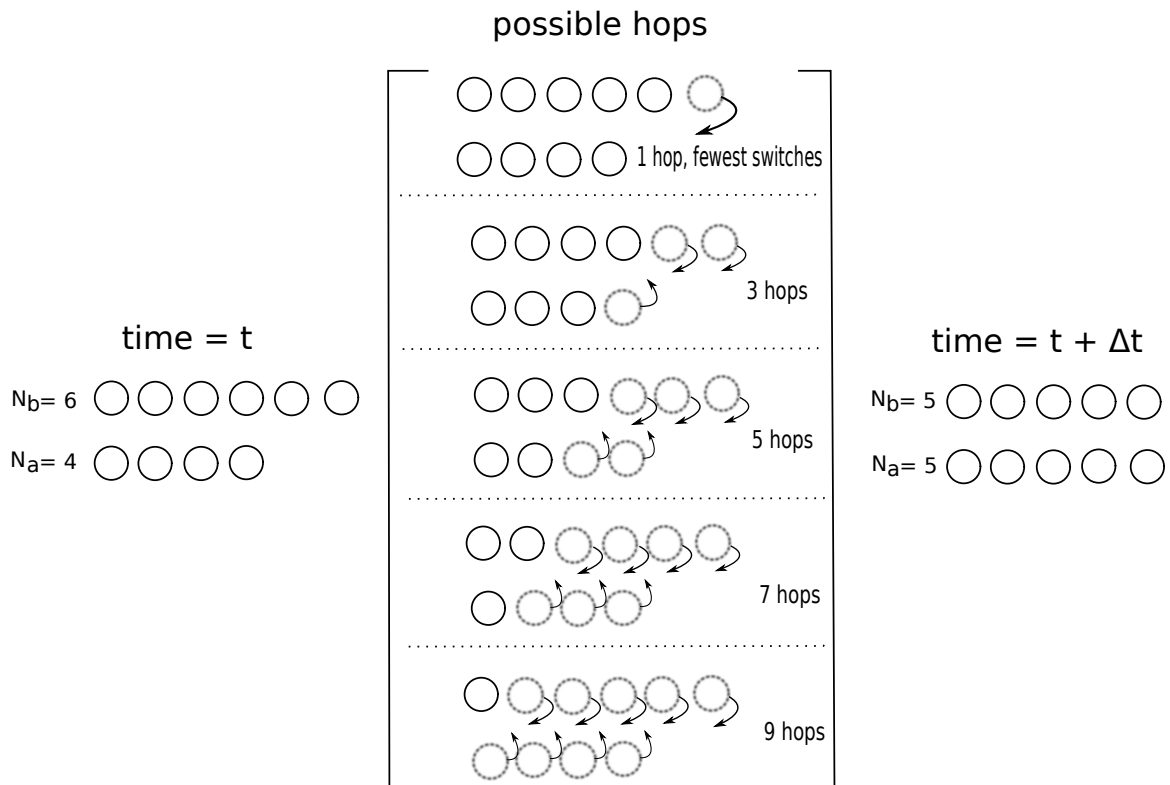


FIGURE 2.1: A system which contains the states  $a$  and  $b$ , where the number of trajectories in the state  $b$  equals 6 at time  $t$  and is reduced to 5 at time  $t'$ . The middle panel illustrates the various possible switches that bring the system from the population distribution at time  $t$  to the one at time  $t'$ . The first possibility shows how this distribution can be achieved with the minimum number of transitions.

## 2.2. Tully's fewest switches algorithm

---

time interval  $\Delta t$  would become:

$$P_{b \rightarrow \text{any other state}} = \frac{\Delta N}{N_b} = \frac{c_b^* c_b - c_b^{*'} c_b'}{c_b^* c_b}. \quad (2.20)$$

If the time interval is sufficiently small:

$$P_{b \rightarrow \text{any other state}} \approx -\frac{\frac{d}{dt}(c_b^* c_b) \Delta t}{c_b^* c_b}, \quad (2.21)$$

The  $\frac{d}{dt}(c_b^* c_b)$  in Eq. 2.21 can be re-written as:

$$\frac{d}{dt}(c_b^* c_b) = \dot{c}_b^* c_b + c_b^* \dot{c}_b = 2 \operatorname{Re}(c_b^* \dot{c}_b). \quad (2.22)$$

Finally, the probability of a hop from state  $b$  to any other state within  $\Delta t$  is:

$$P_{b \rightarrow \text{any other state}} = -\frac{2 \operatorname{Re}(c_b^* \dot{c}_b)}{c_b^* c_b} \cdot \Delta t. \quad (2.23)$$

Inserting Eq. 2.18 into Eq. 2.23 gives:

$$P_{b \rightarrow \text{any other state}} = \sum_a \frac{2 \operatorname{Re} \left( \mathbf{d}_{ab} \cdot \frac{d\mathbf{R}}{dt} c_b^* c_a \right)}{c_b^* c_b} \cdot \Delta t. \quad (2.24)$$

In order to calculate the probability of hop from state  $b$  to state  $a$  it is enough to remove the sum from Eq. 2.25:

$$P_{b \rightarrow a} = \frac{2 \operatorname{Re} \left( \mathbf{d}_{ab} \cdot \frac{d\mathbf{R}}{dt} c_b^* c_a \right)}{c_b^* c_b} \cdot \Delta t. \quad (2.25)$$

In order to determine the active state among the electronic states, the algorithm draws a uniformly distributed random number  $\zeta \in (0, 1)$  at each time step and compares it

with the hopping probability. A transition from state  $b$  to state  $a$  occurs if:

$$P_{b \rightarrow (a)} < \zeta < P_{b \rightarrow (a+1)}, \quad (2.26)$$

where  $P_{b \rightarrow (a)}$  is the sum of the transition probabilities for the first  $a$  states:

$$P_{b \rightarrow (a)} = \sum_{n \leq a} P_{b \rightarrow n}. \quad (2.27)$$

The basic idea of the fewest switches surface hopping is described above. In the following I will discuss the secondary aspects of the fewest switches surface hopping.

### 2.2.1 Kinetic energy adjustment

If a hop occurs from state  $b$  to state  $a$ , the electronic energy of the system changes from  $E_{el}^b$  to  $E_{el}^a$ . In order to conserve the energy of a molecular system during an electronic transition, the velocity of the nuclei has to be re-scaled after every hop. In Tully's approach, the velocity adjustment is done to the component of velocity in the direction of the nonadiabatic coupling vector ( $\mathbf{d}_{ab}$ ) at the position of the transition ( $R$ ):

$$\dot{\mathbf{R}}_a = \dot{\mathbf{R}}_b - \lambda_{ba} \mathbf{U} \quad (2.28)$$

where  $\dot{\mathbf{R}}_a$  is the nuclear velocity in state  $a$  (after the hop) and  $\dot{\mathbf{R}}_b$  is the nuclear velocity in state  $b$  (before the hop),  $\mathbf{U} = \frac{\mathbf{d}_{ab}}{|\mathbf{d}_{ab}|}$  is the unit vector in the direction of nonadiabatic coupling vector, and  $\lambda_{ba}$  is the scaling factor to be determined. After a

hop has occurred, the change in the kinetic energy is given by [153]:

$$\begin{aligned}
 \Delta T &= \frac{1}{2} \sum_{\alpha} m_{\alpha} (\dot{\mathbf{R}}_a)^2 - \frac{1}{2} \sum_{\alpha} m_{\alpha} (\dot{\mathbf{R}}_b)^2 & (2.29) \\
 &= \frac{1}{2} \sum_{\alpha} m_{\alpha} (\dot{\mathbf{R}}_b - \lambda_{ba} \mathbf{U})^2 - \frac{1}{2} \sum_{\alpha} m_{\alpha} (\dot{\mathbf{R}}_b)^2 \\
 &= \frac{1}{2} \sum_{\alpha} m_{\alpha} ((\lambda_{ba} \mathbf{U})^2 - 2\lambda_{ba} \mathbf{U} \dot{\mathbf{R}}_b) \\
 &= \lambda_{ba}^2 \left[ \frac{1}{2} \sum_{\alpha} m_{\alpha} \mathbf{U}^2 \right] - \lambda_{ba} \left[ \sum_{\alpha} m_{\alpha} \mathbf{U} \dot{\mathbf{R}}_b \right].
 \end{aligned}$$

Since energy is conserved, the change in the electronic energy is equal to the change in the kinetic energy [153]:

$$T_a + E_{el}^a = T_b + E_{el}^b \quad (2.30)$$

$$\Delta T = (E_b - E_a) = \lambda_{ba}^2 \left[ \frac{1}{2} \sum_{\alpha} m_{\alpha} \mathbf{U}^2 \right] - \lambda_{ba} \left[ \sum_{\alpha} m_{\alpha} \mathbf{U} \dot{\mathbf{R}}_b \right] \quad (2.31)$$

The above equation can be re-written as:

$$A_{ba} \lambda_{ba}^2 - B_{ba} \lambda_{ba} - (E_b - E_a) = 0. \quad (2.32)$$

If  $B_{ba}^2 - 4A_{ba}(E_b - E_a) < 0$ , Eq. 2.32 has no real solutions. Here we follow Tully's original suggestion where classically forbidden transitions are forbidden while nuclear velocities are maintained. However, if  $B_{ba}^2 - 4A_{ba}(E_b - E_a) > 0$ , the scaling factor would be the solution to 2.32 where the  $\lambda_{ba}$  that accounts for least momentum change is chosen.

### 2.2.2 Ensemble of trajectories

According to the Heisenberg uncertainty principle, the position and the velocity of an object, here nuclei, cannot both be known exactly at the same time. In Tully's

approach, the nuclear wavepacket is approximated by an ensemble of particles that follow some independent trajectories [156]. In Tully’s approach a single electronic state governs the nuclear motion at each instant of time. This electronic state can differ from one trajectory to another. For the above reason and also because of the stochastic nature of hopping, an ensemble of trajectories must be calculated.

For the case studies presented in this thesis, the number of trajectories sampled varies between 20 to 100. To ensure good statistics, at the end of the calculations, the trajectories are divided into the two equal subsets of trajectories. If a similar temporal evolution is observed for the two subsets, we infer good statistics, i.e. the number of trajectories are good enough for a certain molecular dynamics.

### 2.2.3 Generation of initial phase space

In order to sample the initial nuclear coordinates and momenta, two methods have been used in this thesis namely microcanonical normal mode sampling, and Wigner sampling [157]. The details of the two sampling methods are given in 4.1 and ??, respectively.

### 2.2.4 Numerical integration of Newton’s equations

At the beginning of the surface hopping calculations presented here, initial coordinates, velocities, and electronic state, are defined and the gradient of the active state is computed to provide the initial forces on the nuclei. The numerical integration of Newton’s equations is done using the velocity Verlet algorithm [158–160]. It calculates, for time step  $(t + \Delta t)$ , the coordinates  $\mathbf{R}(t + \Delta t)$  and velocities  $\mathbf{v}(t + \Delta t)$  of the nuclei from the corresponding values of these quantities at the previous time step. In this algorithm, the time evolution of the nuclear coordinates  $\mathbf{R}(t)$  is driven by the gradient of the potential at time  $t$  [161]:

$$\mathbf{v}(t + \Delta t/2) = \mathbf{v}(t) + (0.5/m)\mathbf{F}(t)\Delta t, \quad (2.33)$$

$$\mathbf{R}(t + \Delta t) = \mathbf{R}(t) + \Delta t\mathbf{v}(t + \Delta t/2), \quad (2.34)$$

$$\mathbf{F}(t + \Delta t) = \mathbf{F}(\mathbf{R}(t + \Delta t)), \quad (2.35)$$

$$\mathbf{v}(t + \Delta t) = \mathbf{v}(t + \Delta t/2) + (0.5/m)\mathbf{F}(t + \Delta t)\Delta t, \quad (2.36)$$

where  $m$  represents the mass of the nuclei.

### 2.2.5 Choice of the electronic structure method

In the course of the nonadiabatic quantum classical dynamics, the electronic structure calculations provide us with energies, energy gradients, and nonadiabatic coupling terms. A wrong choice of the electronic structure method would therefore lead to wrong molecular dynamics. In order to obtain accurate dynamics, the electronic structure method should provide not only a correct description of the excitation energies and state ordering around the Franck-Condon region, but also in other parts of the potential energy surfaces accessible to trajectories, including dissociation limits, minimum energy crossing points, etc. In other words, the shape of potential energy surfaces should be correctly described for the entire range of the dynamics.

For the description of single excitation in the Franck-Condon region, which is common for ultraviolet (UV), and visible-induced photochemistry, a single reference (SR) electronic structure method is usually a reliable choice. The simplest approach is to use a Hartree-Fock (HF) determinant as a single reference to build the electronic excitation

and electronic correlation processes which eventually lead to the introduction of the configuration interaction (CI) method. A molecular CI calculation starts with a self-consistent field molecular orbital (SCF MO) or Multi-configurational SCF (MCSCF) calculation to find SCF occupied and virtual molecular orbitals (MOs). The MOs are then used to form configuration state functions (CSFs),  $\Phi_i$ .

The molecular wave function  $|\Psi\rangle$  is a linear combination of the CSFs  $\sum_i b_i \Phi_i$  (Eq. 2.37):

$$|\Psi\rangle = b_0 |\Phi_{ref}\rangle + \sum_{k,a} b_k^a |\Phi_k^a\rangle + \sum_{k>l,a>b} b_{kl}^{ab} |\Phi_{kl}^{ab}\rangle + \sum_{k>l>m,a>b>c} b_{klm}^{abc} |\Phi_{klm}^{abc}\rangle + \dots, \quad (2.37)$$

where  $|\Phi_{ref}\rangle$  is the HF reference/HF determinant. The linear expansion coefficients,  $b_i$ 's, are determined based on the variational method where the coefficients are varied to minimize the energy,  $E = \langle \Psi | \hat{H} | \Psi \rangle / \langle \Psi | \Psi \rangle$ . In the Eq. 2.37, the configuration functions are classified as singly excited, doubly excited, triply excited, etc., according to the number of electrons excited from occupied to virtual orbitals. A truncated CI is defined if some excitation classes are not included in the molecular wave function. The simplest case would be CI singles (CIS) that only includes the first two terms in Eq. 2.37 and results in  $N - 1$  electrons in occupied orbitals and one electron in virtual orbitals. A full CI calculation includes all the possible CSFs with proper symmetry. Because of the huge number of CSFs, a full CI calculation is prohibitively expensive except for very small systems and small basis sets.

A single reference approach is valid if the reference CSF dominates in the CI expansion or it is valid as far as the static electron correlation does not play an important role. This requirement will not be fulfilled in many situations, e.g., covalent bond breaking, or processes that involve many excited states, especially far from the Franck-Condon

region. In these cases, the existence of quasi-degenerate orbitals with similar noninteger occupations and open-shell character would result in the failure of a single reference approach.

Similar to CI is MCSCF which is also based on the variational principle. The molecular wave function of the MCSCF method is a linear combination of CSFs,  $|\Phi_k\rangle$ , where not only the expansion coefficients  $b_k$ , but also the forms of the molecular orbitals in the CSFs are optimized. Because the orbitals are optimized, one can get good results with the inclusion of relatively few CSFs [8]. The most commonly used MCSCF method is the CASSCF method developed by Roos et al. [162]. Within this approach, the molecular orbitals in the CSFs are divided into two main sub-groups of active and inactive orbitals. The inactive orbitals remain doubly occupied in all CSFs. The electrons in active orbitals are called active electrons. One does a full CI and creates all the possible CSFs within the active space by distributing the active electrons among the active orbitals. The CSFs must have the same spin and symmetry eigenvalues as the main state. A CASSCF calculation uses significantly less CSFs compared to full CI. Although a CASSCF calculation cannot recover a significant portion of the correlation energy, it can represent the changes in correlation energy in processes such as geometry changes or chemical reactions. The optimization processes in CASSCF calculations become complicated when several electronic states are described at the same time. In such cases, a state averaged CASSCF (SA-CASSCF) would be a good choice. It optimizes the average energy of all states under consideration and provides a single set of compromise orbitals for all the states. This prevents root-flipping problems during the optimization process.

In order to reduce the computational cost of CASSCF calculations, the restricted active space SCF (RASSCF) method has been introduced. The RASSCF method divides the active space into three subspaces called RAS1, RAS2, and RAS3. RAS2 is

identical to CAS, RAS1 and RAS3 generate further CFSs through certain electronic excitations from RAS1 to RAS3. The problem of CASSCF and RASSCF calculations is the absence of dynamic electron correlation.

A correlated multi-reference description is provided by CAS second order perturbation theory (CASPT2). The CASPT2 method applies perturbation theory to an MCSCF wave function (usually a CASSCF wave function) as a reference function. The second-order perturbation theory extension [43–48] of CASSCF recovers part of the dynamical correlation energy that is missing from a CASSCF calculation [43].

Another popular multireference method that combines the MCSCF and CI methods is called multireference CI (MRCI) method [8]. MRCI method builds on an MCSCF calculation.

The result of an initial MCSCF calculation is a wave function,  $|\Psi_{MCSCF}\rangle$ , that is a linear combination of many CSFs,  $(\Phi_{MCSCF}^1, \Phi_{MCSCF}^2, \Phi_{MCSCF}^3, \dots)$ , with optimized orbitals. In addition, the wave function  $|\Psi_{MCSCF}\rangle$  should ideally show a proper behavior for all nuclear configurations. In the MRCI method, one first does an MCSCF calculation to produce a wave function that is a linear combination of several CSFs with optimized orbitals and that has the proper behavior for all nuclear configurations. One then takes this MCSCF function and moves electrons out of occupied orbitals of the CSFs (called the reference CSFs) into virtual orbitals to produce further CSFs. Most commonly, one does a CISD calculation starting with the MCSCF function, giving an MR-CISD or MRSDCI calculation [8].

MRCI and CASPT2 multireference methods are among the most accurate methods for describing the chemistry of electronically excited states. However some shortcomings are associated with the mentioned methods. See chapter 1 for a detailed discussion on the challenges associated with these methods.

### 2.2.6 Koopmans' theorem

The original Koopmans' theorem states that the first vertical ionization energy of an N-electron system ( $I_{HOMO}$ ) within the Hartree-Fock method and for a closed-shell systems (L) is equal to the negative of the orbital energy of the HOMO of the system [163],

$$I_{HOMO} = -\epsilon_{HOMO}, \quad (2.38)$$

where  $\epsilon_{HOMO}$  is the HOMO's eigenvalue of the HF equation,  $\hat{F}|\phi_i\rangle = \epsilon|\phi_i\rangle$  [8], for the closed-shell system, and  $I_{HOMO}$  is defined in the frozen orbital approximation,

$$I_{HOMO} = E_{frozen}(L_{HOMO}^+) - E_{HF}(L), \quad (2.39)$$

$$E_{frozen}(L_{HOMO}^+) = \langle \Psi(L_{HOMO}^+) | \hat{H} | \Psi(L_{HOMO}^+) \rangle, \quad (2.40)$$

where ( $L_{HOMO}^+$ ) is the cation having a hole in HOMO,  $\Psi(L_{HOMO}^+)$  is a one-determinant wave function of  $L_{HOMO}^+$  using the same HF orbitals,  $E_{HF}(L)$  is the HF energy of the closed shell system  $L$ , and  $\hat{H}$  is the total many-electron Hamiltonian.

Koopmans' theorem assumes that the ionization is due to the immediate loss of an electron without letting the orbitals relax. Therefore, it uses the same set of orbitals to obtain the energies of the N and (N-1) electron systems (the frozen orbital approximation). Koopmans' theorem can be generalized to the removal of an electron from any occupied molecular (valence) orbital to form a cation. The removal of an electron from different orbitals brings the system into different electronic states. The removal of an electron from the HOMO usually leads to the creation of a cation in the electronic ground state. Removing an electron from HOMO-1 creates a cation in its first electronically excited state, etc. The accuracy of Koopmans' theorem usually decreases as the orbital energy decreases. Therefore, it is not recommended to use

the Koopmans' approximation for orbitals with lower energy than the outer valence orbitals. Two main sources of error in Koopmans approximation are the neglect of electron correlation and orbital relaxation effects.

## Chapter 3

# Weak-field few-fs VUV photodissociation dynamics of water isotopologues

- A. Baumann, S. Bazzi, D. Rompotis, O. Schepp, A. Azima, M. Wieland, D. Popova-Gorelova, O. Vendrell, R. Santra, and M. Drescher, “Weak-field few-femtosecond VUV photodissociation dynamics of water isotopologues,” *Physical Review A* 96 (2017). <https://journals.aps.org/prabstract/10.1103/PhysRevA.96.013428>

In this chapter, I present the results of our collaboration with the group of Markus Drescher at the University of Hamburg. The experiment aimed to demonstrate the applications of ultrashort and intense VUV pulses in pump-probe experiments by investigating the VUV-induced photodissociation dynamics of water and its deuterated isotopologues. We have provided theoretical and computational support by: (I) calculating the ultrafast dynamics of the water molecule and its deuterated derivatives in their ground and first excited states, and (II) calculating the photoionization cross sections for 7.7-eV photon energy as a function of geometry. Our theoretical calculations are in a very good agreement with the data obtained from the pump-probe

experiments. I have included both the experimental and theoretical sections to make this chapter more readable.

### 3.1 Experimental methods

35-fs pulses with an energy of up to 15 mJ per pulse delivered by a Ti:Sa laser system relying on chirped-pulse amplification with a central wavelength of 800 nm and a repetition rate of 25 Hz were loosely focused into a length-variable gas cell to generate high-order harmonic radiation. The generation conditions are optimized for fifth harmonic (161.0 nm, 7.7 eV) pulses with a pulse duration of 16 fs and a pulse energy up to 1.1  $\mu\text{J}$  [164].

The single-shot pump-probe technique is described in detail in [144], so here only a short description is provided; a sketch of the optical setup is shown in Figure 3.1. The wavefront of the harmonic beam was split into two halves by a Si wedge cut at

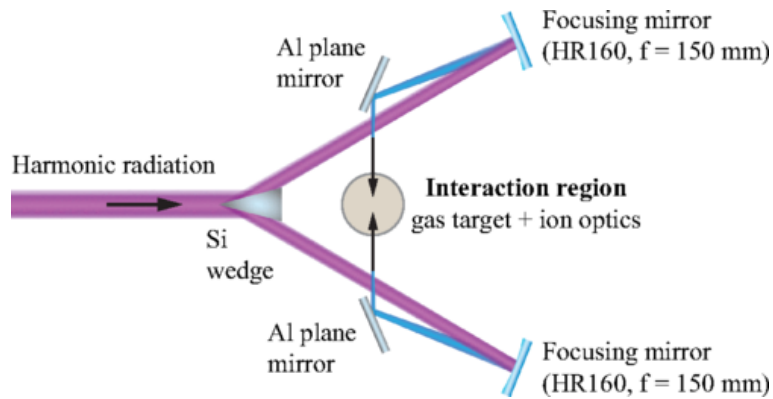


FIGURE 3.1: Sketch of the optical setup used to perform the single-shot pump-probe experiment. © 2017, American Physical Society (APS)

Brewster’s angle for 800 nm, suppressing the fundamental pulse and creating a pair of spatially separated VUV pulses. Each VUV pulse followed a separate symmetric beam path, where the fifth harmonic was spectrally purified by focusing multilayer mirrors

( $HR\ 160\ nm$ ,  $f = 150\ mm$ , *Layertec*, 2 deg angle of incidence). Both beams were then redirected by Al-coated plane mirrors, bringing the two focused beams in a counter-propagating geometry. A pulsed gas valve provided a gaseous target in the common focal region, where the target was excited and further ionized. The photoionization products were imaged with a time-of-flight ion microscope with spatial resolution of  $< 3\ \mu m$  onto a position-sensitive detector, similar to the one described in [165]. Individual ion species were selectively imaged based on their time of flight by applying a high voltage pulse to the detector, acting as a temporal gate. The temporal delay between the counterpropagating pulses was mapped onto a spatial coordinate in the ion image (see Figure 3.2), thus enabling single-shot autocorrelation and pump-probe measurements. Reference measurements with a fringe-resolved interferometric autocorrelation technique [166] were performed using the exact experimental conditions to precisely calibrate the delay-time axis. These measurements resulted in a conversion factor of  $(1.3 \pm 0.1)$  fs/pixel of the CCD camera used to image the detector. Furthermore, the pump-probe signal as well as the spatial ion signal of each individual beam path can be observed with the detector in real time, which allows the experimentalist to precisely optimize the spatial overlap between both beam paths and measurement conditions.

Non-resonant two photon ionization of Kr was used for single-shot autocorrelation measurements in order to experimentally determine the instrument response function.  $H_2O$  and  $D_2O$  were supplied from the heated vapor of pure liquids, while HDO was supplied from the vapor of a mixture of both. By applying a backing pressure of less than 200 mbar the formation of water dimers or clusters can be excluded, verified by ion time-of-flight spectrometry.

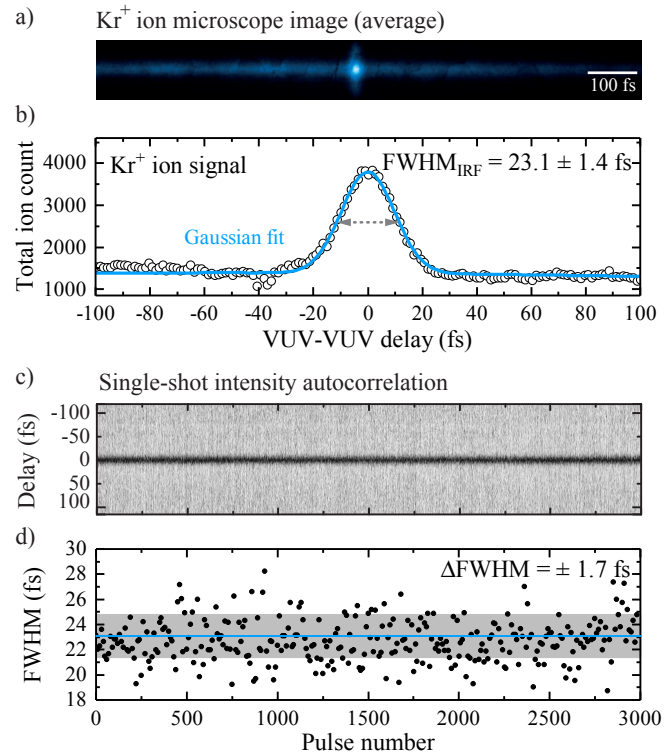


FIGURE 3.2: Ion microscope image and delay-dependent ion signal originating from the non-resonant two-photon ionization of Kr. The microscope image (a) shows the averaged spatially resolved Kr<sup>+</sup> ion yield for 3000 laser pulses. The averaged delay-dependent Kr<sup>+</sup> ion yield (b) corresponds to the VUV pulse intensity autocorrelation, which yields an instrument response function with a FWHM of  $(23.1 \pm 1.4)$  fs. From the single-shot intensity autocorrelation for each laser pulse (c), the root-mean-square uncertainty of its FWHM (d) can be deduced. © 2017, American Physical Society (APS)

## 3.2 Computational methods

The ultrafast dynamics of a water molecule and its deuterated derivatives, HDO and D<sub>2</sub>O, on their first electronically excited state was studied using a mixed quantum-classical approach in which the nuclear motions were treated classically by Newton’s equations of motion and the electrons were described quantum mechanically. Since the molecules are sufficiently cold in the experiment, the nuclear coordinates and momenta were sampled from the harmonic Wigner distribution [167] for the  $\tilde{X}^1A_1$  ground electronic state in which the zero-point vibrational energy is given to each normal mode. It is also assumed that all water molecules are initially in the rotational ground state. In this way initial conditions for 20 classical trajectories on the  $\tilde{A}^1B_1$  potential energy surface were obtained. The trajectories were then divided into two subsets of ten trajectories. Similar temporal evolutions of the two subsets confirmed sufficiently good statistics. For each trajectory 0.1 fs time steps were used for the numerical integration of Newton’s equations using the velocity Verlet algorithm [160]. On-the-fly

Electronic states	(a) Calc.	(b) Calc.	Exp.
$\tilde{A}^1B_1 \rightarrow \tilde{X}^2B_1$	5.000	4.249	5.168
$\tilde{A}^1B_1 \rightarrow \tilde{A}^2A_1$	7.302	6.829	7.192
$\tilde{A}^1B_1 \rightarrow \tilde{X}^2B_1$ (H + OH <sup>+</sup> )	12.247		13.017
$\tilde{A}^1B_1 \rightarrow \tilde{A}^2A_1$ (H <sup>+</sup> + OH)	13.420		13.598

TABLE 3.1: Vertical ionization energies of H<sub>2</sub>O at the experimental equilibrium position (top) and at the asymptotic region (bottom) calculated with (a) MR-CISD and (b) CASSCF with the OH bond length kept fixed at the equilibrium OH bond length of H<sub>2</sub>O. Experimental ionization energies for H<sub>2</sub>O, OH in their respective equilibrium geometries and the Hydrogen radical are taken from Refs. [168] and [169]. All values in electronvolts

ab-initio calculations of the electronic structure, including the gradients, were done with the complete active space self-consistent field method using six active electrons in four active orbitals, CASSCF(6,4), and the augmented double- $\zeta$  basis set, aug-cc-pVDZ [170, 171] utilizing the MOLCAS program package [172]. In order to improve

the numerical stability of the CASSCF calculations, the excited-state Hartree-Fock molecular orbitals of the positive ion were used as the initial molecular orbitals. The energies were reevaluated with single point calculations at the multireference single and doubles configuration-interaction level with eight correlated electrons and seven active orbitals, MR-CISD(8,7), and the aug-cc-pVDZ basis set. Both CASSCF and MR-CISD were employed because only CASSCF allows one to compute gradients analytically within MOLCAS, which is optimal for calculating chemical trajectories, whereas MR-CISD provides higher accuracy for ionization energies. Since the analytic gradients are calculated based on the CASSCF potential energy surface, the location of the atoms in space depends on the CASSCF force and therefore it is very crucial to have a correct shape of the CASSCF potential, especially at the FC region for the  $\tilde{A}^1B_1$  state, where the photodissociation reaction of water takes place. The MR-SDCI potential is used as a reference to check the validity of the CASSCF potential. The closer the CASSCF potential shape is to the MR-SDCI shape, the more reliable the CASSCF potential is [see Figure 3.3 (a)]. The accuracy of the shape of the MR-CISD potential itself is checked based on the expected vertical ionization values at both the FC region and at the asymptotic region, where one OH bond is broken (Table 3.1). As it can be seen from Table 3.1, at the FC region, the value of MR-CISD vertical ionization energies from the first electronic excited state of neutral water to the ground and first excited electronic states of water cation obtained from the MR-CISD potential are in a very good agreement with the corresponding experimental values. At the asymptotic region, MR-CISD vertical ionization energy for  $H^+ + OH$ , which is in principle the ionization energy of a hydrogen radical, is in excellent agreement with the experimental ionization energy [see Table 3.1 and Figure 3.3 (a)]. The ionization energy of  $H + OH^+$  depends on the OH bond length. The vertical ionization energy of OH radical, calculated with MR-CISD, deviates from the corresponding experimental value by 0.77 eV, which is

not a negligible deviation [see Table 3.1 and Figure 3.3 (a)]. This deviation, however, is not due to the inaccuracy of the MR-CISD potential energy surfaces, but it is stemming from the difference between the length of the OH bond in our calculations with that in the experimental conditions. For the scan underlying Table 3.1, the OH bond length was kept fixed at the equilibrium OH bond length of H<sub>2</sub>O; therefore its length in the asymptotic region differs from its optimal experimental value. The time windows in which the neutral molecule can be ionized to the electronic ground and first excited states of the cation with a single photon of 7.7 eV energy are obtained by averaging over 20 trajectories. Outside these time windows, the geometry is so far distorted in comparison to the equilibrium geometry that the cation could no longer be created with a single photon of 7.7-eV energy. Photoionization cross sections  $\sigma(\tilde{X}^2B_1)$  and  $\sigma(\tilde{A}^2A_1)$  were calculated for 7.7-eV photon energy as a function of the molecular geometry, applying the orthogonalized plane-wave approximation to the photoelectron wave function [173]. At each molecular geometry the MR-CISD(8,7) wave function for the  $\tilde{A}^1B_1$  state and the MR-CISD(7,7) wave functions for the  $\tilde{X}^2B_1$  and  $\tilde{A}^2A_1$  states were used for these calculations.

## 3.3 Results and discussion

### 3.3.1 Experimental data

The time constant for the VUV photodissociation of H<sub>2</sub>O is expected to be on the order of the duration of the pump and probe pulses according to previous studies [142]. To analyze reaction dynamics on this short time scale, a detailed knowledge of the instrument response function, which is given by the second order intensity autocorrelation (IAC), is necessary. To achieve this, the direct two-photon ionization of Kr has been measured directly before and after each pump-probe experiment.

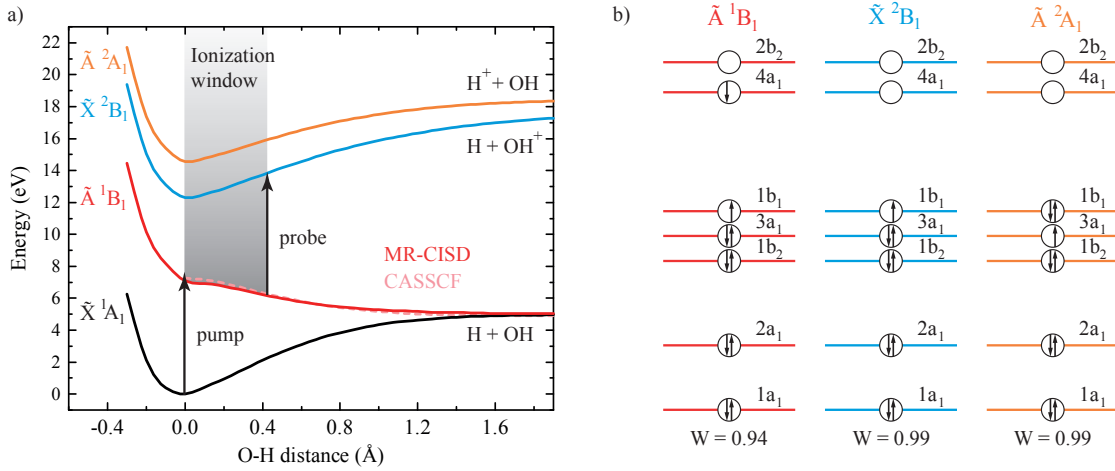


FIGURE 3.3: (a) Cuts through the potential energy surfaces for the ground and first excited electronic states of  $H_2O$  and  $H_2O^+$  calculated at the MR-CISD(8,7) and MR-CISD(7,7) level, respectively (solid lines) and for the  $\tilde{A}^1B_1$  state of  $H_2O$  calculated with CASSCF(6,4) (dashed line). The dissociation coordinate is obtained by changing the length of one of the O-H bonds ( $R_{OH}$ ) and maintaining the other O-H bond length and the angle HOH at the equilibrium values of 0.958 Å and 104.47°, respectively.  $R_{OH} = 0$  corresponds to the equilibrium bond length. (b) The dominant configurations for the  $\tilde{A}^1B_1$  state of a neutral water molecule, and  $\tilde{X}^2B_1$  and  $\tilde{A}^2A_1$  states of the cation and their corresponding CI coefficients at the equilibrium geometry (W) are obtained from the MR-CISD calculation. © 2017, American Physical Society (APS)

The resulting averaged ion image for  $Kr^+$  is shown in Figure 3.2 (a) for a data set of 3000 images, exhibiting a pronounced intensity increase, where both counterpropagating pulses overlap in space and time. In order to retrieve the intensity autocorrelation of the VUV pulse, the central position of individual ion hits in a single-shot image is extracted to increase the spatial resolution by eliminating the influence of the spot size of individual ion signals on the detector. Considering the delay time-to-space calibration, the delay-dependent ion yield is given by the profile of the spatial distribution of the ion image along the propagation axis. The resulting trace, Figure 3.2 (b), exhibits a peak-to-background ratio near the theoretically expected value of 3:1 for a 2<sup>nd</sup> order intensity autocorrelation, which is given by the Gaussian fit (blue). For the shown

measurement a FWHM of the intensity autocorrelation of  $(23.1 \pm 1.4)$  fs is retrieved, which corresponds to the instrument response function. Although a different temporal profile of the VUV pulse, e.g., a  $\text{sech}^2$  pulse, does result in a shorter retrieved pulse duration, the instrument response function is hardly changed and the possible impact on the pump-probe data sets is negligible.

To reliably distinguish the effect of systematic and statistical uncertainties on the measured pump-probe signal, not only the mean instrument response function is of interest. Utilizing the single-shot capabilities of the colliding-pulse geometry the effect of shot-to-shot instabilities, such as beam pointing or the temporal stability of the pulses, as well as the long-term stability of the pulse properties become accessible. In Figure 3.2 (c) the single-shot intensity autocorrelation is shown for each laser pulse. To increase the signal-to-noise ratio a 10 shot average is used to retrieve the temporal jitter of the instrument response function. Figure 3.2 (d) shows the mean FWHM of the instrument response function  $(23.1 \pm 1.4)$  fs as a blue line and its root mean square uncertainty as a gray box. Since the root mean square uncertainty of  $\pm 1.7$  fs is comparable to the uncertainty of the average measurement and no temporal drifts of the FWHM are visible, a high stability of the instrument response function over time is ensured.

In contrast to the non-resonant two-photon ionization of Kr, the delay-dependent ion yield for  $\text{H}_2\text{O}$  and its isotopologues is not only determined by the duration of the VUV pulses, but also by the internal dynamics of the molecule.

The experimentally obtained pump-probe signal for  $\text{H}_2\text{O}$  and its deuterated derivatives is determined by the convolution of the instrument response function and the internal dynamics of the respective molecule. To deconvolve these dynamics from the experimental data sets, where the instrument response function is on the same time scale as the expected ionization window, an appropriate fit function needs to be applied.

As has been shown in our trajectory simulations, the first trajectories start leaving the ionization window after more than 5 fs and up until this time the population in the ionization window stays constant. This behavior can be modeled as a rectangular function, where the duration of the ionization window is given by its half-width. The convolution of this function and the instrument response function is given by

$$I(\Delta t) = a \cdot \left[ \operatorname{erf} \left( \frac{\tau_{1/2} - \Delta t}{\sqrt{2}\sigma_p} \right) + \operatorname{erf} \left( \frac{\tau_{1/2} + \Delta t}{\sqrt{2}\sigma_p} \right) \right] \quad (3.1)$$

Here  $\Delta t$  is the delay between pump and probe pulse and  $\sigma_p$  is the standard deviation of the instrument response function ( $\sigma_p = \text{FWHM}/(2\sqrt{2\ln 2})$ ), while  $\tau_{1/2}$ , the half-width of the rectangular function, and the scaling factor  $a$  are the free fit parameters.

### 3.3.2 Computational data

Figure 3.3 (a) shows a one-dimensional cut through the potential energy surfaces, which are relevant for this pump-probe experiment. The potential energy surfaces have been calculated at the MR-CISD(8,7) and MR-CISD(7,7) levels for  $\text{H}_2\text{O}$  and  $\text{H}_2\text{O}^+$  respectively. The CASSCF calculation for the  $\tilde{A}^1B_1$  (light red) is shown in addition, emphasizing the excellent agreement between both calculation methods. In the excitation scheme employed in this pump-probe experiment, the first VUV photon (7.7 eV) excites the molecule from its electronic ground state (black) into the  $\tilde{A}^1B_1$  state (red). Since this state is unbound in the direction of the asymmetric stretch vibration, the molecule starts to dissociate. Not only is the bond distance of the dissociating bond shown in Figure 3.3 (a) changing during this dissociation reaction, but also the HOH angle and the second O-H bond distance are changing and have been taken into account in the calculation. Due to the increasing energy difference between the excited  $\tilde{A}^1B_1$  state and the electronic ground state of the  $\text{H}_2\text{O}^+$  ion (blue), as well as the first excited state (orange), the observation of the dissociation dynamics is

### 3.3. Results and discussion

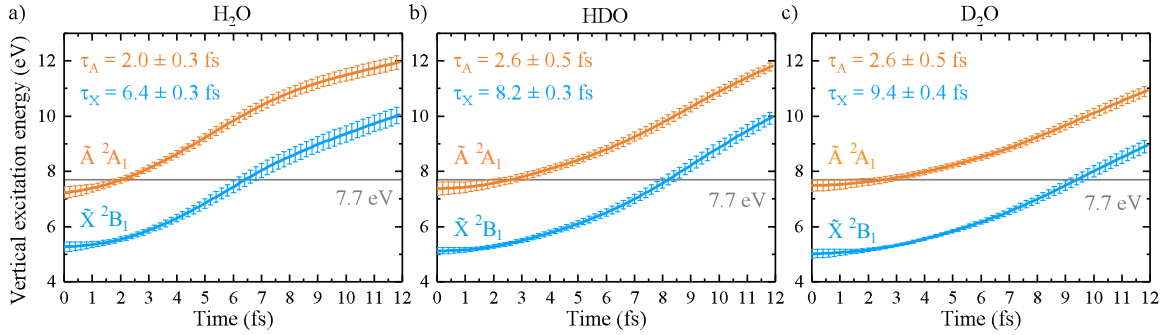


FIGURE 3.4: Calculated time evolution of the vertical excitation energy from the  $\tilde{A}^1B_1$  to the  $\tilde{X}^2B_1$  state (blue) and from the  $\tilde{A}^1B_1$  to the  $\tilde{A}^2A_1$  state (orange) during the dissociation for (a)  $\text{H}_2\text{O}$ , (b)  $\text{HDO}$ , and (c)  $\text{D}_2\text{O}$  and the corresponding time windows, in which ionization from  $\tilde{A}^1B_1$  to  $\tilde{X}^2B_1$  and  $\tilde{A}^2A_1$  with a single photon of 7.7 eV energy (gray line) is possible. The error bars represent the root-mean-square width of the energy distribution for a given time. © 2017, American Physical Society (APS)

confined to a limited time range. Thus, we precisely clock the time, when the molecular structure is distorted such that a single VUV probe photon cannot ionize the molecule anymore (depicted as the gray ionization window in Figure 3.3 (a)).

The duration of the ionization window can be extracted from the trajectory calculations for each isotopologue. Hence, the vertical excitation energies for the transition from the molecular  $\tilde{A}^1B_1$  state to the electronic ground state and to the first excited state of the ion are calculated for the evolving molecular coordinates after each time step. Figure 3.4 shows the time evolution of the vertical excitation energies for (a)  $\text{H}_2\text{O}$ , (b)  $\text{HDO}$  and (c)  $\text{D}_2\text{O}$ , as well as the photon energy of the probe pulse as a reference. As soon as the excitation energy for each transition exceeds the probe photon energy, the ionization window for the respective excitation scheme closes. The shortest window for ionization to the ground cationic state corresponds to  $\text{H}_2\text{O}$  and is 6.4 fs, increasing to 8.2 fs for  $\text{HDO}$ , due to the higher mass of the fragment.  $\text{D}_2\text{O}$  exhibits the longest time window of 9.4 fs.

The corresponding ionization window for a probe transition to the first electronically excited state of  $\text{H}_2\text{O}^+$  and its deuterated derivatives is much shorter than the time window for ionization to their ground electronic state. Depending on the ratio between their respective photoionization cross sections, both probe transitions may contribute to the experimentally observed ionization window. The longest ionization window is observed if the photoionization cross section  $\sigma$  for the  $\tilde{X}^2B_1$  channel is much larger than  $\sigma(\tilde{A}^2A_1)$ . On the other hand, the apparent ionization window gets shorter as the ratio  $\sigma(\tilde{A}^2A_1)/\sigma(\tilde{X}^2B_1)$  increases. It should be noted that, even at distances where ionization is still possible,  $\sigma$  is not necessarily constant.

According to our calculations,  $\sigma(\tilde{A}^2A_1)$  is negligible in comparison to  $\sigma(\tilde{X}^2B_1)$  at all molecular geometries where ionization to both states is possible. This can even be demonstrated at the independent-particle level, which implies that a single photon can remove an electron from a configuration only without influencing the rest of the configuration. Figure 3.3 (b) shows the dominant configurations for the  $\tilde{A}^1B_1$  state of  $\text{H}_2\text{O}$  and the  $\tilde{X}^2B_1$  and the  $\tilde{A}^2A_1$  states of  $\text{H}_2\text{O}^+$  and their corresponding MR-CISD coefficients at the equilibrium geometry. It can be seen from Figure 3.3 (b) that a transition from the dominant configuration of  $\tilde{A}^1B_1$  to the dominant configuration of  $\tilde{X}^2B_1$  is possible at the independent-particle level, because only one electron is removed by the single-photon probe step. In contrast, the transition to the dominant configuration of  $\tilde{A}^2A_1$  is forbidden, since an additional electron is excited to another orbital, requiring a two photon absorption. Other configurations of  $\tilde{A}^1B_1$  provide a negligible contribution to the photoionization probability to the state  $\tilde{A}^2A_1$ . The configurations shown in Figure 3.3 (b) are dominant for the corresponding states at all geometries where photoionization is possible. Thus, since  $\sigma(\tilde{A}^2A_1)$  is negligible in comparison to  $\sigma(\tilde{X}^2B_1)$ , the photoionization time windows are determined exclusively by the vertical excitation energy from the  $\tilde{A}^1B_1$  to the  $\tilde{X}^2B_1$  potential energy surface

in the employed single-photon probe scheme. For a given pump photon energy the time evolution shown in Figure 3.3 (a) is universal and the  $\tilde{A}^2A_1$  state of the ion will be relevant for a multi-photon probe scheme.

For all isotopologues an excellent agreement between the duration of the ionization window deconvolved from the delay-dependent ion yield and the duration of the ground state ionization window derived from the mixed quantum-classical calculation was achieved, showing that ionization to the ionic ground state is the only significant probe transition contributing to the delay-dependent parent ion yield. An important result of this joint experimental and theoretical study is that the interpretation of pump-probe data even for a ‘simple’ dissociation reaction in the sub 10 fs regime is not trivial. Even when the instrument response function can be determined precisely, the choice of appropriate model function for the delay-dependence of the observable is necessary – in this case the time the molecule needs to exit the ionization window. Assuming an exponential decay rate for the observable, as it is valid for most reactions studied by femtochemistry on the few hundred femtosecond or picosecond time scale, leads in this case to an underestimation of the duration of the ionization window, while the deconvolved duration of a rectangular window coincides well with our mixed quantum-classical trajectory calculation.

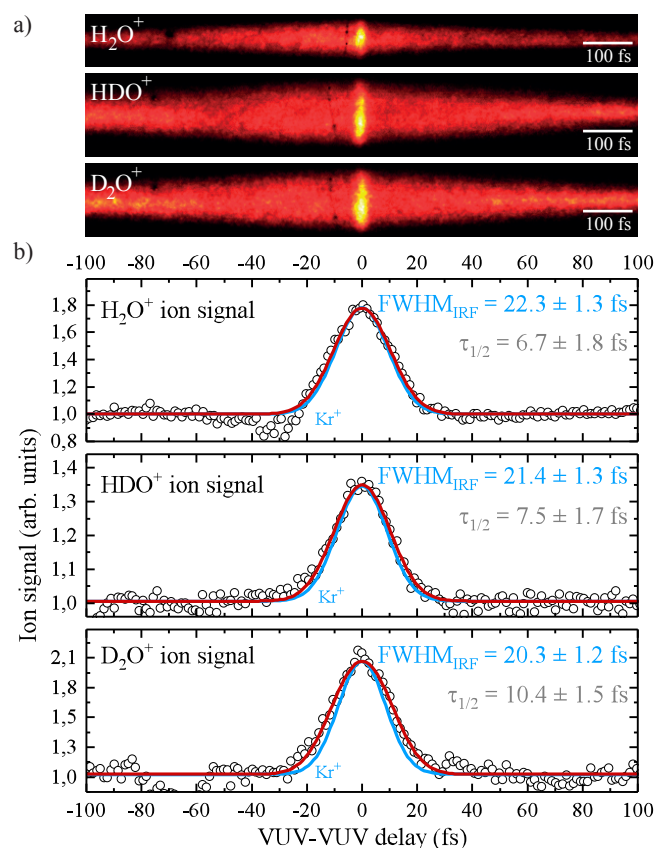


FIGURE 3.5: Ion microscope images and delay-dependent ion signals for  $\text{H}_2\text{O}$ ,  $\text{HDO}$  and  $\text{D}_2\text{O}$ . The microscope image (a) shows the averaged spatially resolved ion yield of the different isotopologues for 3000 laser pulses. The delay-dependent ion signal (b) of each isotopologue is shown in comparison to the instrument response function (blue) recorded in the corresponding measurement series and fitted with a Gaussian function (red). Depending on the degree of deuterization an increased FWHM is observed with respect to the instrument response function, indicating a kinetic isotope effect on the excited state dynamics of the molecule.

© 2017, American Physical Society (APS)

## Chapter 4

# XUV photochemistry of the Benzene Radical Cation

Reprinted with permission from *J. Phys. Chem. A* 2018, 122, 4, 1004-1010,  
Copyright 2018 American Chemical Society.

S. Bazzi, R. Welsch, O. Vendrell, and R. Santra, “Challenges in XUV photochemistry simulations: A Case study on ultrafast fragmentation dynamics of the benzene radical cation,”

<https://pubs.acs.org/doi/abs/10.1021/acs.jpca.7b11543>

In this chapter, I address two fundamental aspects of the XUV photochemistry of the benzene radical cation: (I) the time-resolved state-specific fragmentation dynamics, and (II) the time resolved relaxation of the electronic excited states through internal conversion. Understanding the extreme ultraviolet (XUV) induced dynamics and the subsequent fragmentation of molecular systems is important as it can provide answers to a broad range of fundamental questions such as the photochemical fate of biologically relevant molecules, which is related to the origin of life on earth [174], the evolution and complexity of the interstellar medium [175], and the photochemistry of atmospheric molecules. Of particular interest is the photochemical behavior of XUV irradiated polycyclic aromatic hydrocarbons (PAHs) due to their fundamental role in

understanding the chemistry in the interstellar medium. Since the proposal that PAHs are the carriers of certain infrared emission bands observed in outer space [176], these molecules have been the subject of considerable experimental [177–180] and theoretical work [181–183]. It is, however, challenging to obtain a complete picture of the dynamics and dissociation patterns of such large systems after XUV irradiation (10–124 eV), as one has to deal with several nuclear degrees of freedom, as well as a broad range of excited states and fragmentation channels. There is an urgency for further development of theoretical methods that can describe the XUV photochemistry of medium-sized to large systems.

The goal of this study is to evaluate a relatively low-cost theoretical method for investigating the XUV-induced nonadiabatic dynamics of medium-sized to large systems. The theory we used in this chapter is a combination of Koopmans’ theorem and Tully’s fewest switches surface hopping algorithm implemented in our in-house program package called Chemical Dynamics Tool Kit (CDTK). CDTK is capable of performing nonadiabatic mixed quantum-classical dynamics.

In this chapter, I will show how we successfully described the internal conversion dynamics that occurs in a few tens of femtoseconds. The Koopmans’ theorem based approach, however, underestimates the fragmentation probability due to overestimation of the CH dissociation barrier. This work was initiated by our colleague Melanie Schnell and is relevant for experiments at FLASH.

## 4.1 Computational methods

Ab initio classical trajectory calculations and the fewest switches surface hopping (FSSH) scheme [147] are employed to describe the nonadiabatic ultrafast dynamics of a singly charged benzene molecule ionized into any of 15 valence ionization channels characterized by the removal of an electron from each of the 15 occupied valence

molecular orbitals of benzene in the ground state. FSSH is conceptually and practically a simple method and at the same time it has a good accuracy and high computational efficiency. Therefore, it has so far been one of the most utilized methods to describe nonadiabatic dynamics. In the FSSH scheme, classical trajectories are propagated on a single adiabatic potential energy surface and statistically switched to another adiabatic potential energy surface according to a hopping probability. The methodology for the FSSH approach can be found in chapter 2.

Electronic structure data, energies, energy gradients, and nonadiabatic couplings, are determined on the fly on the basis of Koopmans' theorem and using the 6-31g\* basis set utilizing the MOLCAS program package [172]. The fifteen one-hole electronic states are created by removing a valence electron from each of the fifteen Hartree-Fock (HF) valence molecular orbitals of neutral benzene. The energy of the  $i$ -th state is obtained as: [82, 184]

$$V_{i,HF-K} = V_{HF} - \epsilon_i, \quad (4.1)$$

where  $V_{HF}$  is the ground state Hartree-Fock energy of neutral benzene and  $\epsilon_i$  is the energy of the  $i$ -th occupied orbital with  $i=0$  being the highest occupied orbital. The multiconfigurational capabilities of MOLCAS [172] are used to generate the corresponding electronic wave functions  $|\Psi_i\rangle$  with the orbitals from the HF calculation. Gradients and nonadiabatic couplings are then obtained from these configurations employing the RASSI module [82].

The initial nuclear coordinates and momenta are sampled from the vibrational ground state distribution of neutral benzene. This corresponds to the limit of  $T=0K$ . Microcanonical normal mode sampling [157] is employed to assign to each normal mode its zero-point energy. Coordinates  $q_i$  and conjugated momenta  $p_i$  for the  $i$ -th normal

mode are chosen as:

$$q_i = \sqrt{\frac{2E_i}{f_i}} \cos(2\pi\zeta), \quad (4.2)$$

$$p_i = \sqrt{2m_i E_i} \sin(2\pi\zeta), \quad (4.3)$$

with  $\zeta$  being a uniformly distributed random number,  $0 < \zeta < 1$ ,  $E_i$  the zero-point energy,  $f_i$  the force constant, and  $m_i$  the mass of the  $i$ -th normal mode. Normal mode coordinates and momenta are then transformed to Cartesian coordinates for the propagation. The sampled geometries are lifted vertically to the different electronic states of the cation. The nuclear motion is simulated for an ensemble of fifty independent trajectories for each initial electronic state. Newton's equations of motion are integrated using the velocity Verlet algorithm [160] with a time step of 0.5 fs and a total propagation time of 300 fs. Each time step takes on average 270 seconds on a single core of an Intel Xenon X5660 2.80GHz CPU. Therefore, about 45 hours of CPU time are needed for the propagation of each trajectory. We note that some of the dissociative trajectories are not propagated for the full 300 fs due to SCF convergence problems.

## 4.2 Potential energy surfaces

The study reported here involves fifteen coupled potential energy surfaces of the valence shell singly ionized benzene. The fifteen surfaces are grouped into ten electronic states according to the degeneracy of the orbitals at the Franck-Condon region. Table 4.1 lists the symmetry assignments of the electronic states and the corresponding orbital energies at the equilibrium geometry of the neutral benzene. The orbital energies

obtained from our Koopmans' theorem based approach are in reasonable agreement with binding energies obtained by the third-order algebraic-diagrammatic construction [ADC(3)] scheme [185]. While some quantitative differences of the absolute energies can be found, the relative energies, which are more important for the dynamical study, are in good agreement. The relative energy difference from one state to the next one in the manifold of the  $\tilde{B}^2E_{2g}$  to the  $\tilde{G}^3A_{1g}$  states is at most 0.24 eV, but often lower. As expected, bigger differences are found for the higher-lying states and for the difference between the ground and first excited state. The latter, however, should not be problematic as we still find ultrafast electronic decay to the ground state.

## 4.3 State-specific fragmentation dynamics

Figure 4.1 summarizes the fragmentation dynamics along with the state population dynamics. Fragments appear after 100 fs which is longer than the typical internal conversion time. This shows that the fragmentation does not occur in the initially excited electronic state. Previous studies of benzene [188–190] suggest that the dissociation occurs from the ground electronic state after a fast non-radiative relaxation even if higher electronic states are initially populated. A similar behavior can be found in our simulations. The only exception is found for a single trajectory on the highest valence shell excited state ( $\tilde{J}^2A_{1g}$ ) where the molecule breaks apart after relaxation to the second excited state,  $\tilde{C}^2A_{2u}$  (Figure 4.1).

For lower electronically excited states, with orbital energies up to -22.313 eV (see Table 4.1), only H and CH elimination are observed (panels a-d of Figure 4.1). The channel with two large fragments,  $C_4H_4^+ + C_2H_2$ , only appears for highly excited states of the benzene radical cation (states  $\tilde{I}^2E_{1u}$  and  $\tilde{J}^2A_{1g}$ ) with orbital energies of -27.519 and -31.239, respectively (see Figure 4.1 e and f). This is in agreement with an experimental study [191] where the authors show that the contribution due to the

Symmetry symbol	Orbital energy (eV)	Dissociation probability (%)	Half life (fs) present	Half life (fs) Ref. [186] <sup>(a)</sup>
$\tilde{X}^2E_{1g}$	-8.996	-	-	-
$\tilde{B}^2E_{2g}$	-13.320	3.0	120	100 >200
$\tilde{C}^2A_{2u}$	-13.551	0.0	15	15 15
$\tilde{D}^2E_{1u}$	-15.897	2.0	30	>200 95
$\tilde{E}^2B_{2u}$	-16.708	0.0	15	15 15
$\tilde{F}^2B_{1u}$	-17.410	0.0	10	-
$\tilde{G}^3A_{1g}$	-19.244	1.5	20	-
$\tilde{H}^2E_{2g}$	-22.313	4.0	>300	-
$\tilde{I}^2E_{1u}$	-27.519	2.0	>300	-
$\tilde{J}^2A_{1g}$	-31.239	2.0	>300	-

a: The first and second rows refer to the cases where an initial electronic state is coupled to two and three neighboring states, respectively. Taken from Ref. [187].

TABLE 4.1: The symmetry assignment of the excited electronic states of  $C_6H_6^+$  and the corresponding orbital energies calculated at HF/6-31g\* level at the equilibrium geometry of the neutral benzene. The dissociation probability for an initial excitation to each electronic state is also given. The Half life of each of the initially excited states is given and compared to Ref. [186].

$C_4H_4^+$  rapidly increases at higher photon energies.

Another interesting observation is the  $C_6H_4^+$  fragment ion production.  $C_6H_4^+$  is produced either through a concerted dissociation mechanism or through a stepwise process via  $C_6H_5^+$ . As shown in Table 4.1, the dissociation probability upon valence shell ionization of benzene is a maximum of 4 % after 300 fs. This is in contrast with an experimental study on the photoionization and photodissociation of benzene, which shows more than 50 % dissociation at a UV energy of 21.21 eV [192]. Experiments in

the higher excitation energies show that above 20 eV, more than 50 % of the benzene cation dissociates [191, 193]. The discrepancy between the simulation and the experiment can be rationalized by comparing the calculated CH dissociation barrier for the ground state benzene cation with the value obtained at higher level of theory and through experiment (see Figure 4.2). The CH dissociation energy calculated at the same level of theory as employed in our classical trajectory calculations (HF/6-31g\*) is 7.3 eV. It considerably overestimates the value obtained from CASPT2/6-31g\* (see Figure 4.2). The CASPT2 calculations use an active space with 11 active electrons distributed in 8 molecular orbitals. An RRKM fit of experimental data suggests an even lower dissociation energy of 3.66 eV [189]. Thus, the benzene radical cation may remain artificially bound in our simulations. Nonetheless, we note that the CH energy profile calculated at the HF/6-31g\* level matches the corresponding surface calculated at the CASPT2/6-31g\* level around the equilibrium geometry. Moreover, the limited propagation time might also contribute to the low fragmentation yield observed in this study. For trajectories with enough initial energy to overcome the artificially high barriers the most frequent fragments upon dissociation of the benzene cation are:  $C_6H_5^+ + H$ ,  $C_6H_4^+ + 2H$ , and  $C_4H_4^+ + C_2H_2$ , which appear after 100 fs. These ionic fragments are also among the most abundant fragment ions observed experimentally upon valence shell ionization of the benzene molecule [191, 192].

## 4.4 Internal conversion dynamics

As discussed in the previous section, the potential energy surface of the cationic ground state in the Franck-Condon region is well described by the Koopmans' theorem based approach. Based on this and earlier studies [82], we expect the short-time nonadiabatic dynamics to be reasonably well described by the simulations presented in this study. Figures 4.3 and 4.4 show the population dynamics for different initial excitations.

Figure 4.3 (a) presents the case of an initial excitation to the  $\tilde{B}^2E_{2g}$  state. For this case, the  $\tilde{B}^2E_{2g}$  population gradually decreases to reach 25 % at 270 fs when the  $\tilde{X}^2E_{1g}$  state reaches its maximum at around 73 % (Figure 4.3 a). The coupling to the  $\tilde{C}^2A_{2u}$  state is very weak and the corresponding population remains almost unchanged during the dynamics. The short time dynamics are in good agreement with previous theoretical work based on a reduced-dimensional quantum dynamics description using a vibronic coupling model Hamiltonian [186, 194, 195]. However, for longer times a faster decay to the ground state is found compared to previous work. The difference might be attributed to the reduced dimensionality and the harmonic expansion in the previous work or to the surface hopping approximation in our simulations. In Table 4.1, the half life of the different states is given, i.e., the time it takes for the population of an initially excited state to decrease to 50%. The half life computed for the  $\tilde{B}^2E_{2g}$  state agrees very well with previous work [186].

Figure 4.3 (b) shows the case of an initial excitation to the  $\tilde{C}^2A_{2u}$  state. The half life of the  $\tilde{C}^2A_{2u}$  state is 15 fs and in perfect agreement with previous work (see Table 4.1). The  $\tilde{B}^2E_{2g}$  state population steeply increases to its maximum of 75% within 60 fs and then gradually decays to zero at 250 fs, when the  $\tilde{X}^2E_{1g}$  state population reaches its maximum (93 %). For the first 100 fs, the results of our study are in good agreement with previous calculations [186]. Again at longer times, a slightly faster decay to the ground state is found in our simulations compared to the previous study [186]. Experimentally, no fluorescence from the  $\tilde{C}^2A_{2u}$  state is found although the transition from the  $\tilde{C}^2A_{2u}$  to the  $\tilde{X}^2E_{1g}$  is dipole-allowed, [196] which supports a fast radiationless transition from the  $\tilde{C}^2A_{2u}$  state to the ground state [196]. In an experiment based on photo-dissociation kinetics and charge exchange ionization mass spectroscopy [197] a long lived electronic excited state was observed in the energy range of the  $\tilde{B}^2E_{2g}$  and  $\tilde{C}^2A_{2u}$  states, which was eventually assigned to the  $\tilde{B}^2E_{2g}$

state. However, the authors were not absolutely certain about the assignment because of a controversy regarding the lifetime of the  $\tilde{B}^2E_{2g}$  state [190, 196]. According to our results the  $\tilde{B}^2E_{2g}$  state is somewhat longer-lived than the  $\tilde{C}^2A_{2u}$  state.

Starting the initial wave packet from the  $\tilde{D}^2E_{1u}$  state [Figure 4.3 (c)], a very fast decay of the  $\tilde{D}^2E_{1u}$  state population occurs. The  $\tilde{D}^2E_{1u}$  state population dynamics considerably differ from the previous theoretical studies, where the population gradually decays and reaches about 40 % at 200 fs and the half life is considerably longer than in the present work [186, 194]. This discrepancy already at short times can be due to the reduced dimensional description employed in previous works that may not capture the dynamics of the benzene cation in the  $\tilde{D}^2E_{1u}$  state adequately or it can be due to shifts in the positions of the conical intersections in our calculations. Figure 4.4 illustrates the state population dynamics for an initial excitation to the states  $\tilde{E}^2B_{2u}$ ,  $\tilde{F}^2B_{1u}$ ,  $\tilde{G}^3A_{1g}$ ,  $\tilde{I}^2E_{1u}$ , and  $\tilde{J}^2A_{1g}$ . The population dynamics following initial excitation to the  $\tilde{E}^2B_{2u}$ ,  $\tilde{F}^2B_{1u}$ , and  $\tilde{G}^3A_{1g}$  states show very similar behavior as for the  $\tilde{C}^2A_{2u}$  and  $\tilde{D}^2E_{1u}$  states (compare panels b and c of Figure 4.3 with panels a, b, and c of Figure 4.4). In all of these cases, an initial excitation to the states  $\tilde{E}^2B_{2u}$ ,  $\tilde{F}^2B_{1u}$ , and  $\tilde{G}^3A_{1g}$  is accompanied by a very fast decay to the ground state. Initial excitations to the  $\tilde{I}^2E_{1u}$  and  $\tilde{J}^2A_{1g}$  states, however, show a slow decay similar to what has been discussed for the  $\tilde{H}^2E_{2g}$  state (compare panel d of Figure 4.3 with panels d, e of Figure 4.4). The slow decay for these highest lying valence states was similarly observed in a theoretical study of naphthalene [61].

This longer lifetime in our simulations can be explained based on the large energy gap of the higher-lying electronic states to any other state for the geometries sampled during the dynamics. Table 4.2 shows the minimum and maximum difference, averaged over 50 trajectories, between the potential energies of the initially excited electronic state with the lower lying electronic states along the dynamics,  $\Delta E_{min}$  and  $\Delta E_{max}$ ,

respectively. As can be seen from Table 4.2, the  $\Delta E_{min}$  between two immediate potentials ( $\Delta E_{min_{i, i-1}}$ ) correlates very well with the life time of the electronically excited states, where  $i$  refers to the state number. In the case of the initially degenerate states, we compare the two closest potentials corresponding to different states. The fastest electronic population decay is observed for the states where the  $\Delta E_{min_{i, i-1}}$  reaches a value less than 0.7 eV along the dynamics (states  $\tilde{C}^2A_{2u}-\tilde{G}^3A_{1g}$ ).  $\Delta E_{min_{i, i-1}}$  for the  $\tilde{B}^2E_{2g}$  state is 1.5 eV and it shows a relatively slower decay compared to the states  $\tilde{C}^2A_{2u}-\tilde{G}^3A_{1g}$ . In particular, for states  $\tilde{H}^2E_{2g}$ ,  $\tilde{I}^2E_{1u}$ , and  $\tilde{J}^2A_{1g}$  we observe large gaps to all other states, which explains well their high stability in our simulations. The average gap of the higher-lying states to the next lower state is typically about 3 eV and never decreases below 0.5 eV (Table 4.2). This large energy gap might hinder the high internal energy of the cation to convert into vibrational energy in lower-lying states. Therefore, the highly electronically excited cation is surprisingly less likely to undergo dissociation. It should be noted that including shake-up states in the electronic structure calculations could lead to a faster non-radiative decay of the high-lying states. The number of shake-up states increases above 20 eV [185] and thus they could bridge the large energy gaps seen in our simulations. However, we would expect the non-radiative decay from the inner valence excited states to the outer valence excited states to be slower than the decay of the outer valence states, even if shake-up states are included. No study of conical intersections at these energies has been performed. The effect of shake-up states on XUV induced photodissociation of benzene requires further investigation and is beyond the scope of this work.

State	0(X)	1(X)	2(B)	3(B)	4(C)	5(D)	6(D)	7(E)	8(F)	9(G)	10(H)	11(H)	12(I)	13(I)
<b>1(X)</b>	0.1-1.2													
<b>2(B)</b>	2.2-3.6	<b>1.5-3.1</b>												
<b>3(B)</b>	4.1-4.6	3.2-4.0	0.5-1.7											
<b>4(C)</b>	4.6-5.3	3.9-4.6	0.9-2.5	<b>0.2-0.9</b>										
<b>5(D)</b>	5.3-6.6	4.6-6.1	2.1-3.6	1.0-2.0	<b>0.6-1.5</b>									
<b>6(D)</b>	6.2-7.6	5.7-6.4	3.0-4.4	2.2-3.0	1.5-2.3	0.3-1.4								
<b>7(E)</b>	7.1-8.3	6.6-7.4	3.8-5.4	3.0-3.9	2.3-3.1	0.9-2.0	<b>0.5-1.1</b>							
<b>8(F)</b>	7.9-9.5	7.6-8.4	4.5-6.6	3.8-5.1	3.2-4.4	1.8-3.2	1.3-2.1	<b>0.4-1.3</b>						
<b>9(G)</b>	8.9-10.7	8.6-9.9	5.4-7.2	5.0-6.2	4.5-5.4	3.1-4.3	2.5-3.2	1.7-2.5	<b>0.5-1.7</b>					
<b>10(H)</b>	12.1-13.2	11.4-12.8	8.8-9.6	8.0-8.7	7.3-8.1	5.9-6.4	5.4-6.1	4.7-5.3	3.4-4.6	<b>2.5-3.3</b>				
<b>11(H)</b>	13.2-14.5	12.6-13.4	9.7-10.7	8.9-9.9	8.4-9.2	6.7-7.9	6.6-7.1	5.7-6.4	4.6-5.4	3.4-4.2	0.3-1.6			
<b>12(I)</b>	17.5-18.5	16.3-18.0	13.4-14.9	13.0-14.0	12.2-13.4	11.1-12.1	11.3-11.4	9.6-10.6	7.9-10.0	7.3-8.5	4.3-5.3	<b>3.5-4.8</b>		
<b>13(I)</b>	18.4-19.5	17.7-18.5	14.6-15.7	14.14.9	13.3-14.3	11.8-13.1	11.3-12.2	10.8-11.4	9.1-10.8	8.4-9.3	6.4-5.1	4.7-5.5	0.2-1.6	
<b>14(J)</b>	20.2-22.6	19.8-22.1	16.8-19.0	16.0-18.0	15.3-17.0	14.0-16.0	13.4-15.5	12.9-14.7	11.0-14.0	10.1-12.3	7.2-9.4	6.7-8.8	2.4-4.7	<b>2.3-3.6</b>

TABLE 4.2: Average of the minimum and maximum difference between the potential energies along the 50 trajectories started on the given potential energy surfaces. All quantities are given in eV. Table is taken from the supplementary information of Ref. [187].

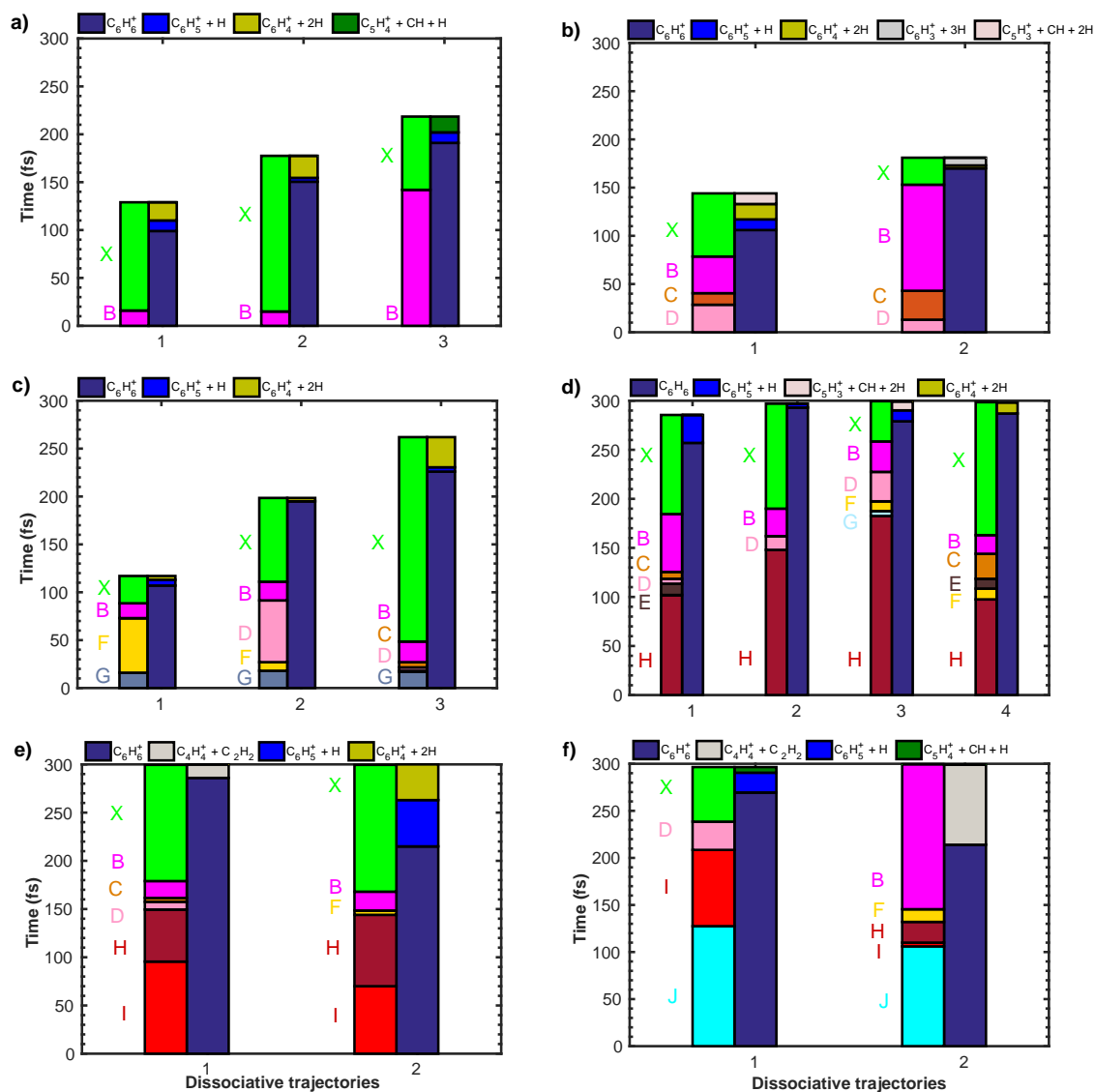


FIGURE 4.1: Fragmentation dynamics along with the internal conversion dynamics for an initial excitation to the states a)  $\tilde{B}^2E_{2g}$ , b)  $\tilde{D}^2E_{1u}$ , c)  $\tilde{G}^3A_{1g}$  d)  $\tilde{H}^2E_{2g}$ , e)  $\tilde{I}^2E_{1u}$ , and f)  $\tilde{J}^2A_{1g}$ . The left bar displays the current electronic state of the trajectory and the right bar indicates the fragments. Taken from the supplementary information of Ref. [187].

© 2018, American Chemical Society (ACS)

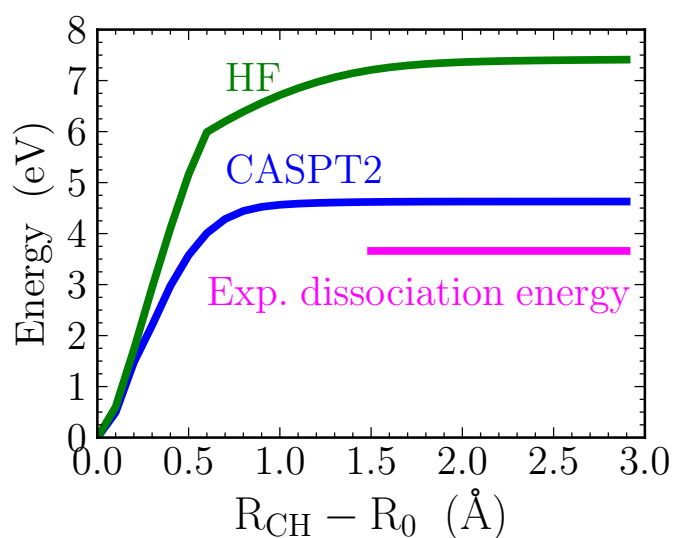


FIGURE 4.2: Cuts through the potential energy surface for the  $\tilde{X}^2E_{1g}$  state of  $\text{C}_6\text{H}_6^+$  calculated with HF/6-31g\* (green), and CASPT2(12,8)/6-31g\* (blue). The dissociation coordinate is obtained by changing the length of one of the CH bonds ( $R_{\text{CH}}$ ) and maintaining the other bond lengths and the angles at the equilibrium values.  $R_0$  corresponds to the equilibrium bond length. Figure is taken from Ref. [187]. © 2018, American Chemical Society (ACS)

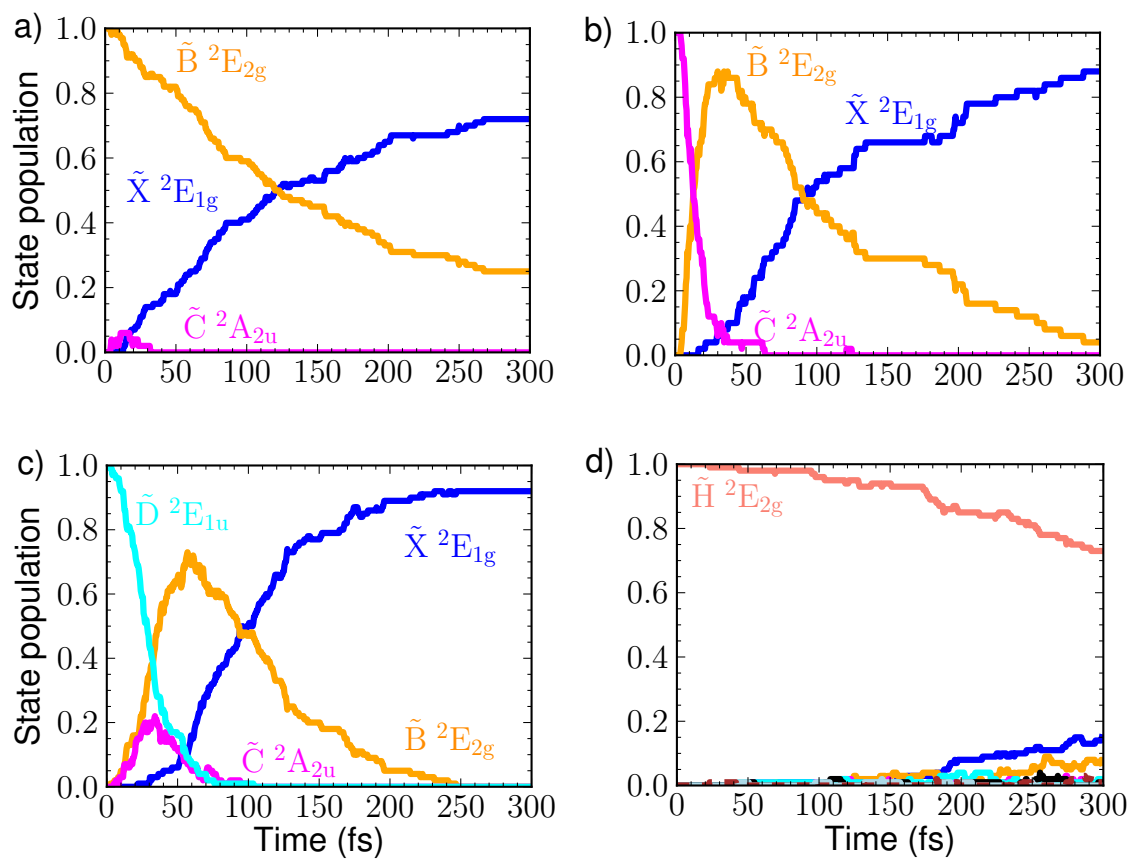


FIGURE 4.3: Internal conversion dynamics for an initial excitation to the states (a)  $\tilde{B}^2E_{2g}$ , (b)  $\tilde{C}^2A_{2u}$ , (c)  $\tilde{D}^2E_{1u}$ , and (d)  $\tilde{H}^2E_{2g}$ . Figure is taken from Ref. [187]. © 2018, American Chemical Society (ACS)

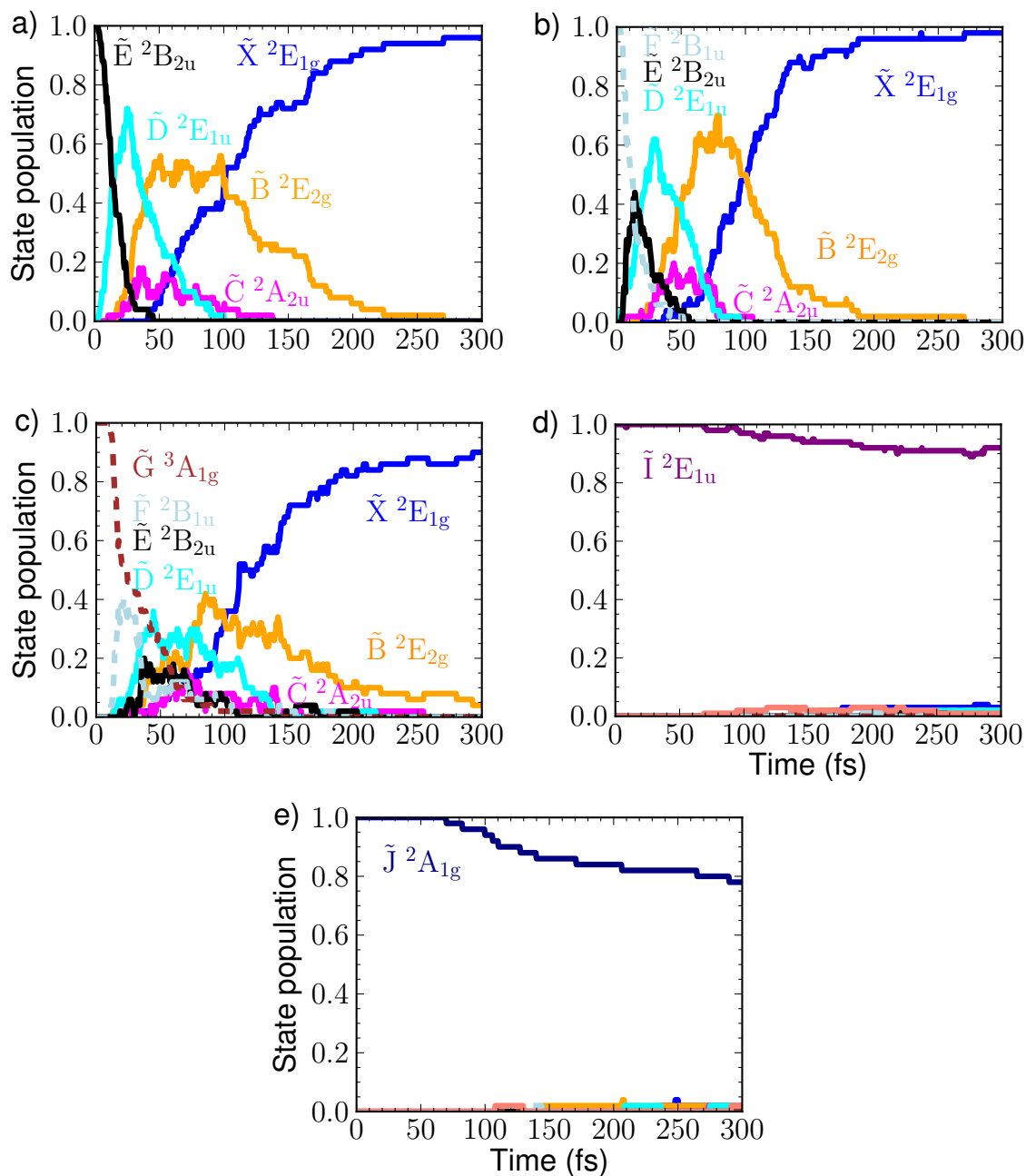


FIGURE 4.4: Internal conversion dynamics for an initial excitation on the states (a)  $\tilde{E}^2B_{2u}$ , (b)  $\tilde{F}^2B_{1u}$ , (c)  $\tilde{G}^3A_{1g}$ , (d)  $\tilde{I}^2E_{1u}$ , and (e)  $\tilde{J}^2A_{1g}$ . Figure is taken from the supplementary information of Ref. [187]. © 2018, American Chemical Society (ACS)

## Chapter 5

# Ultrafast charge transfer and structural dynamics following outer valence ionization of a halogen-bonded dimer

Reprinted with permission from *J. Phys. Chem. A* 2019, 123, 34, 7351-7360, Copyright 2019 American Chemical Society.

S. Bazzi and R. Santra, "Ultrafast Charge Transfer and Structural Dynamics Following Outer-Valence Ionization of a Halogen-Bonded Dimer.

<https://pubs.acs.org/doi/10.1021/acs.jpca.9b00646>

In this chapter, I use the same theory as in chapter 4 to describe the vertical ionization-induced charge transfer and structural dynamics in  $\text{CH}_2\text{O} \cdots \text{ClF}$  halogen-bonded dimer. Halogen bonds are noncovalent interactions comparable in strength (up to 2.0 eV, 47.8 kcal/mol) to hydrogen bonds [198]. Although hydrogen bonding in the electronic excited state has been the subject of numerous studies [199, 200], excited-state halogen bonding is largely unexplored. Despite its potential importance, electronically nonadiabatic or non-Born–Oppenheimer halogen bonding has never been studied before.

As already discussed in chapter 1, describing the photochemistry of halogen-bonded systems in their excited electronic states is a challenging task because it requires considering the coupling between nuclei and electronic motions in a non-Born–Oppenheimer regime [187].

In the following, we investigate the temporal evolution of the structure and the charge of the  $\text{CH}_2\text{O}\cdots\text{ClF}$  dimer after removing an electron from each of three outer-valence molecular orbitals. We show that the distance between the oxygen and chlorine atoms is directly connected to the magnitude of the charge on the O and Cl atoms. Taking the distance between the two molecules involved in halogen-bond interaction as a measure of the halogen bond strength, we show the significance of electrostatic interaction and the contribution of the molecular orbitals to the halogen-bond strength.

## 5.1 Computational methods

To describe the nonadiabatic ultrafast dynamics of the halogen-bonded dimer following outer-valence ionization we follow three main steps: (1) Optimize the  $\text{CH}_2\text{O}\cdots\text{ClF}$  geometry. (2) Sample the initial nuclear coordinates and momenta. (3) Start trajectories on the ground-state and excited-state potentials of the dimer cation using the Tully’s fewest switches surface hopping (FSSH) approach. [147]

(1) Optimization. The minimum-energy geometry of the  $\text{CH}_2\text{O}\cdots\text{ClF}$  dimer is computed using the same level of theory as employed in our trajectory calculations (HF/ANO-L-VTZP) utilizing the MOLCAS 8.2 package [201]. The main structural parameters of the optimized dimer are shown in Figure 5.1 and compared with the gas-phase experimental values [202]. The level of theory used here is not the best choice for optimization of halogen-bonded systems because halogen bond interactions are weak interactions with soft interaction potentials; thus only methods that take into account

electron correlation are considered to be reliable for describing this family of interactions. [198] However, we chose this method for optimization to be consistent with the adopted Koopmans' theorem-based trajectory calculations. The Koopmans' theorem-based approach is suitable for describing the short-term dynamics and nonadiabatic relaxation processes [187].

(2) Sampling the phase space. Initial nuclear positions and velocities were sampled from the Wigner quantum harmonic-oscillator distribution for the ground state [157]. The Wigner distribution [203] for the vibrational ground state is given as

$$W^{(n=0)}(\mathbf{R}, \mathbf{P}) = e^{-(\mathbf{P}^2 + \mathbf{R}^2)}, \quad (5.1)$$

where  $(R, P)$  is a point in the phase space of dimensionless normal coordinates and canonically conjugate momenta [203]. The Wigner distribution is sampled employing the von Neumann rejection scheme [203]. The corresponding phase space points are transformed to Cartesian coordinates,

$$\mathbf{X}_i = \mathbf{X}_{eq} + \frac{\mathbf{L}\mathbf{R}_i}{\sqrt{M\omega}}, \quad (5.2)$$

$$\mathbf{V}_i = \frac{\mathbf{L}\mathbf{P}_i\sqrt{\omega}}{\sqrt{M}}. \quad (5.3)$$

where  $\mathbf{i} = \mathbf{1}, \dots, \mathbf{N}$  is the number of initial states sampled,  $\mathbf{L}$ ,  $\mathbf{M}$ , and  $\omega$  are transformation matrix from the dimensionless normal mode coordinates back to Cartesian coordinates, normal-mode mass, and normal-mode frequency, respectively,  $\mathbf{X}_{eq}$  is the ground-state equilibrium geometry. (3) The sampled geometries were vertically lifted to the outer-valence ionized  $\text{CH}_2\text{O} \cdots \text{ClF}$  electronic state and propagated on that potential energy surface using the FSSH approach. The methodology for the FSSH approach can be found in our previous work [187]. However, a short description of the methodology is given here to make the text more readable.

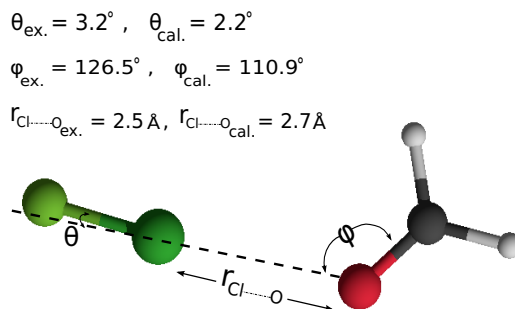


FIGURE 5.1: Ground-state geometry of the  $\text{CH}_2\text{O}\cdots\text{ClF}$  dimer calculated at the HF/ANO-L-VTZP level. The main structural parameters from the calculated ground-state geometry (cal.) are given and compared to the experimental values (ex.) obtained from Ref. Cooke1998.

© 2019, American Chemical Society (ACS)

Electronic structure data such as energies, gradients, and nonadiabatic coupling vectors, were calculated on the fly on the basis of Koopmans' theorem and using the ANO-L-VTZP basis set utilizing the MOLCAS 8.2 package [201]. No decoherence corrections are employed as these corrections are not relevant for the irreversible electronic decay discussed in this study [204].

The three one-hole electronic states are created by removing an electron from each of the three Hartree-Fock (HF) valence molecular orbitals of the neutral dimer i.e., HOMO, HOMO-1, and HOMO-2 creating the ground ( $D_0$ ), the first excited ( $D_1$ ), and the second excited ( $D_2$ ) electronic states of the dimer cation, respectively. The symbol D refers to the doublet character of the states which does not change in the course of dynamics. A total of 100 independent trajectories with a 0.5 fs time step and a total propagation time of 300 fs were employed to approximate the evolution of the nuclear wave packet evolving on the coupled potential energy surfaces. The velocity Verlet algorithm [160] was used to integrate the nuclear equation of motion. The ensemble of independent classical trajectories can be propagated either on precalculated potential energy surfaces or combined with non-adiabatic molecular dynamics “on the fly” [205]. Here, we have created the potential energy surfaces on the fly. The energy of the  $i$ -th

state at every time step is obtained as: [82, 184]

$$V_{i,HF-K} = V_{HF} - \epsilon_i, \quad (5.4)$$

where  $V_{HF}$  is the ground state Hartree-Fock energy of the neutral dimer and  $\epsilon_i$  is the energy of the  $i$ -th occupied orbital with  $i=0$  being the highest occupied orbital. The multiconfigurational capabilities of MOLCAS [201] are used to generate the corresponding electronic wave functions  $|\Psi_i\rangle$  with the orbitals from the HF calculation [187]. Energy gradients and non-adiabatic couplings are obtained on the fly from these configurations employing the RASSI module of the MOLCAS program package [82]. The energies of the three states (roots in the language of the MOLCAS package [201]) are calculated simultaneously at every time step. The molecular system always evolves on a single adiabatic potential energy surface. When the trajectory reaches the vicinity of an intersection of potential energy surfaces and the energy gap between different potential energy surfaces becomes small, the system might hop to another potential energy surface resulting in the breakdown of the Born–Oppenheimer approximation. In these regions, the transition probability to the other potential energy surface is calculated and the trajectory hops to the other surface depending on the comparison of the transition probability with a random number [187].

Each electronic state is described by a single-determinant wave function. This is a valid approximation as long as electron correlation effects are small. In order to assess the validity of the adopted Koopmans’ theorem we compare the potential energy surfaces for the ground, first and second excited states of the dimer cation along the Cl···O reaction coordinate obtained from Koopmans’ theorem and CASCI electronic structure approaches (Figure 5.2).

Figure 5.2a illustrates the Koopmans' theorem based potential energy surfaces employed in our quantum-classical trajectory calculations. In order to generate the potential energy surfaces shown in Figures 5.2b we take into account static electron correlation by expanding the CAS space to five active electrons in eight active orbitals CASCI(5,8). The ANO-L-VTZP basis set is used for the calculations presented in Figure 5.2.

The Cl...O reaction coordinate indicates the halogen bond distance that is the main focus of this study. In particular, we want to show how the halogen bond distance can be transiently shortened through selective ionization. In the next two sections we show how the transient shortening of the halogen bond distance occurs in less than 100 fs, before the covalent bonds start to break. Based on our previous calculations on the benzene cation, a good performance of Koopmans' theorem is expected as long as the chemical process does not involve breakage of covalent bonds [187].

As can be seen from Figure 5.2, the Koopmans' theorem based potential energy surfaces show a similar behavior to those obtained from CASCI(5,8) calculations. This similarity can be explained as follows. 1) The system remains closed shell for all intermolecular distances. It should be noted that in our trajectory calculations all the nuclear degrees of freedom are taken into account during the dynamics and breaking of covalent bonds is observed after a certain time. 2) We have only considered outer valence ionization where the molecular orbital picture is usually valid for small- and medium-size molecules. For a detailed discussion on the validity of the orbital picture see Ref. Cederbaum1986. The use of a non-adiabatic dynamics calculation based on Koopmans' theorem guarantees smooth potential energy surfaces in a high dimensional space, which is a crucial prerequisite for an accurate description of the non-adiabatic dynamics.

Based on both sets of the potential energy curves shown in Figure 5.2, a barrierless

lengthening of the halogen bond is expected after removal of an electron from HOMO (blue curve). However, in the case of the first (red curve) and second (green curve) electronically excited states, the system has the possibility to reach regions of the potential energy surface where the halogen bond distance decreases compared to the ground state neutral dimer.

With the non-adiabatic dynamics, which takes all nuclear degrees of freedom into account, we see a shortening of the halogen bond distance after ionization from HOMO-1. The ionization from HOMO-2 also does not immediately lead to lengthening of the halogen bond. The removal of an electron from HOMO, however, leads to immediate increase in the halogen bond distance as predicted by the potential energy curves in Figure 5.2. These changes of the intermolecular distance in the course of dynamics are rationalized in the following sections on the basis of electrostatic interactions between the partial charges at the atomic positions. The partial charges are calculated based on Mulliken population analysis.

In our trajectory calculations, each time step takes on average 720 seconds on a single core of an Intel Xenon X5660 2.80 GHz CPU. Therefore, about 120 hours of CPU time were needed for the propagation of each trajectory. The energy is conserved at the level of  $\approx 10^{-5}$ . We note that some of the dissociative trajectories are not propagated for the full 300 fs due to SCF convergence problems. In the case of the first electronically excited state, the major convergence problems begin to occur at around 150 fs with about 10 % convergence failure. At about 200 fs, this number reaches 20 %. A steep rise in the convergence failure can be observed between 200 and 300 fs, with 35 % of the total trajectories failing to converge at 300 fs. The fragmentation causes SCF convergence problems.

In the case of the second electronically excited state, fragmentation begins earlier and with a higher probability (121 fs, 54%) as compared to the first excited state. As a

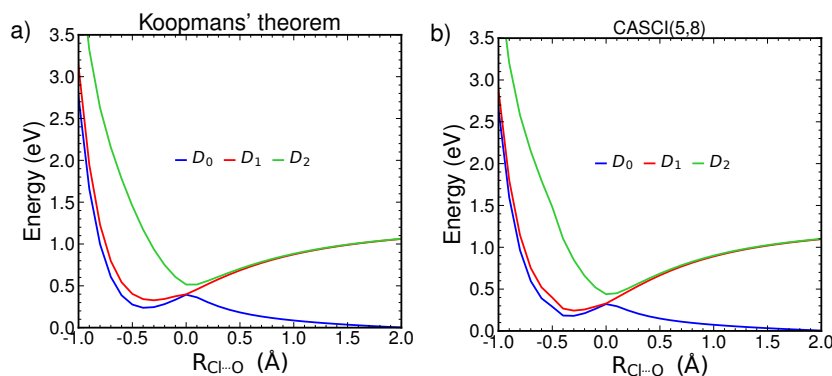


FIGURE 5.2: Cuts through the potential energy surfaces for the ground ( $D_0$ ), first excited ( $D_1$ ), and second excited ( $D_2$ ) electronic states of the  $\text{CH}_2\text{O}\cdots\text{ClF}$  dimer cation calculated at a) Koopmans' level and b) CASCI(5,8). The ANO-L-VTZP basis set is used in both calculations. The intermolecular coordinate is obtained by changing the distance along the ( $\text{Cl}\cdots\text{O}$ ) halogen bond ( $R_{\text{Cl}\cdots\text{O}}$ ) and maintaining the rest of the bonds and the angles at the equilibrium geometry of the neutral dimer.  $R_{\text{Cl}\cdots\text{O}} = 0$  corresponds to the equilibrium intermolecular distance in the neutral dimer. © 2019, American Chemical Society (ACS)

result, the SCF convergence problems are relatively prominent with 20 %, 45 % and 58 % at 100 fs, 200 fs and 300 fs, respectively. In case of the ground state cation, removing an electron from HOMO results in a very fast localization of the positive charge on the  $\text{CH}_2\text{O}$  site leading to early and efficient proton elimination. Thus, the SCF convergence problems due to fragmentation are most prominent when the hole is initially created at HOMO. The percentage of non-converged trajectories at the 100 fs, 200 fs, and 300 fs are around 30 %, 55 %, and 60 % respectively.

### 5.1.1 The first electronically excited state

At the equilibrium geometry of the  $\text{CH}_2\text{O}\cdots\text{ClF}$  dimer, the HOMO (highest occupied molecular orbital) is mostly localized on the  $\text{CH}_2\text{O}$  molecule (Figure 5.3). The HOMO-1, however, is localized on the  $\text{ClF}$  molecule (Figure 5.3) and, therefore, the ionization

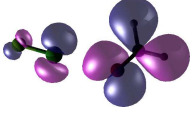
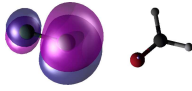
Molecular orbital	HOMO	HOMO-1	HOMO-2
Isosurface			
Orbital energy (eV)	-12.6	-12.8	-12.9
ClF hole population (%)	40	100	60

FIGURE 5.3: Isosurfaces of the three highest molecular orbitals of the  $\text{CH}_2\text{O}\cdots\text{ClF}$  dimer and the corresponding orbital energies calculated at the HF/ANO-L-VTZP level at the equilibrium geometry of the neutral dimer, as well as the partial hole population on the ClF molecule.

© 2019, American Chemical Society (ACS)

out of it creates an initial hole on the ClF molecule which corresponds to the first electronically excited state ( $D_1$ ) of the dimer. Following ionization of the HOMO-1, the dimer starts to relax to its ground electronic state by migration of the initial hole from the HOMO-1 to the HOMO (Figure 5.4b), which is equivalent to saying that the electronic charge starts to move from the  $\text{CH}_2\text{O}$  molecule to the ClF molecule (Figure 5.4a). The HOMO is delocalized over the  $\text{CH}_2\text{O}$  and the ClF molecules with about 60 % localization on the  $\text{CH}_2\text{O}$  (Figure 5.3). The intermolecular charge transfer dynamics and the electronic population decay after creating the initial hole on the ClF molecule are shown in Figures 5.4a,b, respectively. About 50 % of the hole initially created on the ClF molecule moves to the  $\text{CH}_2\text{O}$  molecule within the first 120 fs and only 10 % of the hole remains on the ClF molecule by the end of the propagation time. The electronic population decay and the intermolecular charge transfer processes show a similar temporal evolution with a similar half-life of around 100 and 120 fs, respectively (Figure 5.4). The origin of the direction of the charge transfer lies in the fact that electrons tend to flow towards the molecular orbital with a lower energy, which is here localized on the ClF molecule. The localization of the HOMO-1 on the ClF molecule can be understood from the higher electronegativity of the Cl and F

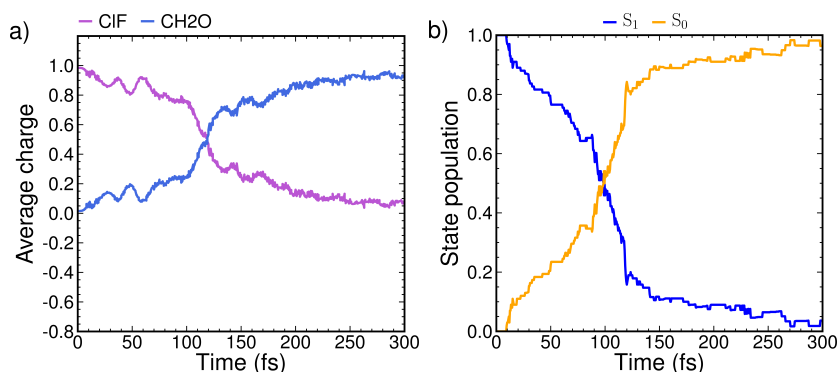


FIGURE 5.4: Dynamics of: (a) intermolecular charge transfer, and (b) electronic population, averaged over 100 trajectories for an initial excitation to the  $D_1$  of the dimer cation. © 2019, American Chemical Society (ACS)

atoms compared to the atoms that constitute the CH<sub>2</sub>O molecule. This shows how one can control the direction of the intermolecular charge flow by gathering the atoms with higher electronegativity on one of the molecular units in a dimer.

The charge oscillations on each individual atom and the covalent bond oscillations are given in Figures 5.5a, b. An initial glance at Figure 5.5a indicates oscillatory patterns of charge fluctuation in the first 80 fs, during which the charge of the atomic sites oscillates with the same frequency as the relevant covalent bonds vibrate (Figure 5.5b). The Fourier transform of the O atom's charge oscillation and the C=O stretch vibration in the 0-80 fs time window shows a main peak at the same frequency of  $1667\text{ cm}^{-1}$  (20 fs). The same frequency is also seen in the Fourier transform of the F atom's charge oscillation in the 0-80 fs time window. This shows that the charge oscillations of the O and F atoms are governed by the C=O stretch vibration. In addition, the phases of the charge oscillation at the O and F atoms are the same. This same phase oscillation can be explained by the polarization effect. The rise of the negative charge on the O atom polarizes the electron density at the neighboring CIF molecule by pushing the electrons towards the F atom. In the 0-80 fs time interval, the Fourier transforms of the CH stretch vibration and the two H atoms' charge oscillation show a main peak

at  $2918\text{ cm}^{-1}$  (11 fs). Thus, the charge oscillations of the H atomic sites are driven by the CH stretch vibrations.

The charge dynamics at each individual atom (Figure 5.5a) helps in understanding the temporal evolution of the electrostatic interaction, which is connected to the halogen bond distance and to the structural dynamics in general (Figures 5.5c, 5.6). For the first 90 fs, while more than 50 % of the hole population is still located on the Cl atom, the intermolecular distance decreases, which is reflected in a reduction of the Cl $\cdots$ O (halogen bond) and F $\cdots$ O distance by 0.3 Å and 0.25 Å, respectively (Figure 5.5c).

The shortening of the halogen bond distance can be explained by the electrostatic interaction between the positive charge on the Cl atom and the negative charge on the O atom (Figure 5.5a). At 90 fs, the charge on the Cl atom decreases by 0.2  $e$  and reaches a value of 0.9  $e$ . In the same time interval, the O atom's charge oscillates between -0.5  $e$  and -0.3  $e$ . Thus, the simple electrostatic interaction between the positive charge on the Cl atom and the negative charge on the O atom results in decreasing the distance between the two molecules.

Although the halogen bond is considered to be a primarily electrostatic interaction [94], it should be noted that in the ground electronic state of the neutral dimer, the positive charge on the halogen bond donor (electron acceptor) is induced by the electron-withdrawing group connected to it. However, the existence of the positive charge on the Cl atom here is the result of the ionization. Therefore, the excited-state halogen bond in the dimer cation differs from the ground state halogen bond in the neutral dimer. To distinguish between the two halogen bonds, we name the former  $D_1^{i+}$  halogen bond, where  $D_1$  stands for the first electronic excited state and the  $i+$  indicates a single ionization. After 90 fs of the initial time, the positive charge on the Cl atom and the negative charge on the O atom show a dramatic decrease that leads to the weakening of the  $D_1^{i+}$  halogen bond reflected in an increase in the Cl $\cdots$ O distance

(Figure 5.5c, and Figure 5.6). The Cl $\cdots$ O distance then keeps increasing till the end of the computed dynamics. The F $\cdots$ O distance, however, shows a decreasing trend in the 0-150 fs time interval. This decreasing trend is because of the attractive interaction between the positive charge of the H atom and the negative charge of the F atom (Figure 5.5a). After 150 fs, the F atom is the only negative site in the whole system and, therefore, the positive atoms of the formaldehyde will be competing over interacting with it. The ClF molecule finally rotates and the F atom moves closer to the CH<sub>2</sub>O molecule (Figure 5.6). The initial charge oscillations and bond vibrations become slower as the hole population on the CH<sub>2</sub>O molecule increases until a CH bond finally breaks. In a previous study we showed that our Koopmans' based approach overestimates the dissociation barrier of the covalent bonds and, thus, underestimates the fragmentation yield; the fragments observed in our calculations were, however, similar to those observed in the corresponding experiments. Thus, the fragmentation probability is expected to be higher in reality. The single-proton elimination with 44 % probability starts at around 181 fs and shortly thereafter, at around 208 fs, the second CH bond breaks apart with 11 % probability. The single-proton elimination at 250 fs can be seen in Figure 5.6. The effect of CH dissociation can not be clearly seen in (Figure 5.5b), because some of the trajectories that undergo CH dissociation are not propagated for the full 300 fs due to SCF convergence problems (see computational methods section).

### 5.1.2 The second electronically excited state

Unlike the first excited state, the second electronically excited state ( $D_2$ ) is created by removing an electron from an orbital that is delocalized over the two molecules. The HOMO-2 is delocalized over the ClF and CH<sub>2</sub>O molecules with a 60 % localization on the ClF molecule (Figure 5.3). As explained in the previous section, the electronic

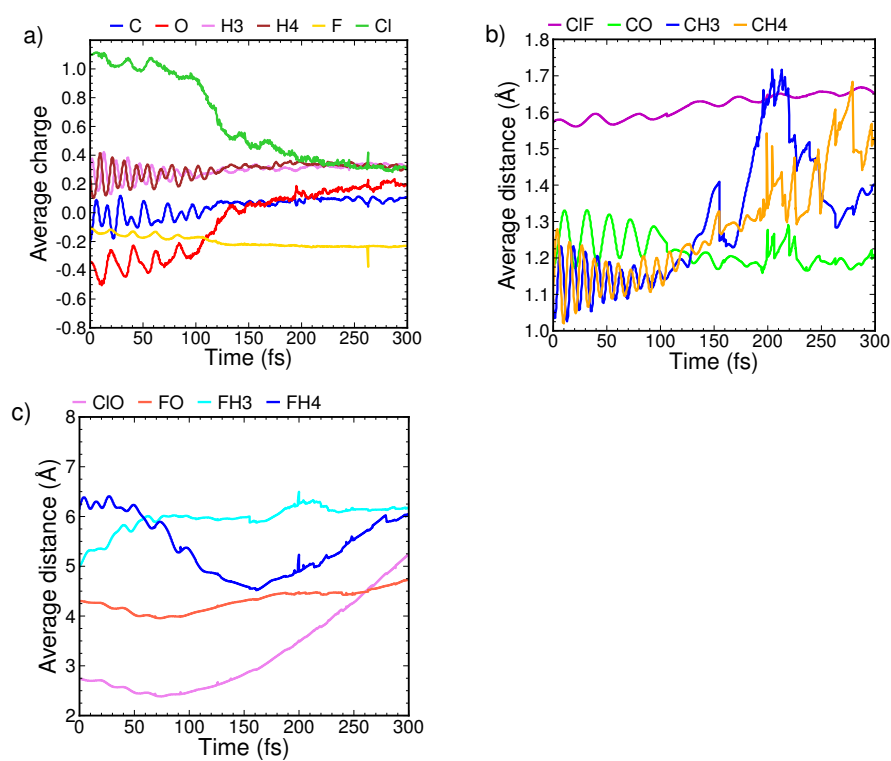


FIGURE 5.5: Temporal evolution of: (a) atomic charges, (b) intramolecular distances, and (c) intermolecular distances, averaged over 100 trajectories for an initial excitation to the  $D_1$  of the dimer cation. © 2019, American Chemical Society (ACS)

charge tends to flow towards the ClF molecule because it contains the most electronegative atoms in the dimer. In other words, the evolution of the system from an initial state where the hole is mostly located on the electron acceptor (the ClF molecule) to a final state where the hole is moved to the electron donor (the CH<sub>2</sub>O molecule) is driven by energetic stabilization.

According to Figure 5.7, for the first 80 fs, charge transfer fluctuations occur before the hole irreversibly transfers to the CH<sub>2</sub>O molecule. At 80 fs, the  $D_2$  is completely depopulated and, therefore, the  $D_1$  and  $D_0$  populations start to mirror each other (Figure 5.7b). The  $D_1$  and  $D_0$  correspond to the HOMO-1, localized on the ClF molecule, and the HOMO, mostly localized on the CH<sub>2</sub>O molecule. Thus, as electronic population moves from the  $D_1$  to the  $D_0$ , the hole is irreversibly transferred from the ClF to the CH<sub>2</sub>O molecule (Figure 5.7a) and the charges of the two molecular sites mirror each other.

The driving force behind the charge oscillations is the nuclear displacements. The bond vibrations during the course of dynamics are shown in Figure 5.8a. The Fourier transform of the CH bond vibrations within the first 50 fs shows a main peak at a frequency of 2668 cm<sup>-1</sup>, corresponding to a period of 12.5 fs. The Fourier transform of the intermolecular charge oscillations in the same time interval shows a main peak at the same frequency. Therefore, the CH stretching vibrations are the driving force behind the large intermolecular charge oscillations. The transient increase of the ClF positive charge during charge fluctuations may seem counterintuitive at first, considering the high electronegativity of the Cl and F atoms. The electronic population of the second electronically excited state ( $D_2$ ) decays very fast (half-life of 20 fs) to the lower electronically excited states (Figure 5.7b). During the first 20 fs, while more than 50 % of the hole population is still in the HOMO-2, the charge shows large oscillations (Figure 5.7a) between the two molecular units. The delocalization of the HOMO-2

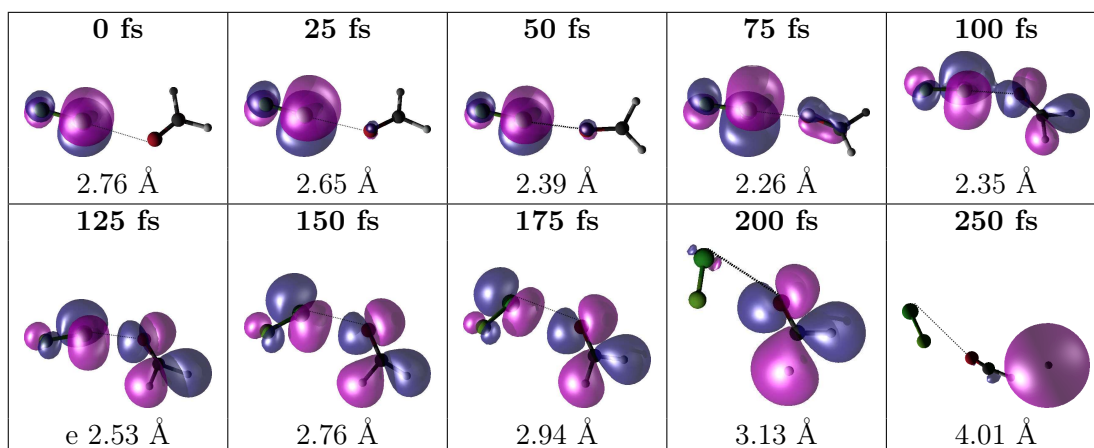


FIGURE 5.6: Time evolution of the nuclear motion and the molecular orbital accommodating the hole in a representative trajectory for an initial excitation to the  $D_1$  of the dimer cation. The distance between the Cl and O atoms is given in Å. © 2019, American Chemical Society (ACS)

over the two moieties allows the charge to transfer back and forth between them. As the  $D_2$  population decreases, the intermolecular charge oscillations become smaller until 80 fs (Figure 5.7b), when the  $D_2$  population vanishes and the hole irreversibly flows from the ClF molecule to the  $\text{CH}_2\text{O}$  molecule.

In a previous study of the attosecond charge dynamics in tryptophan [206], the appearance of more electronic charge on functional groups with less electron affinity than on functional groups with large electron affinity were considered counterintuitive. However, it can be rationalized considering the fact that these oscillations occur when the system is electronically excited, which means it may transiently display the charge distributions that are not the most stabilizing ones until it reaches the ground-state charge distribution, where the charge is distributed according to the electronegativity of the groups and the atoms, i.e., the most electronegative groups bear the least hole population. It should be noted that the driving force for the computed attosecond charge dynamics in tryptophan [206] is the electronic coherence. Here, energetic stabilization is the driving force of the charge transfer and the charge oscillations are

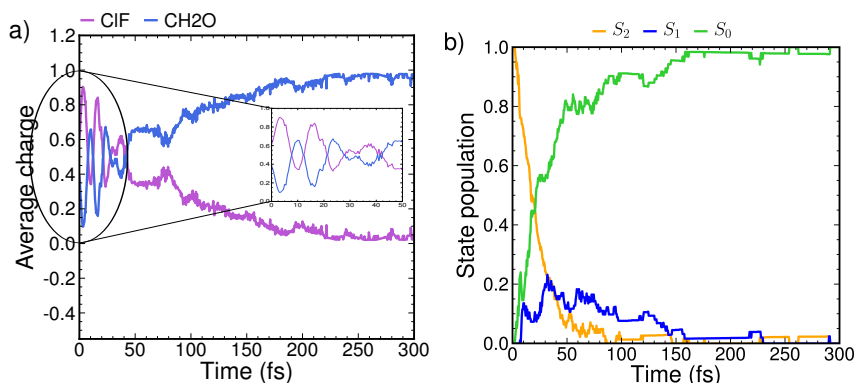


FIGURE 5.7: Dynamics of: (a) intermolecular charge transfer, and (b) electronic population, averaged over 100 trajectories for an initial excitation to the  $D_2$  of the dimer cation. © 2019, American Chemical Society (ACS)

governed by the corresponding covalent-bond vibrations.

The charge fluctuations of the atomic sites and of the  $\text{CH}_2$  group are shown in Figure 5.8a. During the first 20 fs, the charges of the O, Cl, F and the  $\text{CH}_2$  sites oscillate with the same period as the CH bond vibrates. This same periodic behavior is due to the delocalization of the HOMO-2 orbital over the mentioned sites. In the same time interval, the charges of the O and  $\text{CH}_2$  sites oscillate out of phase with respect to the Cl and F atoms, which is an indication of an intermolecular charge transfer oscillation. The charge dynamics of each individual atom also helps to understand the temporal evolution of the halogen bond through the electrostatic interaction. The electrostatically driven halogen bond created following ionization out of the HOMO-2 is called  $D_2^{i+}$  halogen bond here, where  $D_2$  stands for the second electronic excited state and the  $i+$  indicates a single ionization. The  $\text{Cl}\cdots\text{O}$  distance remains almost constant for the first 80 fs (Figure 5.8c). During this time interval, the Cl atom's positive charge and the O atom's negative charge fluctuate between 1.1 to 0.5  $e$  and -0.3 to 0.0  $e$ , respectively (Figure 5.8a). In the 80-300 fs time interval, the charge of both the O atom and the Cl atom is positive. Thus, the  $D_2^{i+}$  halogen bond vanishes and the  $\text{Cl}\cdots\text{O}$  distance keeps increasing till the end of the computed dynamics (Figures 5.8c,

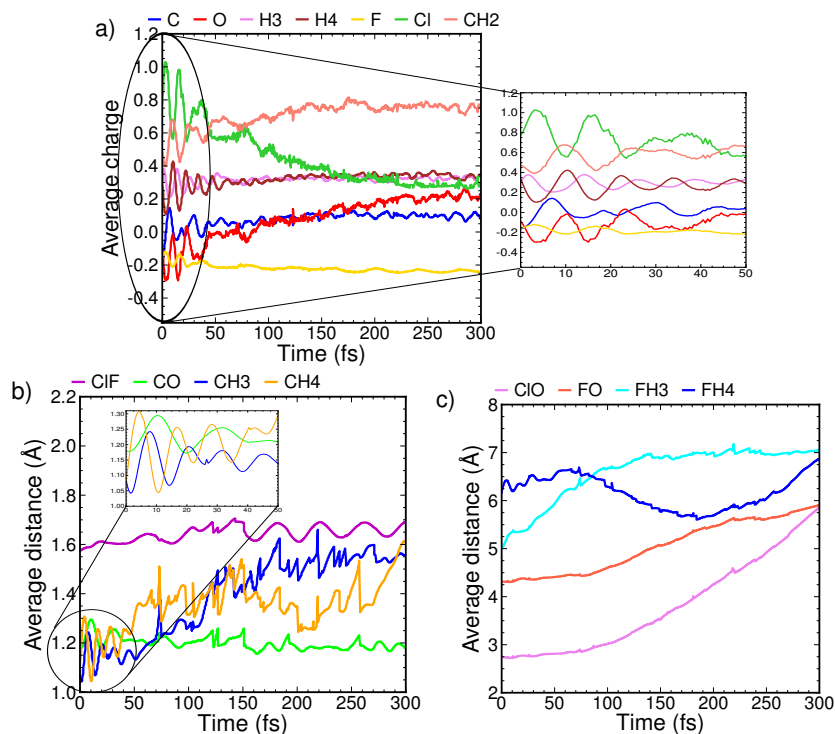


FIGURE 5.8: Temporal evolution of: (a) atomic charges, (b) intramolecular distances, and (c) intermolecular distances, averaged over 100 trajectories for an initial excitation to the  $D_2$  of the dimer cation. © 2019, American Chemical Society (ACS)

5.9). The  $F \cdots H_4$  distance, however, starts to decrease between 80 and 190 fs, which is an indication of the rotation of the two molecules towards each other in a way that the F atom of the ClF gets closer to the H atom of the  $CH_2O$  (Figures 5.8c, 5.9). This rotation can be understood by looking at the atomic charge dynamics (Figures 5.8a). During the 80-190 fs time interval, the F atom is the only negative site in the dimer with a charge of  $-0.2 e$  and the  $CH_2$  group possesses the highest positive charge ( $0.7 e$ ). Therefore, the electrostatic interaction between the negative charge of the F atom and the positive charge of the  $CH_2$  group causes the rotation of the ClF molecule, as shown in Figure 5.9. The single proton elimination with 54 % probability starts at around 125 fs and 12 fs thereafter, the second CH bond breaks apart with 11 % probability. The effect of CH dissociation cannot clearly be seen in Figure 5.8b, because some of

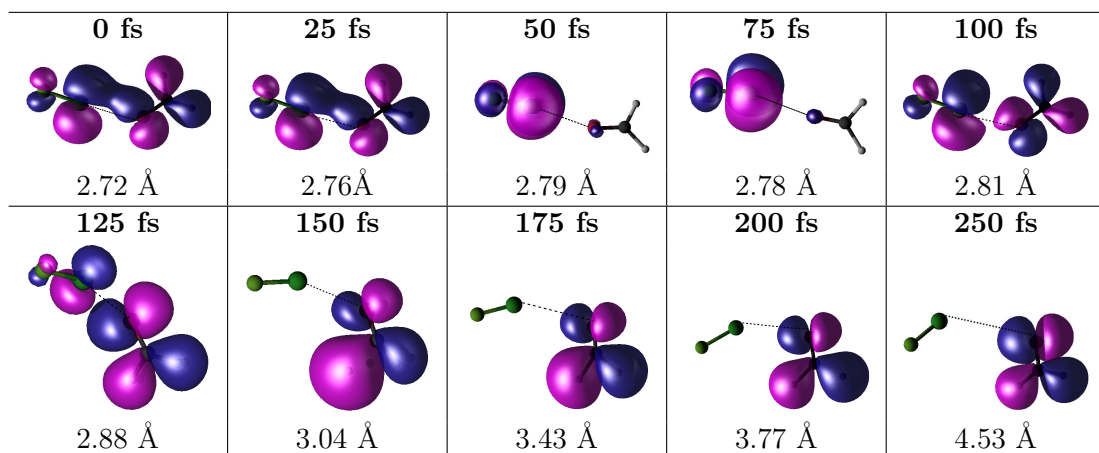


FIGURE 5.9: Time evolution of the nuclear motion and molecular orbital accommodating the hole in a representative trajectory for an initial excitation to the  $D_2$  of the dimer cation. The distance between the Cl and O atoms is given in Å. © 2019, American Chemical Society (ACS)

the trajectories that undergo CH dissociation are not propagated for the full 300 fs due to SCF convergence problems. As already mentioned, the fragmentation probability is expected to be underestimated in this study.

### 5.1.3 The ground state

The HOMO is delocalized over the  $\text{CH}_2\text{O}$  and ClF molecules with about 60 % localization on the  $\text{CH}_2\text{O}$  molecule (Figure 5.3). Removing an electron from the HOMO brings the halogen-bonded dimer to its cationic electronic ground state. Following ionization, the charge density of the dimer changes to adopt the charge distribution of the cation in its ground state. There is no coupling with other potential energy surfaces. Therefore, the dynamics in this case are purely adiabatic. The change in the charge density pattern is reflected by a sudden electronic charge transfer from the  $\text{CH}_2\text{O}$  molecule to the ClF molecule. The intermolecular charge transfer following ionization occurs in the first 6 fs, which leads to an increase in the positive charge of the  $\text{CH}_2\text{O}$  molecule by about  $0.4 e$  (Figure 5.10); the hole then stays localized at the

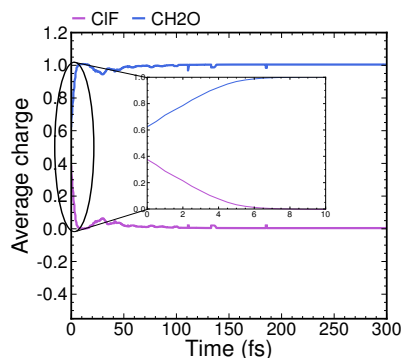


FIGURE 5.10: Dynamics of the intermolecular charge transfer, averaged over 100 trajectories, following ionization out of the HOMO. © 2019, American Chemical Society (ACS)

CH<sub>2</sub>O molecule till the end of propagation time. Localization of the positive charge on the CH<sub>2</sub>O molecule is due to the higher electron affinity of the ClF molecule, which pulls the electrons out of the CH<sub>2</sub>O molecule. The charge fluctuations of the atomic sites and at the CH<sub>2</sub> group are shown in Figure 5.11a. As can be seen, the intermolecular charge transfer mainly occurs between the CH<sub>2</sub> group of the CH<sub>2</sub>O molecule and the Cl atom of the ClF molecule. Comparing the charge oscillations (Figure 5.11a) and the CH-bond vibrations (Figure 5.11b) within the first 10 fs, indicates that the intermolecular charge transfer is associated with the CH bond's dynamics. The first CH bond dissociates on average after 88 fs of the propagation with 64 % probability and 10 fs thereafter the second CH bond dissociates with a probability of 21 %. The effect of CH dissociation on the CH length averaged over all the trajectories cannot be seen in Figure 5.11b because some of the trajectories that undergo dissociation are not propagated for the full 300 fs due to SCF convergence problems. ClF molecule remains intact for the entire propagation time. The Fourier transform of the Cl–F stretch vibration shows a main peak at 889 cm<sup>-1</sup> (37 fs). The Fourier transform of the charge oscillations of the Cl and F atoms shows a main peak at the same frequency of 889 cm<sup>-1</sup>. Therefore, the Cl–F stretch vibration is the driving force of the charge oscillations on the Cl and F atomic sites.

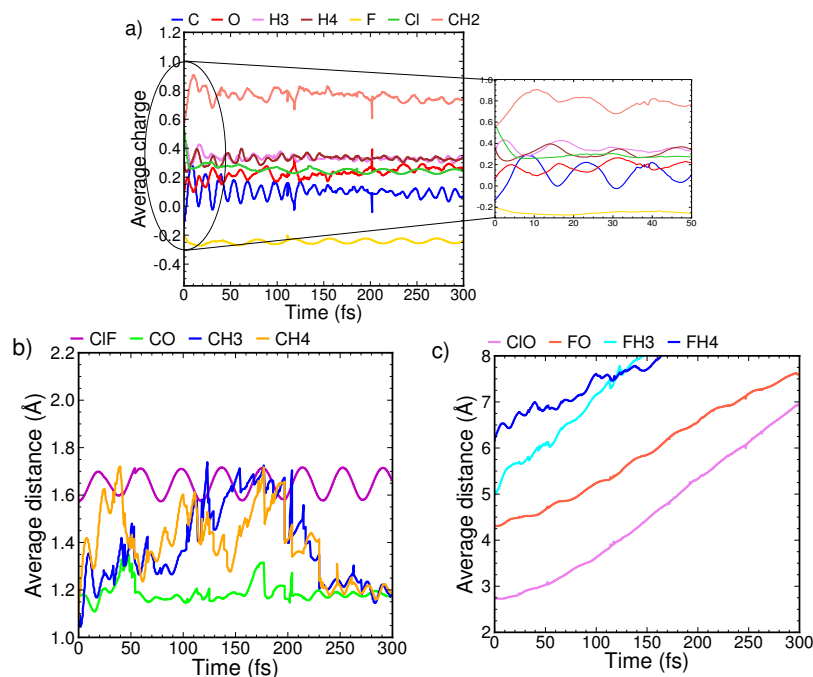


FIGURE 5.11: Temporal evolution of: (a) atomic charges and charge of the  $\text{CH}_2$  group, (b) intramolecular distances, and (c) intermolecular distances, averaged over 100 trajectories, following ionization out of the HOMO. © 2019, American Chemical Society (ACS)

According to Figure 5.11c, the  $\text{CH}_2\text{O}$  and ClF molecules begin to move away from each other about 10 fs after the initial electron removal due to the electrostatic repulsion between the two molecular units. The charge of the O atom becomes positive after about 10 fs (Figure 5.11a). Therefore, the singly ionized halogen-bonded dimer in its ground electronic state survives for only 10 fs before its two molecular units move apart.

## Chapter 6

# Conclusions and Outlook

Within my doctoral work I investigated the femtochemistry of three different molecular systems: (I) H<sub>2</sub>O and its deuterated isotopologues; (II) the benzene radical cation, and (III) CH<sub>2</sub>O···ClF halogen-bonded dimer. The theory employed in this thesis is based on a nonadiabatic mixed quantum-classical approach in which the nuclear motions were treated classically by Newton's equations of motion and the electrons were described quantum mechanically.

Since water is a simple and relatively small molecule, we used a relatively high-level method, i.e., CASSCF for on-the-fly ab-initio calculations of its electronic structure data, energies, energy gradients, and non-adiabatic couplings. The photochemistry of the two other molecular systems, i.e., the benzene radical cation, and CH<sub>2</sub>O···ClF halogen-bonded dimer, was described by a Koopmans' theorem based approach.

In chapter 3, I present a joint experimental and theoretical study of the VUV-induced dynamics of H<sub>2</sub>O and its deuterated isotopologues in the first excited state ( $\tilde{A}^1B_1$ ) utilizing a VUV-pump VUV-probe scheme. Our results disclose the time it takes the dissociating molecule to leave the photoionization window. Vertical excitation energies and photoionization cross sections along the reaction coordinate were calculated, resulting in the delay-dependence of the vertical ionization energy from the  $\tilde{A}^1B_1$  state to the electronic ground and first excited states of the ion for an evolving wave-packet,

which is pivotal in the interpretation of the pump-probe experiment. The experimentally deduced time of 6.7 fs that the H<sub>2</sub>O molecule takes to leave the single-photon ionization window while dissociating, as well the influence of hydrogen substitution (7.5 fs for HDO and 9.4 fs for D<sub>2</sub>O), were consistent with the trajectory calculations. The corresponding calculated times are 6.4 fs, 8.2 fs, and 10.4 fs, for H<sub>2</sub>O, HDO, and D<sub>2</sub>O, respectively.

In the XUV photochemistry simulations of the benzene radical cation (chapter 4) I investigated the non-adiabatic dynamics of singly ionized benzene on fifteen coupled potential energy surfaces. Trajectories excited to different states were propagated employing the fewest switches surface hopping approach while forces and non-adiabatic couplings were obtained at the level of Koopmans' theorem excitations. I addressed two fundamental aspects of the XUV photochemistry: the time resolved relaxation of the electronically excited states through internal conversion and the time-resolved state-specific fragmentation dynamics.

Good performance of the Koopmans' theorem based approach was found for the non-adiabatic relaxation process. Excitations to the lowest six states largely decayed to the ground state within 100 fs, while the highest lying states were stable up to the final propagation time of 300 fs. For most initial excitations we found good agreement with previous simulations employing reduced-dimensional quantum dynamics approaches. Nevertheless, for initial excitation to the  $\tilde{D}^2E_{1u}$  state, we found fast decay to the ground state in contrast to previous calculations which find a slow, gradual decay. The longer lifetime of the higher-lying states can be explained by large energy gaps to other states. Including shake-up states in the electronic structure calculations could alter the life time of the high-lying states. However, our simulations underestimated the dissociation probability compared to experiments due to an overestimation of the

dissociation energies in the adopted Koopmans' theorem based electronic structure calculations. This highlights the challenges in simulating XUV induced photochemistry of medium-sized systems, where a large number of excited states as well as several dissociation channels have to be described. The challenge to develop accurate, yet efficient ab initio models that describe the fragmentation yields upon XUV irradiation remains to be solved in future research.

Albeit, for certain systems, it might be possible to simulate the short time non-adiabatic conversion to the ground state employing the Koopmans' theorem based approach described here and then employ a statistical theory to describe the dissociation on the ground state potential energy surface employing a highly accurate electronic structure method.

Finally, in chapter 5, I studied ultrafast charge transfer and structural dynamics following outer valence ionization of  $\text{CH}_2\text{O} \cdots \text{ClF}$  halogen-bonded dimer. Halogen bonding is mainly driven by electrostatic interaction. Thus, any change in the charge density pattern of a halogen-bonded system that alters the electrostatic interaction will affect the halogen-bond strength.

The introduction of a change in the charge density of a molecular system can take place in different ways, e.g., by chemical substitution, external fields, electronic excitation and ionization. We used outer-valence ionization to initiate a charge density change in the  $\text{CH}_2\text{O} \cdots \text{ClF}$  halogen-bonded dimer, which is followed by charge and structural dynamics on the femtosecond time scale. This study used a nonadiabatic mixed quantum-classical dynamics approach that combines the Tully's fewest switches surface hopping algorithm with a Koopmans' theorem-based electronic structure method. Following ionization of HOMO-1, a positive charge was initially created on the Cl atom, leading to an increase in the attractive electrostatic interaction between the Cl and O atoms that manifested itself in a decrease in the halogen-bond distance by 0.3

Å in the course of 90 fs. As the hole moves from the HOMO-1 to HOMO (internal conversion), electronic charge moves from the CH<sub>2</sub>O to the ClF molecule, changing the structure of the dimer and the strength of the halogen bond during the 300 fs of propagation time. Ionization out of the HOMO, however, breaks the halogen bond following the creation of a positive charge on the oxygen atom.

I showed that the charge dynamics is exclusively driven by the energetic stabilization and by the nuclear dynamics. I hope that this work inspires further research on the control of halogen-bond interactions through ionization or electronic excitation with potential applications in drug design and drug delivery, solar energy conversion, and anion recognition, to name a few.

# Bibliography

- [1] W. Haynes, *Ultrafast Dynamics of the Chemical Bond. 1 and 2*. Singapore: World Scientific, **1994**.
- [2] M. A.-E. et al., *Tesla technical design report, part 5: The x-ray free electron laser*, Tech. rep, DESY, **2001**.
- [3] R. de Nalda, L. Bañares, *Ultrafast Phenomena in Molecular Sciences: Femtosecond Physics and Chemistry*, Springer Cham Heidelberg New York Dordrecht London, **2014**.
- [4] J. Feldhaus, *J. Phys. B* **2010**, *43*.
- [5] A. Zewail, *Sci. Am.* **1990**.
- [6] H. Eyring, M. Polanyi, *Z. Phys. B12* **1931**, *279*, 279–311.
- [7] M. Born, R. Oppenheimer, *Annalen der Physik* **1927**, *389*, 457–484.
- [8] I. Levine, *Quantum Chemistry*, Pearson Education, **2013**.
- [9] L. Landau, *Phys. Z. Sowjetunion* **1932**, *2*, 46–51.
- [10] C. Zener, *Proc. R. Soc. Lond. A.* **1932**, *137*, 696–702.
- [11] E. Stückelberg, *Helv. Phys. Acta.* **1932**, *5*, 369.
- [12] F. London, *Zeitschrift für Physik* **1932**, *74 (3-4)*, 143–174.
- [13] X. Zhou, P. Ranitovic, C. Hogle, J. Eland, H. Kapteyn, M. Murnane, *Nat. Phys.* **2012**, *8*, 232–237.

## BIBLIOGRAPHY

---

- [14] V. Gorshkov, S. Tretiak, D. Mozyrsky, *Nat. Commun.* **2013**, *4*.
- [15] R. Mathies, C. Brito Cruz, W. Pollard, C. Shank, *Science* **1988**, *240*, 777–779.
- [16] J. Clark, T. Nelson, S. Tretiak, G. Cirmi, G. Lanzani, *Nat. Phys.* **2012**, *8*, 225–231.
- [17] M. Sato, S. Adachi, T. Suzuki, *J. Phys. Chem. A* **2016**, *120*, 5099–5102.
- [18] O. Schalk, M. Schuurman, G. Wu, P. Lang, M. Mucke, R. Feifel, A. Stolow, *J. Phys. Chem. A* **2014**, *118*, 2279–2287.
- [19] A. Lamola, G. Hammond, *J. Chem. Phys.* **1965**, *43*, 2129–2135.
- [20] K. Goushi, K. Yoshida, K. Sato, C. Adachi, *Nat Photonics* **2012**, *6*, 253–258.
- [21] A. Hauser, *J. Chem. Phys.* **1991**, *94*, 2741–2748.
- [22] K. Saita, M. Takagi, Y. Harabuchi, H. Okada, S. Maeda, *J. Chem. Phys.* **2018**, *149*.
- [23] P. Hartnett, C. Mauck, M. Harris, R. Young, Y.-L. Wu, T. Marks, M. Wasielewski, *J. Am. Chem. Soc.* **2017**, *139*, 749–756.
- [24] M. Kim, L. Shen, H. Tao, T. Martinez, A. Suits, *Science* **2007**, *315*, 1561–1565.
- [25] T. Goodson III, *Acc. Chem. Res.* **2005**, *38*, 99–107.
- [26] P. Peumans, S. Uchida, S. Forrest, *Nature* **2003**, *425*, 158–162.
- [27] E. Collini, G. Scholes, *Science* **2009**, *323*, 369–373.
- [28] G. Scholes, G. Fleming, A. Olaya-Castro, R. Van Grondelle, *Nat Chem.* **2011**, *3*, 763–774.
- [29] T. Shimizu, M. Sugiura, T. Noguchi, *J. Phys. Chem. B* **2018**, *122*, 9460–9470.
- [30] G. W. H.-D. Meyer, F. Gatti, *Multidimensional quantum dynamics: MCTDH theory and applications*, Wiley, Weinheim, **2009**.

- [31] R. Crespo-Otero, M. Barbatti, *Chem. Rev.* **2018**, *118*, 7026–7068.
- [32] C. Martens, J.-Y. Fang, *J. Chem. Phys.* **1997**, *106*, 4918–4930.
- [33] R. Kapral, *J. Chem. Phys.* **1999**, *110*, 8919–8929.
- [34] D. Mac Kernan, G. Ciccotti, R. Kapral, *J. Phys. Chem. B* **2008**, *112*, 424–432.
- [35] G. Stock, M. Thoss, *Phys. Rev. Lett.* **1997**, *78*, 578–581.
- [36] M. Thoss, G. Stock, *Phys. Rev. A* **1999**, *59*, 64–79.
- [37] F. Agostini, S. Min, A. Abedi, E. Gross, *J. Chem. Theory Comput.* **2016**, *12*, 2127–2143.
- [38] H.-J. Werner, *Adv. Chem. Phys.* **1987**, *69*, 1–69.
- [39] P. Saxe, B. Lengsfeld III, D. Yarkony, *Chem. Phys. Lett.* **1985**, *113*, 159–164.
- [40] H. Lischka, M. Dallos, P. G. Szalay, D. R. Yarkony, R. Shepard, *J. Chem. Phys.* **2004**, *120*, 7322–7329.
- [41] X. Zhu, D. R. Yarkony, *J. Chem. Phys.* **2016**, *144*, 024105.
- [42] B. O. Roos, *Adv. Chem. Phys.* **1987**, *69*, 399–445.
- [43] K. Andersson, P.-A. Malmqvist, B. Roos, *J. Chem. Phys.* **1992**, *96*, 1218–1226.
- [44] G. Roberts, C. Williams, J. Young, S. Ullrich, M. Paterson, V. Stavros, *J. Am. Chem. Soc.* **2012**, *134*, 12578–12589.
- [45] X. Guo, Y. Zhao, Z. Cao, *J. Phys. Chem. A* **2014**, *118*, 9013–9020.
- [46] G. Cui, W. Fang, *J. Phys. Chem. A* **2011**, *115*, 1547–1555.
- [47] J. Schönborn, J. Sielk, B. Hartke, *J. Phys. Chem. A* **2010**, *114*, 4036–4044.
- [48] H. Tao, B. Levine, T. Martínez, *J. Phys. Chem. A* **2009**, *113*, 13656–13662.
- [49] K. Andersson, P. A. Malmqvist, B. O. Roos, A. J. Sadlej, K. Wolinski, *J. Phys. Chem.* **1990**, *94*, 5483–5488.

- [50] J. Segarra-Martí, A. Francés-Monerris, D. Roca-Sanjuán, M. Merchán, *Molecules* **2016**, *21*, 1666–1683.
- [51] S. Keller, K. Boguslawski, T. Janowski, M. Reiher, P. Pulay, *J. Chem. Phys.* **2015**, *142*, 245–278.
- [52] O. Christiansen, H. Koch, P. Jørgensen, *Chem. Phys. Lett.* **1995**, *243*, 409–418.
- [53] G. D. Purvis, R. J. Bartlett, *J. Chem. Phys.* **1982**, *76*, 1910–1918.
- [54] J. Schirmer, *Phys. Rev. A* **1982**, *26*, 2395–2416.
- [55] J. Schirmer, A. Trofimov, *J. Chem. Phys.* **2004**, *120*, 11449–11464.
- [56] A. Trofimov, G. Stelter, J. Schirmer, *J. Chem. Phys.* **1999**, *111*, 9982–9999.
- [57] A. Trofimov, G. Stelter, J. Schirmer, *J. Chem. Phys.* **2002**, *117*, 6402–6410.
- [58] F. Mertins, J. Schirmer, *Phys. Rev. A* **1996**, *53*, 2140–2152.
- [59] A. Dreuw, M. Wormit, *Wiley Interdiscip. Rev.: Comput. Mol. Sci.* **2015**, *5*, 82–95.
- [60] C. Krauter, B. Schimmelpfennig, M. Pernpointner, A. Dreuw, *Chem. Phys.* **2017**, *482*, 286–293.
- [61] A. Marciniak, V. Despré, T. Barillot, A. Rouzée, M. Galbraith, J. Klei, C.-H. Yang, C. Smeenk, V. Loriot, S. Reddy, A. Tielens, S. Mahapatra, A. Kuleff, M. Vrakking, F. Lépine, *Nat. Commun.* **2015**, *6*, 7909–7914.
- [62] D. Tuna, D. Lefrancois, L. Wolański, S. Gozem, I. Schapiro, T. Andruniów, A. Dreuw, M. Olivucci, *J. Chem. Theory Comput.* **2015**, *11*, 5758–5781.
- [63] F. Plasser, R. Crespo-Otero, M. Pederzoli, J. Pittner, H. Lischka, M. Barbatti, *J. Chem. Theory Comput.* **2014**, *10*, 1395–1405.
- [64] C. Walter, V. Krämer, B. Engels, *Int. J. Quantum Chem.* **2017**, *117*, e25337–e25350.

- [65] R. Bauernschmitt, R. Ahlrichs, *Chem. Phys. Lett.* **1996**, *256*, 454–464.
- [66] J. Zhao, H. Yao, J. Liu, M. Hoffmann, *J. Phys. Chem. A* **2015**, *119*, 681–688.
- [67] S. Chai, G.-J. Zhao, P. Song, S.-Q. Yang, J.-Y. Liu, K.-L. Han, *Phys. Chem. Chem. Phys.* **2009**, *11*, 4385–4390.
- [68] G.-J. Zhao, K.-L. Han, *J. Comput. Chem.* **2008**, *29*, 2010–2017.
- [69] D. Yang, G. Yang, J. Zhao, R. Zheng, Y. Wang, *RSC Adv.* **2017**, *7*, 1299–1304.
- [70] E. Runge, E. Gross, *Phys. Rev. Lett.* **1984**, *52*, 997–1000.
- [71] W. Liu, V. Settels, P. Harbach, A. Dreuw, R. Fink, B. Engels, *J. Comput. Chem.* **2011**, *32*, 1971–1981.
- [72] K. Komoto, T. Kowalczyk, *J. Phys. Chem. A* **2016**, *120*, 8160–8168.
- [73] A. Becke, *Phys. Rev. A* **1988**, *38*, 3098–3100.
- [74] J. Perdew, *Phys. Rev. B* **1986**, *33*, 8822–8824.
- [75] A. Becke, *J. Chem. Phys.* **1993**, *98*, 5648–5652.
- [76] P. Stephens, F. Devlin, C. Chabalowski, M. Frisch, *J. Phys. Chem.* **1994**, *98*, 11623–11627.
- [77] M. Casida, C. Jamorski, K. Casida, D. Salahub, *J. Chem. Phys.* **1998**, *108*, 4439–4449.
- [78] S. Grimme, M. Parac, *ChemPhysChem* **2003**, *4*, 292–295.
- [79] Y.-L. Wang, G.-S. Wu, *Int. J. Quantum Chem.* **2008**, *108*, 430–439.
- [80] M. Huix-Rotllant, A. Nikiforov, W. Thiel, M. Filatov, *Description of Conical Intersections with Density Functional Methods*, Springer, **2015**, pp. 445–476.
- [81] Z. Li, M.-A. Madjet, O. Vendrell, R. Santra, *Faraday Discuss.* **2014**, *171*, 457–470.

## BIBLIOGRAPHY

---

- [82] M.-A. Madjet, O. Vendrell, R. Santra, *Phys. Rev. Lett.* **2011**, *107*, 263002–263006.
- [83] P. Ho, *Future Medicinal Chemistry* **2017**, *9*, 637–640.
- [84] M. Kolář, O. Tabarrini, *JJ. Med. Chem.* **2017**, *60*, 8681–8690.
- [85] A. Brown, P. Beer, *ChemComm* **2016**, *52*, 8645–8658.
- [86] A. Vargas Jentzsch, S. Matile, *J. Am. Chem. Soc.* **2013**, *135*, 5302–5303.
- [87] R. Cabot, C. Hunter, *ChemComm* **2009**, 2005–2007.
- [88] S. Jungbauer, D. Bulfield, F. Kniep, C. Lehmann, E. Herdtweck, S. Huber, *J. Am. Chem. Soc.* **2014**, *136*, 16740–16743.
- [89] F. Zapata, A. Caballero, N. White, T. Claridge, P. Costa, V. Félix, P. Beer, *J. Am. Chem. Soc.* **2012**, *134*, 11533–11541.
- [90] W.-S. Zou, S. Lin, J.-Y. Li, H.-Q. Wei, X.-Q. Zhang, D.-X. Shen, J.-Q. Qiao, H.-Z. Lian, D.-Q. Xie, X. Ge, *New J. Chem.* **2015**, *39*, 262–272.
- [91] A. Jentzsch, S. Matile, *Topics in Current Chemistry* **2014**, *358*, 205–239.
- [92] H. Ungati, V. Govindaraj, G. Mugesh, *Angew. Chem. - International Edition* **2018**, *57*, 8989–8993.
- [93] R. Tepper, U. Schubert, *Angew. Chem. - International Edition* **2018**, *57*, 6004–6016.
- [94] J.-C. Christopherson, F. Topić, C. Barrett, T. Friščić, *Cryst Growth Des.* **2018**, *18*, 1245–1259.
- [95] G. Cavallo, P. Metrangolo, R. Milani, T. Pilati, A. Priimagi, G. Resnati, G. Terraneo, *Chem. Rev.* **2016**, *116*, 2478–2601.
- [96] M. Breugst, D. Von Der Heiden, J. Schmauck, *Synthesis (Germany)* **2017**, *49*, 3224–3236.

- [97] P. Politzer, J. Murray, *ChemPhysChem* **2013**, *14*, 278–294.
- [98] T. Brinck, J. Murray, P. Politzer, *Int. J. Quantum Chem.* **1992**, *44*, 57–64.
- [99] T. Brinck, J. Murray, P. Politzer, *Int. J. Quantum Chem.* **1993**, *48*, 73–88.
- [100] J. Murray, K. Paulsen, P. Politzer, *J. Chem. Sci.* **1994**, *106*, 267–275.
- [101] H. Wörner, C. Arrell, N. Banerji, A. Cannizzo, M. Chergui, A. Das, P. Hamm, U. Keller, P. Kraus, E. Liberatore, P. Lopez-Tarifa, M. Lucchini, M. Meuwly, C. Milne, J.-E. Moser, U. Rothlisberger, G. Smolentsev, J. Teuscher, J. Van Bokhoven, O. Wenger, *Struct Dyn* **2017**, *4*, 061508–61546.
- [102] A. Kuleff, S. Lünemann, L. Cederbaum, *Chemical Physics* **2012**, *399*, 245–251.
- [103] S. Lünemann, A., L. Cederbaum, *J. Chem. Phys.* **2008**, *129*.
- [104] A. Kuleff, S. Lünemann, L. Cederbaum, *J. Phys. Chem. A* **2010**, *114*, 8676–8679.
- [105] L. Cederbaum, J. Zobeley, *Chem. Phys. Lett.* **1999**, *307*, 205–210.
- [106] F. Remacle, R. Levine, *Zeitschrift für Physikalische Chemie* **2007**, *221*, 647–661.
- [107] F. Remacle, R. Levine, *PNAS USA* **2006**, *103*, 6793–6798.
- [108] S. Lünemann, A. Kuleff, L. Cederbaum, *Chemical Physics Letters* **2008**, *450*, 232–235.
- [109] F. Remacle, R. Levine, *J. Chem. Phys.* **2006**, *125*, 133321–133328.
- [110] G. Periyasamy, R. Levine, F. Remacle, *Chemical Physics* **2009**, *366*, 129–138.
- [111] S. Chandra, A. Bhattacharya, *J. Phys. Chem. A* **2016**, *120*, 10057–10071.
- [112] S. Chandra, B. Rana, G. Periyasamy, A. Bhattacharya, *Chemical Physics* **2016**, *472*, 61–71.

## BIBLIOGRAPHY

---

- [113] S. Chandra, M. Iqbal, A. Bhattacharya, *J. Chem. Sci.* **2016**, *128*, 1175–1189.
- [114] O. Bolton, K. Lee, H.-J. Kim, K. Lin, J. Kim, *Nat Chem.* **2011**, *3*, 205–210.
- [115] A. Voth, P. Ho, *Curr. Top. Med. Chem.* **2007**, *7*, 1336–1348.
- [116] M. Scholfield, C. Vander Zanden, M. Carter, P. Ho, *Protein Science* **2013**, *22*, 139–152.
- [117] P. Auffinger, F. Hays, E. Westhof, P. Ho, *PNAS USA* **2004**, *101*, 16789–16794.
- [118] O. Fedorov, K. Huber, A. Eisenreich, P. Filippakopoulos, O. King, A. Bullock, D. Szklarczyk, L. Jensen, D. Fabbro, J. Trappe, U. Rauch, F. Bracher, S. Knapp, *Chem. Biol.* **2011**, *18*, 67–76.
- [119] Y. Lu, Y. Liu, Z. Xu, H. Li, H. Liu, W. Zhu, *Expert Opinion on Drug Discovery* **2012**, *7*, 375–383.
- [120] S. Baumli, J. Endicott, L. Johnson, *Chem. Biol.* **2010**, *17*, 931–936.
- [121] V. Staemmler, A. Palma, *Chem. Phys.* **1985**, *93*, 63–69.
- [122] V. Engel, R. Schinke, V. Staemmler, *J. Chem. Phys.* **1988**, *88*, 129.
- [123] A. J. Dobbyn, P. J. Knowles, *Mol. Phys.* **1997**, *91*, 1107–1124.
- [124] R. van Harrevelt, M. C. van Hemert, *J. Chem. Phys.* **2000**, *112*, 5777.
- [125] R. van Harrevelt, M. C. van Hemert, *J. Chem. Phys.* **2001**, *114*, 9453.
- [126] V. Engel, R. Schinke, *J. Chem. Phys.* **1988**, *88*, 6831.
- [127] N. E. Henriksen, J. Zhang, D. G. Imre, *J. Chem. Phys.* **1988**, *89*, 5607–5613.
- [128] D. G. Imre, J. Zhang, *Chem. Phys.* **1989**, *139*, 89–121.
- [129] F. Xu, L. Wang, C. C. Martens, Y. Zheng, *J. Chem. Phys.* **2013**, *138*, 024103.
- [130] L. Zhou, D. Xie, Z. Sun, H. Guo, *J. Chem. Phys.* **2014**, *140*, 024310.

- [131] R. Mota, R. Parafita, A. Giuliani, M. J. Hubin-Franskin, J. M. C. Lourenço, G. Garcia, S. V. Hoffmann, N. J. Mason, P. a. Ribeiro, M. Raposo, P. Limão-Vieira, *Chem. Phys. Lett.* **2005**, *416*, 152–159.
- [132] X. F. Yang, D. W. Hwang, J. J. Lin, X Ying, *J. Chem. Phys.* **2000**, *113*, 10597–10604.
- [133] I.-C. Lu, F. Wang, K. Yuan, Y. Cheng, X. Yang, *J. Chem. Phys.* **2008**, *128*, 066101.
- [134] J. Z. Zhang, E. H. Abramson, D. G. Imre, *J. Chem. Phys.* **1991**, *95*, 6536.
- [135] N. Shafer, S. Satyapal, R. Bersohn, *J. Chem. Phys.* **1989**, *90*, 6807.
- [136] R. L. Vander Wal, F. F. Crim, *J. Phys. Chem.* **1989**, *93*, 5331–5333.
- [137] R. L. Vander Wal, J. L. Scott, F. F. Crim, K. Weide, R. Schinke, *J. Chem. Phys.* **1991**, *94*, 3548.
- [138] J. Zhang, D. G. Imre, J. H. Frederick, *J. Phys. Chem.* **1989**, *93*, 1840–1851.
- [139] N. Engholm Henriksen, B. Amstrup, *Chem. Phys. Lett.* **1993**, *213*, 65–70.
- [140] P. Farmanara, O. Steinkellner, M. Wick, M. Wittmann, G. Korn, V. Stert, W. Radloff, *J. Chem. Phys.* **1999**, *111*, 6264.
- [141] M. Wittmann, M. Wick, O. Steinkellner, P. Farmanara, V. Stert, W. Radloff, G. Korn, I. Hertel, *Opt. Commun.* **2000**, *173*, 323–331.
- [142] S. A. Trushin, W. E. Schmid, W. Fuß, *Chem. Phys. Lett.* **2009**, *468*, 9–13.
- [143] A. Baumann, S. Bazzi, D. Rompotis, O. Schepp, A. Azima, M. Wieland, D. Popova-Gorelova, O. Vendrell, R. Santra, M. Drescher, *Phys. Rev. A* **2017**, *96*, 013428.
- [144] D. Rompotis, A. Baumann, O. Schepp, T. Maltezopoulos, M. Wieland, M. Drescher, *Optica* **2017**, *4*, 871–878.

## BIBLIOGRAPHY

---

- [145] J. H. Posthumus, *Reports Prog. Phys.* **2004**, *67*, 623–665.
- [146] O. Schepp, A. Baumann, D. Rompotis, T. Gebert, A. Azima, M. Wieland, M. Drescher, *Phys. Rev. A* **2016**, *94*, 033411.
- [147] J. Tully, *J. Chem. Phys.* **1990**, *93*, 1061–1071.
- [148] N. Doltsinis in, NIC, **2006**, pp. 389–409.
- [149] L. Wang, A. Akimov, O. Prezhdo, *J. Phys. Chem. Lett.* **2016**, *7*, 2100–2112.
- [150] J. Tully, *J. Chem. Phys.* **2012**, *137*.
- [151] J. Subotnik, A. Jain, B. Landry, A. Petit, W. Ouyang, N. Bellonzi, *Annu. Rev. Phys. Chem.* **2016**, *67*, 387–417.
- [152] S. Mai, P. Marquetand, L. González, *Wiley Interdisciplinary Reviews: Computational Molecular Science* **2018**, *8*.
- [153] E. Fabiano, T. Keal, W. Thiel, *Chemical Physics* **2008**, *349*, 334–347.
- [154] *Attosecond Molecular Dynamics*, (Eds.: M. J. J. Vrakking, F. Lepine), The Royal Society of Chemistry, **2019**, pp. 1–500.
- [155] K. Khalili, *Lecture notes*, **2015**.
- [156] G. A. Worth, L. S. Cederbaum, *Annu. Rev. Phys. Chem.* **2004**, *55*, PMID: 15117250, 127–158.
- [157] W. L. Hase, D. G. Buckowski, *Chem. Phys. Lett.* **1980**, *74*, 284–287.
- [158] L. Verlet, *Phys. Rev.* **1967**, *159*, 98–103.
- [159] L. VERLET, *Phys. Rev.* **1968**, *165*, 201–214.
- [160] W. C. Swope, H. C. Andersen, P. H. Berens, K. R. Wilson, *J. Chem. Phys.* **1982**, *76*, 637–649.
- [161] M. Richter, P. Marquetand, J. González-Vázquez, I. Sola, L. González, *J. Chem. Theory Comput.* **2011**, *7*, PMID: 26610121, 1253–1258.

- [162] B. O. Roos, P. R. Taylor, P. E. Sigbahn, *Chemical Physics* **1980**, *48*, 157–173.
- [163] T Koopmans, *Physica* **1934**, *1*, 104–113.
- [164] D. Rompotis, T. Gebert, M. Wieland, F. Karimi, M. Drescher, *Opt. Lett.* **2015**, *40*, 1675–1678.
- [165] M. Schultze, B. Bergues, H. Schröder, F. Krausz, K. L. Kompa, *New J. Phys.* **2011**, *13*, 1–9.
- [166] T Gebert, D Rompotis, M Wieland, F Karimi, A Azima, M Drescher, *New J. Phys.* **2014**, *16*, 073047.
- [167] E. Wigner, *Phys. Rev.* **1932**, *40*, 749–759.
- [168] L. Karlsson, L. Mattsson, R. Jadrny, R. G. Albridge, S. Pinchas, T. Bergmark, K. Siegbahn, *J. Chem. Phys.* **1975**, *62*, 4745–4752.
- [169] W. Haynes, *CRC Handbook of Chemistry and Physics*, *91st ed.* Taylor and Francis Group, London, **2010**.
- [170] R. A. kendall, T. H. Dunning Jr., R. J. Harrison, *J. Chem. Phys.* **1992**, *96*, 6796–6806.
- [171] D. E. Woon, T. H. Dunning Jr., *J. Chem. Phys.* **1993**, *98*, 1358–1993.
- [172] F. Aquilante, L. De Vico, N. Ferré, G. Ghigo, P.-a. Malmqvist, P. Neogrády, T. B. Pedersen, M. Pitoňák, M. Reiher, B. O. Roos, L. Serrano-Andrés, M. Urban, V. Veryazov, R. Lindh, *J. Comput. Chem.* **2010**, *31*, 224–247.
- [173] J. W. Rabalais, T. P. Debies, J. L. Berkosky, J.-T. J. Huang, F. O. Ellison, *J. Chem. Phys.* **1974**, *61*, 529–533.
- [174] A. Tielens, *Annu. Rev. Astron. Astrophys.* **2008**, *46*, 289–337.
- [175] R. Lundin, H. Lammer, I. Ribas, *Space Sci. Rev.* **2007**, *129*, 245–278.
- [176] A. Leger, J. L. Puget, *Astron. Astrophys* **1984**, *137*, L5–L8.

## BIBLIOGRAPHY

---

- [177] J. Zhen, S. Castillo, C. Joblin, G. Mulas, H. Sabbah, A. Giuliani, L. Nahon, S. Martin, J.-P. Champeaux, P. Mayer, *Astrophys. J.* **2016**, *822*, 113–120.
- [178] G. Trinquier, A. Simon, M. Rapacioli, F. Gadéa, *Mol. Astrophys.* **2017**, *7*, 37–59.
- [179] L. Allamandola, S. Sandford, B. Wopenka, *Science* **1987**, *237*, 56–59.
- [180] T. Snow, V. Le Page, Y. Keheyan, V. Bierbaum, *Nature* **1998**, *391*, 259–260.
- [181] J. Szczepanski, M. Vala, *Nature* **1993**, *363*, 699–701.
- [182] F. Lovas, R. McMahon, J.-U. Grabow, M. Schnell, J. Mack, L. Scott, R. Kuczkowski, *J. Am. Chem. Soc.* **2005**, *127*, 4345–4349.
- [183] A. Simon, M. Rapacioli, G. Rouaut, G. Trinquier, F. Gadéa, *Phil. Trans. R. Soc. A* **2017**, *375*, 20160195.
- [184] Z. Li, M.-A. Madjet, O. Vendrell, *J. Chem. Phys.* **2013**, *138*, 094313–094311.
- [185] M. Deleuze, A. Trofimov, L. Cederbaum, *J. Chem. Phys.* **2001**, *115*, 5859–5882.
- [186] I. Bâldea, H. Köppel, *J. Chem. Phys.* **2006**, *124*, 064101.
- [187] S. Bazzi, R. Welsch, O. Vendrell, R. Santra, *J. Phys. Chem. A* **2018**, *122*, 1004–1010.
- [188] T. Baer, G. Willett, D. Smith, J. Sanford Phillips, *J. Chem. Phys.* **1979**, *70*, 4076–4085.
- [189] H. Kühlewind, A. Kiermeier, H. Neusser, *J. Chem. Phys.* **1986**, *85*, 4427–4435.
- [190] H. Köppel, *Chem. Phys. Lett.* **1993**, *205*, 361–370.
- [191] D. Holland, D. Shaw, I. Sumner, M. Bowler, R. Mackie, L. Shpinkova, L. Cooper, E. Rennie, J. Parker, C. Johnson, *Int. J. Mass Spectrom.* **2002**, *220*, 31–51.

- [192] H. M. Boechat-Roberty, R. Neves, S. Pilling, A. F. Lago, G. G. B. De Souza, *Mon. Notices Royal Astron. Soc.* **2009**, *394*, 810.
- [193] M. Galbraith, C. Smeenk, G. Reitsma, A. Marciniak, V. Despré, J. Mikosch, N. Zhavoronkov, M. Vrakking, O. Kornilov, F. Lépine, *Phys. Chem. Chem. Phys.* **2017**, *19*, 19822–19828.
- [194] S. Sardar, A. K. Paul, R. Sharma, S. Adhikari, *Int. J. Quantum Chem.* **2011**, *111*, 2741–2759.
- [195] H. Köppel, M. Döscher, I. Bâldea, H.-D. Meyer, P. G. Szalay, *J. Chem. Phys.* **2002**, *117*, 2657–2671.
- [196] O. Braitbart, E. Castellucci, G. Dujardin, S. Leach, *J. Phys. Chem.* **1983**, *87*, 4799–4804.
- [197] M. Kim, C. Kwon, J. Choe, *J. Chem. Phys.* **2000**, *113*, 9532–9539.
- [198] L. Gilday, S. Robinson, T. Barendt, M. Langton, B. Mullaney, P. Beer, *Chem. Rev.* **2015**, *115*, 7118–7195.
- [199] K.-L. Han, G.-J. Zhao, *Hydrogen Bonding and Transfer in the Excited State*, Vol. 1-2, John Wiley & Sons, **2011**.
- [200] A. Sobolewski, W. Domcke, *J. Phys. Chem. A* **2007**, *111*, 11725–11735.
- [201] F. Aquilante, J. Autschbach, R. K. Carlson, L. F. Chibotaru, M. G. Delcey, L. D. Vico, I. F. Galván, N. Ferré, L. M. Frutos, L. Gagliardi, M. Garavelli, A. Giusani, C. E. Hoyer, G. L. Manni, H. Lischka, D. Ma, P. Å. Malmqvist, T. Müller, A. Nenov, M. Olivucci, T. B. Pedersen, D. Peng, F. Plasser, B. Pritchard, M. Reiher, I. Rivalta, I. Schapiro, J. Segarra-Martí, M. Stenrup, D. G. Truhlar, L. Ungur, A. Valentini, S. Vancoillie, V. Veryazov, V. P. Vysotskiy, O. Weingart, F. Zapata, R. Lindh, *J. Comput. Chem.* **2016**, *37*, 506.

## BIBLIOGRAPHY

---

- [202] S. A. Cooke, G. K. Corlett, C. M. Evans, A. C. Legon, J. H. Holloway, *J. Chem. Phys.* **1998**, *108*, 39–45.
- [203] L. Sun, W. L. Hase, *J. Chem. Phys.* **2010**, *133*, 044313.
- [204] G. Granucci, M. Persico, A. Zocante, *J. Chem. Phys.* **2010**, *133*, 134111.
- [205] O. Kühn, L. Wöste, *Analysis and control of ultrafast photoinduced reactions*, Vol. 87, Springer Science & Business Media, **2007**.
- [206] M. Lara-Astiaso, M. Galli, A. Trabattoni, A. Palacios, D. Ayuso, F. Frassetto, L. Poletto, S. De Camillis, J. Greenwood, P. Decleva, I. Tavernelli, F. Calegari, M. Nisoli, F. Martín, *J. Phys. Chem. Lett.* **2018**, *9*, 4570–4577.

# Eidesstattliche Erklärung

Hiermit erkläre ich an Eides statt, dass ich die vorliegende Dissertationsschrift selbst verfasst und keine anderen als die angegebenen Quellen und Hilfsmittel benutzt habe.

Hamburg, den

Unterschrift

## *H and P substances*

I herewith declare that I have not used any H and P substances during my Ph.D. work.